ALUMINUM OXIDE TEMPLATE AND TITANIUM OXIDE NANOTUBES AND THEIR APPLICATIONS

LIM SIEW LENG
(B. Sc (Hons), NUS)

A THESIS SUBMITTED FOR THE DEGREE OF
DOCTORAL OF PHILOSOPHY
DEPARTMENT OF PHYSICS
NATIONAL UNIVERSITY OF SINGAPORE
2011

Acknowledgements

I would like to express my deepest gratitude to my supervisors, Prof. Ong Chong Kim and Assistant Prof. Lim Hock Siah. I would like to thank Prof. Ong for giving me the opportunity to perform research work in the Center of Superconducting and Magnetic Materials (CSMM). Due to his constant advice and supervision, I am able to progress in designing experiments and interpreting the result. Without his patience and guidance during my postgraduate study in National University of Singapore, I would not have reached this far.

I would also like to express my appreciations to Dr Ma Yungui, Dr Nguyen Nguyen Phuoc, Dr Zhang Xiaoyu and Dr Xu Feng in CSMM for giving me useful advices and rendering help whenever I have difficulty in performing the experiments and analysing the results. I am also grateful to my fellow colleagues in CSMM, Chen Xin, Phua Li Xian, Song Qing, Zhu Gui, Li Jing, and Sheng Su in CSMM and Mr Tan Choon Wan from the physics workshop.

I would also like to thank Prof Kang En-Tang, Dr Liu Yiliang and Dr Liu Gang from Department of Chemical and Biomolecular Engineering of NUS for their assistance and advice in performing experiments.

I would also like to acknowledge the financial support from the National University of Singapore for providing scholarship during this course of study.

Last but not the least, I would like to thank my family for giving me the support and encourage throughout mine postgraduate study in NUS. None of this would be possible without their love and concerns.

Table of Content

2. Fabrication and characterization

3. Magnetic anisotropy

Summary

In this thesis, aluminum oxide template and titanium oxide nanotube were fabricated by anodization method. With the aid of anodized aluminum oxide (AAO) template, three different magnetic nanostructures have been fabricated: (1) ferromagnetic $CoFe_2$ nanowires electrodeposited into the pores of AAO template using AC voltage, (2) ferromagnetic CoAlO antidot arrays deposited on top of AAO template by co-sputtering AlO and Co targets and (3) exchange bias coupled multilayered FeNi/FeMn antidot arrays deposited on top of AAO template by sputtering FeNi and FeMn targets in an alternating manner. Geometrical factors of these magnetic nanostructures on their magnetic properties were investigated.

We first fabricated a series of $CoFe_2$ nanowire samples of different lengths with diameter of 32 nm and interpore distance of 65 nm. Studies of magnetic properties of the $CoFe_2$ nanowires electrodeposited into pores of the template using AC voltage were presented in this work. We investigated the effect of length of the nanowires at extreme high aspect ratio on their coercivity and remanence. The coercivity and remanence measured along the longitudinal axis of the nanowires increased with increasing length. This observation can be explained by taking into account the dipolar interaction between the nanowires.

We next used sputtering to deposit CoAlO antidot array on top of AAO template. The effect of pore size and thickness of the CoAlO antidot array on its magnetic and transport properties was investigated. During the film deposition, external magnetic field was applied in situ on the film plane to induce an effective uniaxial anisotropy. When the pore size of the CoAlO antidot array was increased from 0 nm to 80 nm while the thickness

was kept at 40 nm, coercivities increased and magnetic anisotropy changed from anisotropic to nearly isotropic. This phenomenon was attributed to the shape anisotropy induced from the pore modulated network topology. Similarly, magnetoresistance behaviors also varied from anisotropic to isotropic as the pore size was increased. This behaviour can be explained by the isotropic magnetic properties and current trajectories being confined along the network in larger pore diameter antidot array. However, when the thickness of the antidot array with pore diameter of 80 nm was increased from 10 nm to 180 nm, coercivity decreased. This is probably due to the fact that there had been a transition in the domain reversal process from domain rotation in the thin antidot array to domain wall motion in the samples of higher structural continuity. Negligible magnetoresistive loops were observed in the thick films. This could be explained by spin independent electron scattering.

We then proceeded to study exchange bias effect in multilayered ferromagnetic FeNi / antiferromagnetic FeMn antidot array deposited on top of AAO template. We have studied the effect of pore size of the AAO template and thickness of the FeNi layer on the strength of exchange bias and ferromagnetic resonance (FMR) frequency of this system. The exchange bias field (H_E) determined from the magnetic hysteresis loop was enhanced significantly as the pore diameter was increased in a thin FeNi layer sample, but it did not change much in thicker FeNi layer sample. This behaviour can be qualitatively explained by employing the random field model proposed by Li and Zhang [Z. Li and S. F. Zhang, *Phys. Rev. B* **61**, R14897 (2000)]. The uniaxial anisotropy field (H_k) showed similar variation with the pore diameter as the exchange bias field since the exchange coupling between the FM and AFM can also induce uniaxial anisotropy besides unidirectional

anisotropy. Microwave measurement also indicated that FMR frequency is significantly enhanced by the pore size in a similar way to the exchange bias field and the uniaxial anisotropy field.

We also fabricated two different TiO_2 nanotube structures and attempted to study the feasibility of using the TiO_2 nanotube array as hybrid photovoltaic when combined with P3HT polymer. The first type of TiO_2 nanotube structure was formed via direct anodization of titanium foil and P3HT polymer was infiltrated into pores of such TiO_2 nanotubes by dip coating method. Extent of the polymer infiltration into the TiO_2 nanotubes was investigated. The infiltration of the P3HT polymer has been confirmed by UV–Vis absorption spectrometer measurement which showed peak absorption at 500 nm due to the embedded polymer within the nanotube arrays. Time of flight–secondary ion mass spectrometer depth profiling up to 500 nm showed that P3HT polymer was infiltrated into the TiO_2 nanotube arrays. Furthermore, energy-dispersive X-ray spectroscopy of transmission electron microscopy (TEM) indicated the presence of sulfur and carbon atoms due to the P3HT polymer. TEM observations also showed that the pore was filled with the polymer. Polymer nanotubes can be obtained after the TiO_2 nanotubes were etched by dilute HF solution.

However, the TiO_2 nanotubes formed via anodization of titanium foil were not transparent and hence they are not a suitable electrode to be used in photovoltaic device. We then anodized Ti film sputtered directly on indium tin oxide (ITO) coated glass to form transparent TiO_2 nanotubes. We were able to eliminate residue titanium on the ITO glass completely during the anodization so that the oxide electrode formed was transparent. Two types of electrolytes were used in this work: an aqueous mixture of

acetic acid and HF solution and a mixture of NH_4F and water in ethylene glycol. The concentration of NH_4F, the applied voltage and the thickness of the sputtered titanium film were varied to study their effects on formation of the TiO_2 nanotube arrays. It was found that the electrolyte consisting of 0.75% (wt.) NH_4F and 2% (vol.) H_2O and an anodization voltage of 40 V were optimal for the formation of TiO_2 nanotube arrays. It was also demonstrated in this work that a nanoporous layer was formed on top of the TiO_2 nanotube arrays. Furthermore, UV-Vis spectrometer measurement indicated that the TiO_2 nanotubes annealed at 450^oC in air had much lower transmittance than the non-annealed TiO_2 nanotubes in visible region.

List of Tables

List of Figures

Chapter 1 Introduction

1.1 Introduction

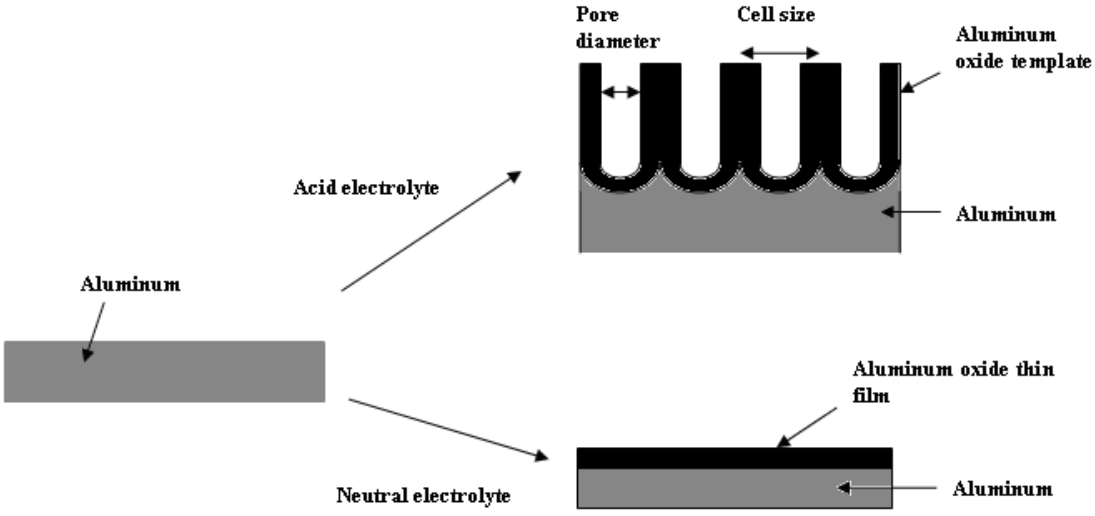

Fig. 1.1 Formation of aluminum oxide template and aluminum oxide thin film via anodization of aluminum.

Anodization has been used commercially since at least 1923 to protect or decorate aluminum surfaces. Anodic aluminum oxide template with porous structure can only be formed by using acidic electrolyte (usually phosphoric, oxalic and sulfuric acid solutions). Using electrolyte with pH >5 in the anodization leads to formation of a compact aluminum oxide thin film. In the early days of porous alumina research (1953), Keller et al reported on cell structure (shown in Fig. 1.1) and anodic voltage dependence of the cell size [1]. They defined a cell as the unit area containing a single pore surrounded by its wall. Anodic aluminum oxide template consists of pores growing in the direction normal to the surface as shown in Fig. 1.1. In 1970s, several authors such as O'Sullivan & Wood [2] and Thompson et al [3] proposed a model to describe pore formation based on electrical field assisted dissolution. The two main processes that took place in the pore

formation are (i) growth of the aluminum oxide at the interface between aluminum and aluminum oxide due to the transport of Al^{3+}, OH^- and O^{2-} ions within the aluminum oxide film and (ii) the dissolution of the aluminum oxide at the interface between the aluminum oxide film and electrolyte. In 1992, Parkhutik and Shershulsky presented a mathematical theory for single pore growth [4]. Both models can give microscopic explanations for the dependence of pore diameters and pore distances on applied voltage or electrolyte composition.

It was until late 1990s that high degree of ordering can be attained in the aluminum oxide template. Masuda and co-workers grew an aluminum oxide template with a perfect hexagonal pore arrangement over a large area at micron scale by first anodizing aluminum foil for more than 10 h, dissolving aluminum oxide template, and finally reanodizing for a few minutes [5]. They also used electron beam lithography to form a patterned SiC surface with periodic convex surfaces and "nanoindent" the Al surface with this pattern to give the "correct spacings" prior to anodization in acid [6]. A perfect hexagonal pore arrangement with dimension of 2 mm x 2 mm can be achieved in this way. During high current density electropolishing of aluminum, hexagonal ordering patterns of pits can be formed [7]. Subsequent anodization of this electropolished aluminum will yield also perfect hexagonal pore arrangement. Systematic variation of electropolishing time and voltage has been carried out to establish the regions of stability of hexagonal patterns, random patterns, and striped patterns. It has been discovered that only certain anodization conditions can lead to self-organization of the pores. Jessensky et al reported that ordered hexagonal array can be obtained using oxalic and sulfuric acid electrolyte [8,9]. For each type of electrolyte used, a hexagonal pore array can only be

formed at a particular voltage [8,9]. Nielsh et al proposed that as long as anodic aluminum oxide film formed has 10% porosity, self-ordering of the pores into hexagonal array is possible [10]. Both Jessensky and Nielsh attributed these observations to the resulting mechanical stress from the oxide volume expansion at the oxide and metal interface during anodization. The empirical model proposed by Nielsh seems to be in contradiction to the recent result obtained by Lee et al [11] who successfully fabricated well-ordered hexagonal pore arrays in an aluminum oxide template with 3.3 % porosity. Up to now, the driving force for the self-organization of the pores still remains unclear.

More recently, it has been discovered that anodization of other valve metals such as titanium in electrolyte containing F^- ions can also lead to the formation of porous systems. In 1991, Zwilling and co-workers [12,13] reported a disordered porous array of titanium oxide film formed in aqueous solution containing F^- ions. Further studies were focused on achieving uniform and ordered nanotube arrays and precise control over morphology, pore size, wall thickness and length of the nanotube arrays. Electrolyte composition and pH value have great influences over the resultant structure of the nanotube arrays since they determine both the rate of titanium oxide dissolution and the rate of nanotube array formation. More than a decade later in 2001, Gong and co-workers were the first to report on successful formation of ordered array of nanotubes up to 0.5 μm length by electrochemical anodization of Ti foil in HF aqueous electrolyte [14]. In the second generation of nanotube array synthesis, Cai and co-workers [15] fabricated nanotube arrays with length of up to approximately 7 μm by using an aqueous buffered electrolyte which consisted of NaF or NH_4F instead of HF [15,16]. By controlling anodization electrolyte pH values, the chemical dissolution of TiO_2 during anodization can be

reduced and longer tubes can be attained in this way. When a non-aqueous, polar organic electrolyte such as formamide, dimethyl sulfoxide, ethylene glycol, or diethylene glycol was used, nanotube with lengths of up to approximately 1000 μm can be formed. This is the third generation of TiO_2 nanotube arrays [17-21]. The fourth generation of TiO_2 nanotube array synthesis is represented by anodizing titanium in perchlorate and chloride containing electrolyte in instead of F^- ions dissolved in electrolyte [22,23]. However, disordered tube bundles are obtained and their formation is due to a continuous series of dielectric breakdown, which is drastically different from the mechanistic process of self-assembly in the anodization.

Anodization of aluminum and titanium foil result in formation of aluminum oxide template and titanium oxide nanotubes whose pore diameter, length and interpore distance can be controlled readily. This gives us an opportunity to fabricate different magnetic nanostructrures. In this work, three magnetic nanostructures, including $CoFe_2$ nanowire, CoAlO antidot array and FeNi / FeMn antidot array, with desired dimensions were fabricated using aluminum oxide template. The effects of geometrical factors of these magnetic nanostructures on their magnetic properties were studied. Furthermore, we also fabricated two types of TiO_2 nanotube which included P3HT/TiO_2 nanotubes on titanium foil and TiO_2 nanotubes on transparent conductive indium tin oxide substrate. This allowed us to study the feasibility of using TiO_2 nanotubes for P3HT-TiO_2 hybrid photovoltaic.

With the technological development of aluminum oxide template and titanium oxide nanotube and their applications which are studied in my thesis being briefly outlined in this section, we will include a brief review of the three magnetic nanostructures and the

two TiO_2 nanotube structures fabricated in section 1.2 and 1.3, respectively. This chapter will conclude with the objectives for undertaking the present work and outline of my thesis.

1.2 Applications of aluminum oxide template: Magnetic nanostructures

The three different magnetic nanostructures which were studied in this work include soft ferromagnetic CoAlO antidot array, exchanged bias coupled FeNi/FeMn antidot array and ferromagnetic $CoFe_2$ nanowire array. Magnetic antidot array and magnetic nanowire array have attracted much interest from the researchers, due to their potential applications in magnetic recording technology. These magnetic nanostructures were fabricated with the aid of aluminum oxide templates. By sputtering magnetic layers onto surface of the aluminum oxide templates, magnetic thin films with periodic array of holes were formed, which are known as antidot arrays. Magnetic nanowires can be electrodeposited into the pores of the aluminum oxide templates using AC voltage.

1.2.1 Ferromagnetic $CoFe_2$ nanowire arrays

Co_xFe_{100-x} alloys are of current interest due to their potential application as perpendicular recording heads. They possess a high saturation magnetization, $\mu_0 Ms$ = 2.4 T, in the range of $30 < x < 50$ [24]. Due to their negligible magnetocrystalline anisotropy, bulk or thin film Fe-Co alloys have extremely low coercivity, which makes them unsuitable to be used as magnetic recording materials [24].In contrast to their bulk or thin film counterparts, Fe-Co nanowires exhibit a relatively square hysteresis loop with enhanced coercivity H_c and higher remanence M_r when the field is applied perpendicular to the substrate (parallel to longitudinal axis of the nanowire) [25]. When the magnetic

field is applied parallel to the substrate (perpendicular to longitudinal axis of the nanowires), the hysteresis loop becomes sheared with low coercivity. This indicates that the longitudinal axis of the nanowire is the direction of easy magnetization. These distinct magnetic properties of Fe-Co nanowires are entirely attributed to the shape anisotropy of nanowires which have high aspect ratio (ratio of length to the diameter). When the field is applied parallel to the longitudinal axis of each nanowire, there are only two stable remanent magnetization states (either upward or downward magnetization along the longitudinal axis of the nanowire). This allows each magnetic nanowire to store "0" which corresponds to downward magnetization state or "1" which corresponds to upward magnetization state. Thus, Fe-Co nanowires have been proposed to be used as high density perpendicular magnetic recording material.

The magnetic properties of Fe-Co nanowires are not only governed by their shape anisotropy but also by the dipolar stray field generated from each nanowire. Dipolar stray field is generated due to the magnetic charges at surface of the nanowire wires (defined as **M**.**n,** where **n** is normal direction of surface of the nanowire and **M** is magnetization direction within the nanowire) and is in the opposite direction to magnetization of the wire. As a consequence, this will reduce the applied field to reverse their magnetizations. With magnetostatic interactions considered, previous works have well interpreted the decreases in coercivity and remanence of nickel nanowire arrays with increasing diameter of the nanowires while their interpore distance is kept constant [26,27]. Few experimental works have also been carried to investigate on the effect of length on magnetostatic interaction of magnetic nanowires with extremely high aspect ratios [28,29].
Thus, the effect of length of Fe-Co nanowires on their coercivity and remanence at

extremely high aspect ratios was carried in this work.

1.2.2 Ferromagnetic CoAlO antidot arrays

CoAlO granular films can be fabricated by sputtering Co and Al at the same time in the presence of argon mixed with oxygen. These granular films consist of Co\CoAl particles and amorphous AlO matrix. Depending on their compositions, CoAlO granular films can be either soft ferromagnetic or superparamagnetic [30]. CoAlO granular films are superparamagnetic when the films consist of isolated Co embedded in AlO matrix. They are soft ferromagnetic when the films consist of either isolated AlO spheroids in Co\CoAl interconnected particles or interconnected long cylindrical Co particles in AlO matrix. For the former, the concentration of AlO is higher and the number of Co crystals is small within the exchange length. Thus the magnetocrystalline anisotropy of Co is not effectively averaged out and high coercivity of 50 Oe is obtained [31-33]. For the latter, the concentration of AlO is low and each long cylindrical particle consists of randomly oriented Co crystals. Thus the magnetocrystalline anisotropy of Co is effectively averaged out and low coercivity of less than 10 Oe is obtained [31-33].

Although the magnetic and transport properties of these three types of continuous CoAlO thin films have been investigated, there is no detailed report on the effect of holes formed in the soft ferromagnetic CoAlO thin films. Many studies carried out on the permalloy ferromagnetic antidot structures showed that their coercivity was significantly higher [34-36] as compared to that of their parent continuous films due to the domain walls being pinned by the holes. The coercivity can be controlled by size and volume density of the holes presented in the film. The intrinsic magnetic anisotropy will be also modified by the presence of the holes. Experiments have verified that well defined

periodic domain structures in the vicinity of the holes are formed in the demagnetized state to reduce the net magnetic surface charges [37,38]. Cowburn et al [39] proposed that antidot structure made of periodic square holes can be used for longitudinal recording purpose since recording bits can be trapped between the consecutive square holes along the intrinsic hard axis of the magnetic material (green areas of Fig. 1.2) when magnetic field is applied along the intrinsic hard axis. Shape anisotropy of the antidot array will prefer easy direction of magnetization along the direction of the length of square hole since this will reduce the net magnetic surface charges. Thus, in the green areas, the direction of easy axis no longer lies along the intrinsic easy axis but will be along the length of square. In the pink areas, the direction is still along the intrinsic easy axis. In yellow areas, the easy axis is still along the length of the square hole which is due to the shape anisotropy and reinforced by its intrinsic easy axis.

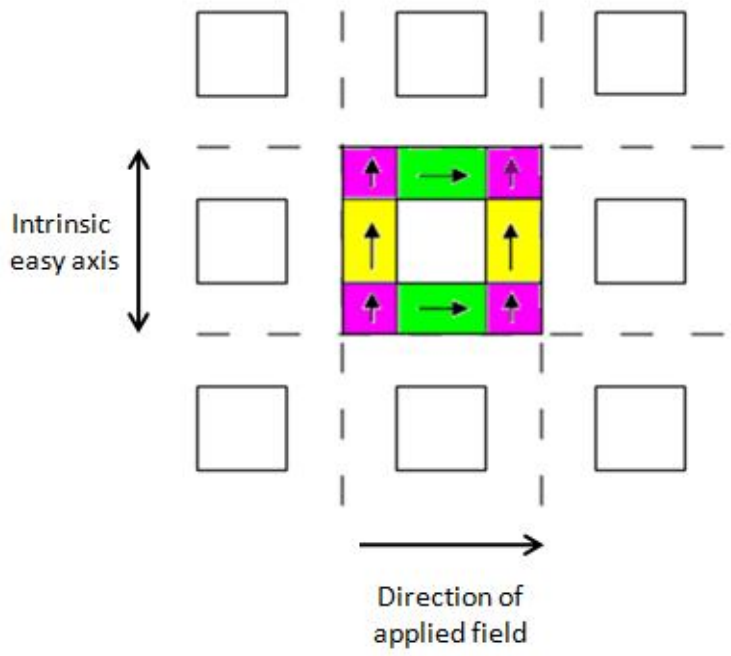

Fig. 1.2 Ideal remanent state of antidot array with periodic square holes. The area in green can be used to store a bit.

Fundamentally, the switching mechanism during the magnetization reversal process is an important issue which is not well understood in the nanoscale regime. In this thesis, the effect of pore diameter and thickness of soft ferromagnetic CoAlO antidot arrays formed on AAO templates on their magnetic anisotropy and magnetoresistance behavior in the nanoscale range have been investigated.

1.2.3 Exchanged bias coupled ferromagnetic FeNi /antiferromagnetic FeMn antidot arrays

In 1956, Meikejohn and Bean discovered that partially oxidized Co nanoparticles exhibited hysteresis loop shift after the samples were field cooled through the Neel temperature (T_N) of CoO which is lower than the Curie temperature (T_C) of Co [40,41]. This observation is also known as exchange bias and the effect has important applications which include permanent magnets, magnetic recording media or domain stabilizers in recording heads based on anisotropic magnetoresistance [42]. This exchange bias arises from the ferromagnetic coupling of both the ferromagnetic spins from Co particles and the antiferromagnetic spins from CoO layer at the interface of Co/CoO.

There have been numerous studies carried on continuous bilayer thin films of ferromagnetic and antiferromagnetic [43-45] but there are relatively fewer works to study the exchange bias in nanostructured materials [46-48]. While some researchers have reported a reduction in exchange bias field as compared to thin films [46], others have observed an opposite trend [47]. Alternating layers of antiferromagnetic and ferromagnetic antidot arrays formed on aluminum oxide template allowed us to study exchange bias at reduced lateral dimensions over a macroscopic area in a nanostructured system which has uniform and controlled geometry. In this thesis, the effect of pore size

and thickness of the ferromagnetic layer on exchange bias and the ferromagnetic resonance frequency were investigated in the alternating multilayer of ferromagnetic (FM) FeNi and antiferromagnetic (AFM) FeMn antidot arrays formed on aluminum oxide templates.

1.3 TiO_2 nanotube arrays and their application in photovoltaic devices

Titanium oxide nanotube structures were fabricated in this thesis for potential applications in photovoltaic devices. The first one was formed by anodizing Ti foil. Poly(3-hexyl thiophene) (P3HT) polymer was infiltrated into the tubes by dip coating method. The second one was fabricated directly on indium tin oxide/glass substrates. The latter is highly desirable as compared to the former for fabrication of P3HT-TiO_2 hybrid photovoltaic since it is transparent.

1.3.1 P3HT/TiO_2 nanotube arrays on Ti foil

Bulk heterojunction can be made by filling inorganic nanostructures with conducting conjugated polymer. Inorganic nanostructures consist of metal oxide template such as TiO_2 nanoparticle film, TiO_2 nanotubes, and ZnO nanorods. In P3HT polymer-TiO_2 bulk heterojunctions, P3HT polymer absorbs light and exciton pairs are created. These excitons travel to the polymer-TiO_2 interface where the exciton pairs will be separated into electrons and holes. The electron will travel to TiO_2 and the holes will travel in the polymer. Thus, photocurrent is generated.

The infiltration of polymer into nanostructured metal oxide is of particular importance for optimizing the performance of these hybrid devices. Wet processing deposition techniques, such as spin-coating, dip-coating, drop-casting, doctor-blading,

inkjet-printing, and screen-printing, are popular approaches to cast the polymer film into nanostructured metal oxide from solution [49-54]. However, infiltration of P3HT polymer into TiO_2 mesoporous films or nanotube arrays can be a challenge if a polymer with large molecular weight is used. Due to the large radius of gyration of higher molecular weight P3HT polymer, the polymer suffers a loss of conformational entropy when it is confined in a channel whose radius is less than that of the polymer gyration radius and thus clogs the pores [55]. Another potential barrier to infiltration of P3HT polymer into TiO_2 mesoporous films or nanotube arrays is hydrophobic/hydrophilic interaction. With its large alkyl groups and uncharged backbone, P3HT polymer is hydrophobic, whereas the highly polar TiO_2 surface is hydrophilic [56]. As a result, there is a problem of incompatibility. One of the strategies used to improve the efficiency of polymer infiltration is to heat the polymer overlying the TiO_2 film above its melting point [56]. To improve the compatibility of TiO_2 surface with the nonpolar P3HT polymer, TiO_2 surface can be coated with an amphiphilic molecular monolayer such that the outward facing part of the attached molecule is nonpolar [56]. Recently, polymer was incoporated into the TiO_2 porous film by chemical in situ polymerization of a soluble low molecular weight monomer instead of inserting from solution of a high molecular weight polymer into the pores [57,58]. There are detailed reports on the extent of infiltration of P3HT conjugated polymer into TiO_2 mesoporous films with different morphologies. Bartholomew and Heeger [56] infiltrated P3HT polymer into 2.2 μm thick random nanocrystalline TiO_2 networks (RNTNs). Even with an overnight heat treatment at 200 ^{o}C, the incorporation of polymer was still slightly below 3%. Coakley et al. [55] infiltrated P3HT polymer into thin mesoporous (50–300 nm) TiO_2 film with uniform pore

sizes (10 nm) by spin coating. In his case, with heating of the polymer to 200 ^{o}C, they were able to achieve incorporation of polymer up to 33%. From these studies, it is clear that morphology of the TiO_2 film can affect the infiltration efficiency of polymer to a large extent.

In this work, we examined the infiltration of P3HT polymer into the ordered array of TiO_2 nanotubes by dip coating. The morphology of the TiO_2 nanotubes is radically different from that of mesoporous TiO_2 film because TiO_2 nanotube arrays offer straight nanopores while the mesoporous TiO_2 film which is made of an interconnected network has inaccessible internal voids that might hinder infiltration of polymer. Furthermore, the average pore radius of the TiO_2 nanotubes is 30 nm, which is much larger than the gyration radius of the polymer chains, in the range of 8.5– 10.6 nm.

1.3.2 Transparent TiO_2 nanotube arrays

The titanium foil which underlies the nanotube arrays can limit the application of P3HT/TiO_2 nanotube arrays in photovoltaic devices. Thus it is of high technological interest to form TiO_2 nanotubes directly on transparent conductive oxide films coated on glass substrates like indium tin oxide (ITO) and fluorine-doped tin oxide (FTO) and this transparent oxide, which serve as electrode through which light can be illuminated onto the P3HT/TiO_2 layers. There are several approaches to fabricate TiO_2 nanotubes directly on desired substrates. One of the most investigated methods is to deposit titanium metal film directly on desired substrate, from which TiO_2 nanotubes can be formed via anodization. Mor et al achieved TiO_2 nanotube arrays from anodization of RF sputter films deposited on glass at 500^{o}C using an electrolyte containing acetic acid and hydrofluoric acid [59]. Macak et al. reported anodization of titanium film which was ion

beam sputtered on silicon substrates in a HF/H_2SO_4 electrolyte [60]. Yang et al formed TiO_2 nanotubes by anodization of DC sputtered Ti films on silicon substrate at 500^oC in NaF aqueous electrolyte [61]. However, few research works have been carried out to investigate the anodization of titanium on ITO glass [62,63] even though there are many reports on anodization of titanium on FTO glass [64-67].

In this work, transparent TiO_2 nanotubes of micrometer length were prepared by anodization of titanium thin film which was RF sputtered onto ITO glass substrates. Using this technique, we are able to fabricate TiO_2 nanotube arrays with residue metal underneath the nanotubes completely being eliminated.

1.4 Objectives and outline of the thesis

In this thesis, aluminum oxide template and titanium oxide nanotubes were formed by anodization method. With the aid of aluminum oxide template, three magnetic nanostructures, including ferromagnetic $CoFe_2$ nanowires, ferromagnetic CoAlO antidot arrays and exchange bias coupled FeNi / FeMn antidot arrays with the desired dimensions, were fabricated. This allowed us to study magnetic properties at reduced lateral dimensions over a macroscopic area in a nanostructured system which has uniform and controlled geometry. These magnetic nanostructures displayed exotic properties that differed drastically from those of their continuous thin film counterparts which have been routinely studied. The objective of this thesis was to study the effects of geometrical factors of these magnetic nanostructures on their magnetic properties so that we can better understand the underlying physics of magnetism in the nanoscale regime. In order to achieve this objective, we first electrodeposited $CoFe_2$ nanowires into the pores and studied the effect of length of the $CoFe_2$ nanowires on coercivity and remanence of the

nanowires with extremely high aspect ratios. Secondly, we deposited CoAlO directly on top of aluminum oxide templates by sputtering and investigated the effect of pore size and thickness of CoAlO antidot arrays on their magnetic and magnetotransport properties. Thirdly, we deposited multilayered FeNi /FeMn antidot arrays on top of aluminum oxide templates by sputtering and systemically studied the effect of thickness and pore size on exchange bias field and resonance frequency.

Besides these, we also synthesized two types of TiO_2 nanotube structures for potential applications in photovoltaic devices: (1) anodizing Ti foil to form TiO_2 nanotubes into which P3HT polymer was infiltrated into by dip coating method and (2) anodization of sputtered Ti film on ITO coated glass to form transparent TiO_2 nanotube arrays. This allowed us to study the feasibility of the TiO_2 nanotube array for TiO_2-P3HT hybrid photovoltaic devices. In order to achieve this objective, we first investigated the efficiency of polymer infiltration into the nanotubes of the first type of nanotube array. Secondly, we proceeded to investigate the conditions necessary for formation of transparent TiO_2 nanotubes on top of ITO/glass substrates.

The layout of the thesis is as follows:

In the Chapter 2, details of various experimental procedures used in this work are presented.

In Chapter 3, various types of magnetic anisotropy that govern the direction of magnetization in a magnetic material are presented.

In Chapter 4, studies of magnetic properties of $CoFe_2$ nanowires electrodeposited into the pores of AAO templates using AC voltage are presented. We investigated the effect of length of the nanowires at extreme high aspect ratios on coercivity and remanence

of the nanowires. The coercivity and remanence measured along longitudinal axis of the nanowires increased with the length. This observation can be explained by taking into account the dipolar interaction between the nanowires.

In Chapter 5, our work on CoAlO antidot arrays deposited on top of AAO templates by co-sputtering of AlO and Co targets is presented. The effect of pore size and thickness of the CoAlO antidot arrays on their magnetic and transport properties were investigated. During the film deposition, external magnetic field was applied in situ on the film plane to induce an effective uniaxial anisotropy. When pore size of CoAlO antidot arrays was increased from 0 nm to 80 nm while the thickness was kept at 40 nm, the coercivities increased and magnetic anisotropy changed from anisotropic to nearly isotropic. This phenomenon was determined by the shape anisotropy induced due to the pore modulated network topology. Similarly, magnetoresistance behaviors also varied from anisotropic to isotropic as the pore size was increased. This behaviour can be explained by the isotropic magnetic properties and current trajectories being confined along the network in antidot arrays with larger pore diameters. However as the thickness of the antidot arrays whose pore diameter of 80 nm was increased from 10 nm to 180 nm, coercivity decreased. This is probably due to the change in domain reversal process from domain rotation in the thin antidots to domain wall motion in the samples of higher structural continuity. Negligible magnetoresistive loops were obtained in thick films. This could be possibly due to the spin independent electron scattering.

In Chapter 6, we studied the dependence of exchange bias and resonance frequency of the multilayer FeNi and FeMn antidot arrays on pore size and thickness of the FeNi layers. The exchange bias field (H_E) determined from magnetic hysteresis loop was

enhanced significantly as the pore diameter was increased in a thin FeNi layer sample but it did not change much in thicker FeNi layer samples. This behaviour can be qualitatively explained by employing the random field model proposed by Li and Zhang [68]. The uniaxial anisotropy field (H_k) showed similar variation with pore diameter to the exchange bias field since the exchange coupling between the FM and AFM can also induce uniaxial anisotropy besides unidirectional anisotropy. Microwave measurement also indicated that resonance frequency was significantly increased with increasing pore size in a similar way to the exchange bias field and the uniaxial anisotropy field.

In Chapter 7, the level of incorporation of P3HT polymer into TiO_2 nanotube arrays formed via direct anodization of titanium foil will be discussed. The polymer was infiltrated into the nanotubes by using dip coating method. UV–Vis absorption spectrometer measurement of the P3HT/TiO_2 nanotubes showed a peak absorption at 500 nm due to the embedded polymer within the nanotube arrays. Time of flight –secondary ion mass spectrometer depth profiling up to 500 nm showed that the P3HT polymer was infiltrated into the TiO_2 nanotube arrays. Furthermore, energy-dispersive X-ray spectroscopy indicated the presence of sulfur and carbon, confirming the presence of the P3HT polymer. Polymer nanotubes can also be observed with scanning electron microscopy (SEM) after the TiO_2 nanotubes were etched by using dilute HF solution.

In Chapter 8, transparent TiO_2 nanotube arrays of micrometer lengths were prepared via anodization of titanium thin film RF sputtered on ITO/glass substrates. Two types of electrolytes were used in this work: an aqueous mixture of acetic acid and HF solution and a mixture of NH_4F and water dissolved in ethylene glycol. The concentration of NH_4F, voltage and the thickness of the sputtered titanium film were varied to study their

effects on the formation of the TiO_2 nanotube arrays. It was found that electrolyte consisting of 0.75% (wt.) NH_4F and 2% (vol.) and anodization voltage of 40 V were optimal for the formation of TiO_2 nanotube arrays. It was also demonstrated that a nanoporous layer was formed on top of the ordered array of TiO_2 nanotubes. Furthermore, UV-Vis spectrometer measurement indicated that the TiO_2 nanotubes annealed at 450^oC in air had much lower transmittance than the non- annealed TiO_2 nanotubes in the visible region.

In Chapter 9, main conclusions and future work of this study and will be presented.

1.5 References

[1] F. Keller, M. S. Hunter and D. L. Robinson, *J. Electrochem. Soc.* **100**, 411 (1953).

[2] J. P. O'Sullivan and G. C. Wood, *Proc. R. Soc.* **A317**, 511 (1970).

[3] G. E. Thompson, R. C. Furneaux, G. C. Wood, J.A. Richardson and J. S. Goode, *Nature* **272**, 433 (1978).

[4] V. P. Parkhutik and V. I. Shershulsky, *J. Phys. D: Appl. Phys.* **25**, 1258 (1992).

[5] H. Masuda and K. Fukuda, *Science* **268**, 1466 (1995).

[6] H. Masuda, H. Yamada, M. Saitoh, H. Asoh, M. Nakao and T. Tamamura, *Appl. Phys. Lett.* **71**, 2770 (1997).

[7] S. Bandyopadhyay, A. E. Miller, H. C. Chang, G. Banerjee, V. Yuzhakov, D. –F. Yue, , R. E. Ricker, J. A. Eastman, E. Baugher and M. Chandrasekhar, *Nanotechnology* **7**, 360 (1996).

[8] O. Jessensky, F. Muller and U. Gosele, *Appl. Phys. Lett.* **72**, 1173 (1998).

[9] O. Jessensky, F. Muller and U. Gosele, *J. Electrochem. Soc.* **145**, 3735 (1998).

[10] K. Nielsch, J. Choi, K. Schwirn, R. B. Wehrspohn and U. Gosele, *Nano Lett.* **2**, 677 (2002).

[11] W. Lee, R. Ji, U. Gösele and K. Nielsch, *Nat. Mater.*, **5**, 741 (2006).

[12] V. Zwilling, M. Aucouturier and E. Darque-Ceretti, *Electrochim. Acta*, **45**, 921(1999)

[13] V. Zwilling, E. Darque-Ceretti, A. Boutry-Forveille, M. Y. Perrin and M. Aucouturier, *Surf. Interface Anal.* **27**, 629 (1999).

[14] D. Gong, C. A. Grimes, O. K. Varghese, W. Hu, R. S. Singh, Z. Chen and E. C. Dickey, *J. Mater. Res.*, **16**, 3331 (2001).

[15] Q. Cai, M. Paulose, O. K. Varghese and C. A. Grimes, *J. Mater. Res.* **20**, 230 (2005).

[16] E. Balaur, J. M. Macak, H. Tsuchiya and P. Schmuki, *J. Mater. Chem.* **15**, 4488 (2006).

[17] M. Paulose, K. Shankar, S. Yoriya, H. E. Prakasam, O. K. Varghese, G. K. Mor, T. J. Latempa, A. Fitzgerald and C. A. Grimes, *J. Phys. Chem. B* **110**, 16179 (2006).

[18] C. Ruan, M. Paulose, O. K. Varghese, G. K. Mor and C. A. Grimes, *J. Phys. Chem. B* **109**, 15754 (2005).

[19] S. Yoriya, H. E. Prakasam, O. K. Varghese, K. Shankar, M. Paulose, G. K. Mor, T. J. Latempa and C. A. Grimes, *Sens. Lett.* **4**, 334 (2006).

[20] K. Shankar, G. K. Mor, A. Fitzgerald and C. A. Grimes, *J. Phys. Chem. C* **111**, 21 (2007).

[21] H. E. Prakasam, K. Shankar, M. Paulose and C. A. Grimes, *J. Phys. Chem. C* **111**, 7235 (2007).

[22] R. Hahn, J. M. Macak and P. Schmuki, *Electrochem. Commun.* **9**, 947 (2007).

[23] Ch. Richter, Z. Wu, E. Panaitescu, R. J. Willey and L. Menon, *Adv Mater.* **19**, 946 (2007).

[24] R. M. Bozorth, *Ferromagnetism* (IEEE, New York, 1993).

[25] H. R. Khan and K. Petrikowski, *J. Magn. Magn. Mater.* **249**, 458 (2002).

[26] M. Vázquez, K. Pirota, M. Hernández-Vélez, V.M. Prida, D. Navas, R. Sanz, F. Batallán and J. Velázquez, *J. Appl. Phys.* **95**, 6642 (2004).

[27] K. Nielsch, R. B. Wehrspohn, J. Barthel, J. Kirschner, U. Gösele, S. F. Fischer and H. Kronmüller, *Appl. Phys. Lett.* **79**, 1360 (2001).

[28] M. Vázquez, K. Pirota, J. Torrejón, D. Navas and M. Hernández-Vélez, *J. Magn. Magn. Mater.* **294**,174 (2005).

[29] J. Escrig, R. Lavín, J.L. Palma, J.C. Denardin, D. Altbir, A. Cortés and H. Gómez, *Nanotechnology* **19**, 075713 (2008).

[30] M. Ohnuma, K. Hono, H. Onodera, S. Ohnuma, H. Fujimori and J. S. Pedersen, *J. Appl. Phys.* **87**, 817 (2000).

[31] G. Herzer, *IEEE Trans. Magn.* **25**, 3327 (1989).

[32] G. Herzer, *IEEE Trans. Magn.* **26**, 1397 (1990).

[33] G. Herzer, *Mater. Sci. Eng., A* **133**, 1 (1991).

[34] A. O. Adeyeye, J. A. C. Bland, and C. Daboo, *Appl. Phys. Lett.* **70**, 3164 (1997).

[35] W. Y. Lee, H. T. Leung, W. Zhang, Y. B. Xu, A. Hirohata, C. C.Yao, B.-Ch. Choi, D. G. Hasko, and J. A. C. Bland, *IEEE Trans. Magn.* **35**, 3475 (1999).

[36] C. C. Wang, A. O. Adeyeye, and Y. H. Wu, *J. Appl. Phys.* **94**, 6644 (2003).

[37] A. Yu. Toporov, R. M. Langford, and A. K. Petford-Long, *Appl. Phys. Lett.* **77**, 3063 (2000).

[38] P. Vavassori, G. Gubbiotti, G. Zangari, C. T. Yu , H. Yin, H. Jiang and G. J. Mankey, *J. Appl. Phys.* **91** 7992 (2002).

[39] R. P. Cowburn, A.O. Adeyeye and J. A. C. Bland, *J. Magn. Magn. Mater.* **173**, 193 (1997).

[40] W.H. Meiklejohn and C.P. Bean, *Phys. Rev.* **102**, 1413 (1956).

[41] W.H. Meiklejohn, and C.P. Bean, *Phys. Rev.* **105**, 904 (1957).

[42] S. S. P. Parkin, X. Jiang, C. Kaiser, A. Panchula, K. Roche, and M. Samant, *Proc. IEEE* **91**, 661 (2003).

[43] K. Fukamichi, *J. Magn. Soc. Japan* **21**, 1062 (1997).

[44] R. Jungblut, R. Coehoorn, M. T. Johnson, J. aan de Stegge and A. Reinders, *J. Appl. Phys.* **75**, 6659 (1994).

[45] M. Takahashi, A. Yanai, S. Taguchi and T. Suzuki, *Jpn. J. Appl. Phys.* **19**, 1093 (1980).

[46] M. Fraune, U. Rüdiger, G. Güntherodt, S. Cardoso, and P. Freitas, *Appl. Phys. Lett.* **77**, 3815 (2000).

[47] K. Liu, S. M. Baker, M. Tuominen, T. P. Russell, and I. K. Schuller, *Phys. Rev. B* **63**, 060403 (2001).

[48] M. I. Montero, K. Liu, O. M. Stoll, A. Hoffmann, J. J. Akerman, J. I. Martin, J. L. Vicent, S. M. Baker, T. P. Russell, C. Leighton, J. Nogués, and I. K. Schuller, *J. Phys. D* **35**, 2398 (2002).

[49] K. M. Coakley, B. S. Srinivasan, J. M. Ziebarth, C. Goh, Y. X. Liu and M. D. McGehee, *Adv. Funct. Mater.* **15**, 1927 (2005).

[50] G. M. Wang, T. Hirasa, D. Moses and A. J. Heeger, *Synth. Met.* **146**, 127 (2004).

[51] J. Park, S. Lee, and H. H. Lee, *Org. Electron.* **7**, 256 (2006).

[52] P. Schilinsky, C. Waldauf and C. J. Brabec, *Adv. Funct. Mater.* **16**, 1669 (2006).

[53] H. Sirringhaus, T. Kawase, R. H. Friend, T. Shimoda, M. Inbasekaran, W. Wu and E. P. Woo, *Science* **290**, 2123–2126 (2000).

[54] S. E. Shaheen, R. Radspinner, N. Peyghambarian and G. E. Jabbour, *Appl. Phys. Lett.* **79**, 2996 (2001).

[55] K. M. Coakley, Y. Liu, M. D. McGehee, K. L. Frindell, and G. D. Stucky, *Adv. Funct. Mater.* **13**, 301 (2003).

[56] G. P. Bartholomew and A. J. Heeger, *Adv. Funct. Mater.* **15**, 677 (2005).

[57] P. Atienzar, T. Ishwara, M. Horie, J. R. Durrant, and J. Nelson, *J. Mater. Chem.* **19**, 5377 (2009).

[58] S. Tepavcevic, S. B. Darling, N. M. Dimitrijevic, T. Rajh, and S. J. Sibener, *Small* **5**, 1776 (2009).

[59] G. K. Mor, O. K. Varghese, M. Paulose and C. A. Grimes, *Adv. Funct. Mater.* **15**, 1291(2005).

[60] J. M. Macak, H. Tsuchiya, S. Berger, S. Bauer, S. Fujimoto and P. Schmuki, *Chem. Phys. Lett.* **428**, 421 (2006).

[61] D. J. Yang, H. G. Kim, S. J. Cho and W. Y. Choi, *IEEE Trans. Nanotechnol.* **7**, 131 (2008).

[62] A. Z. Sadek, H. Zheng, K. Latham, W. Wlodarski and K. K. Zadeh, *Langmuir* **25**, 509 (2009).

[63] J. Wang and Z. Lin, *J. Phys. Chem. C* **113**, 4026 (2009).

[64] P. Xiao, Y. H. Zhang, X. X. Zhang and G. Z. Cao, *J. Inorg. Mater.* **25**, 32 (2010).

[65] Y. X. Tang, J. Tao, Y. Y. Zhang, T. Wu, H. J. Tao and Z. G. Bao, *Acta Phys.-Chim. Sinica* **24** 2191(2008).

[66] Y. X. Tang, J. Tao, H. J. Tao, T. Wu, L. Wang, Y. Y. Zhang, Z. L. Li and X. L. Tian, *Acta Phys.-Chim. Sinica* **24**, 1120 (2008).

[67] H. D. Zheng, A. Z. Sadek, M. Breedon, D. Yao, K. Latham, J. du Plessis, K. Kalantar- Zadeh, *Electrochem. Commun.* **11**, 1308 (2009).

[68] Z. Li and S. F. Zhang, *Phys. Rev. B* **61**, R14897 (2000).

Chapter 2 Fabrication and characterization

2.1 Introduction

This chapter discusses the major experiment techniques used in this research work. Aluminum oxide template and titanium oxide nanotube arrays were fabricated via anodization of aluminum and titanium respectively. Magnetic nanowires were electrodeposited into pores of the aluminum oxide templates with AC voltage. RF sputtering was used to deposit magnetic film perforated with holes (known as antidot arrays) on top of the aluminum oxide templates and titanium thin films onto indium tin oxide substrates.

We studied the magnetic properties of the magnetic nanowires and antidot arrays with vibrating sample magnetometer and M-H loop tracer. Magnetoresistance of the antidot array was measured by using four point probe method. Permeability of the magnetic antidot was measured by using microwave measurement with a technique known as shorted microstrip transmission-line perturbation. Optical properties of different TiO_2 nanotube structures fabricated were investigated with UV-Vis absorption spectrometer.

2.2 Preparation of aluminum oxide templates, titanium oxide nanotubes and magnetic nanowires and deposition of thin film

2.2.1 Aluminum oxide template and titanium oxide nanotube array via anodization

In 1970s, several authors, including O'Sullivan & Wood [1] and Thompson et al [2], discussed the pore formation in aluminum oxide templates based on electrical field assisted dissolution of the oxide. In 1992, Parkhutik and Shershulsky presented a mathematical theory for single pore growth [3]. Fig. 2.1 shows a schematic diagram of

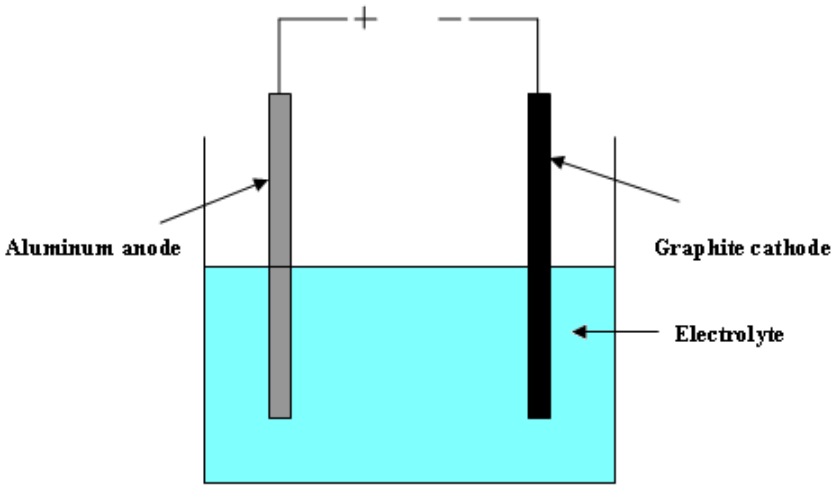

Fig. 2.1 Illustrative drawing of a two electrode electrochemical cell in which aluminum is anodized.

the set up used for anodizing aluminum foil using two electrode electrochemical cell. The two main processes that took place in the pore formation are (i) the growth of aluminum oxide at the interface between aluminum and aluminum oxide due to the transport of Al^{3+}, OH^- and O^{2-} ions within the aluminum oxide film and (ii) the dissolution of the aluminum oxide at the interface between the aluminum oxide film and electrolyte.

Fig. 2.2 shows schematic evolution of the aluminum oxide template anodized at constant voltage. At the beginning of the anodization, a thin oxide layer is formed due to the interaction of Al^{3+} ion from Al surface with O^{2-} ions present in the electrolyte. The O^{2-} ions come from the water due to its splitting. Electric field is formed across the oxide layer, causing the Al^{3+} ions to move from metal/oxide layer interface towards the oxide/electrolyte interface and O^{2-} ions to move from oxide/electrolyte interface towards

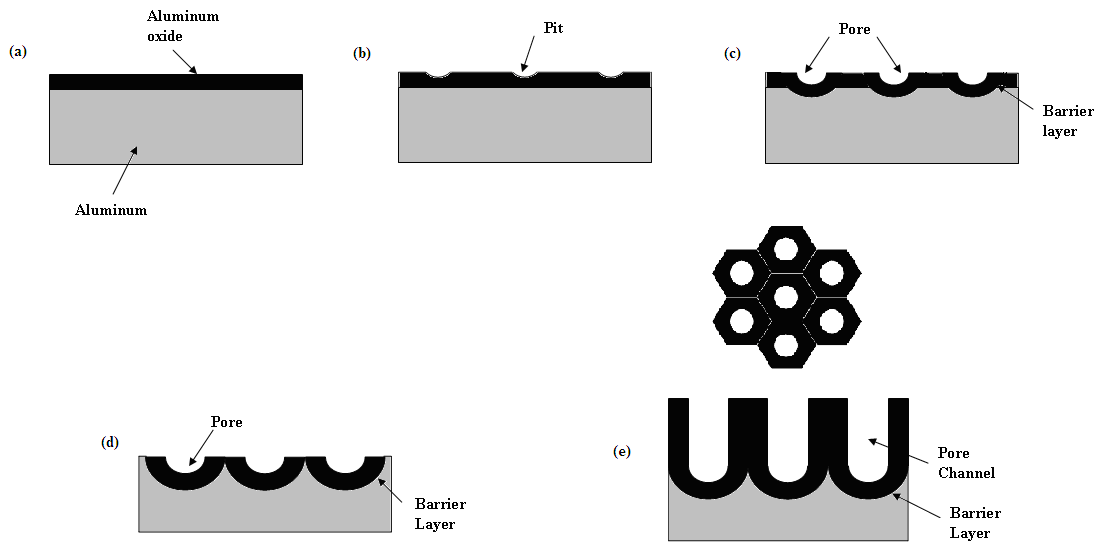

Fig. 2.2 Schematic diagram of the evolution of anodic aluminum oxide template at a constant voltage: (a) oxide layer formation, (b) pit formation on the oxide layer, (c) growth of the pit into scallop shaped pore, (d) lateral expansion of scallop shaped pore until they merge and (e) fully developed anodic aluminum oxide template with a corresponding top view with steady state film growth.

the metal/oxide interface, resulting in the growth of oxide at both the oxide/electrolyte interface and metal/oxide interface. As the thickness increases, the electric field across the oxide decreases and this will limit the growth of the oxide layer. At the same time, the current density will fall rapidly to a value such that oxide can only develop at the metal/oxide interface but not at the oxide/electrolyte interface because all Al^{3+} ions are directly ejected into the electrolyte [4]. This is a necessary condition for porous aluminum oxide template formation, otherwise outwardly mobile Al^{3+} ions forming oxide at the oxide/electrolyte interface will “heal” any developing pores.

The distribution of the electric field in the oxide is however correlated with the surface morphological fluctuations. More focused electric field is concentrated at the

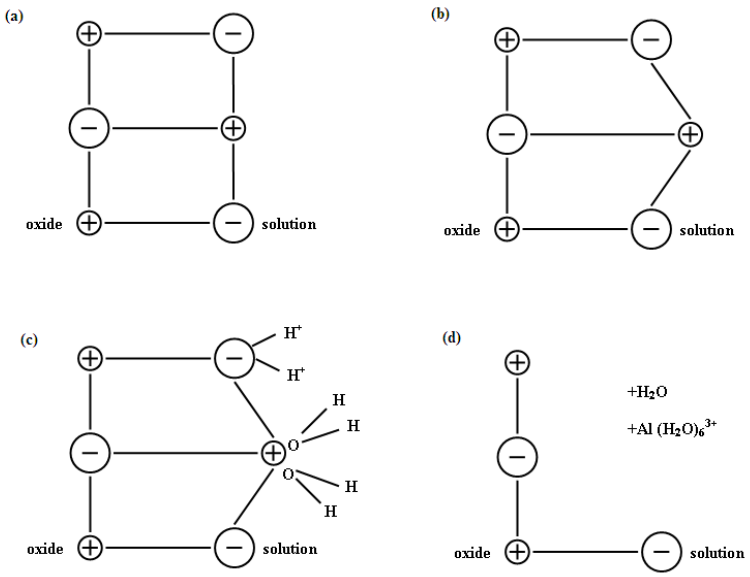

Fig. 2.3 Schematic representation of field-assisted dissolution of $A1_2O_3$: (a) before polarization, (b) after polarization, (c) removal of $A1^{3+}$ and O^{2-} ions, and (d) the remaining oxide with overall reaction being represented as $Al_2O_3 + 6H^+ \rightarrow 3H_2O + 2Al^{3+}$.

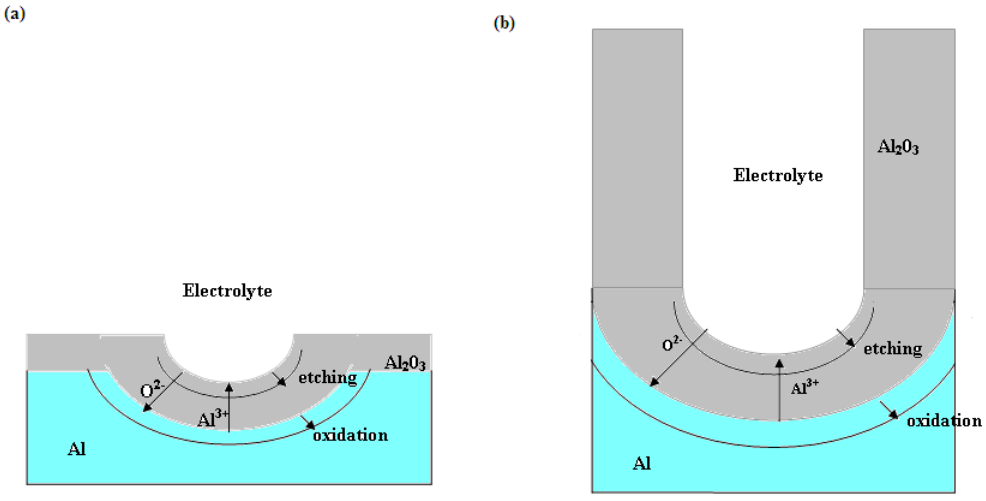

Fig. 2.4 Schematic diagram to show the etching of oxide and the growth of oxide (a) of Fig. 2.2(c) and (b) of Fig. 2.2(e).

surface with pronounced morphological fluctuation. This will result in field enhanced dissolution of oxide (illustrated in Fig. 2.3) at the oxide/electrolyte interface in these areas which will develop into pits as shown in Fig. 2.2(b). Due to the lateral component of the enhanced electric field, the pit will be enlarged to form pores as shown in Fig. 2.2(c) with continuous oxide growth occurring at the pit/ metal interface and dissolution of oxide at the pit/electrolyte interface. These pores will grow laterally and downward until they merge as shown in Fig. 2.2(d). Finally, steady state growth of the anodic aluminum oxide template occurs as shown in Fig. 2.2(e). The electric field is highly localized across the barrier layer, resulting in a field enhanced dissolution of the oxide at the interface of pore base/electrolyte and growth of oxide at the interface of pore base/metal. As a consequence, the pores will grow downward into the metal substrate. Under a steady state condition, the resultant pore diameter and cell size remain unchanged and vary linearly with the applied voltage. This results from a self-adjusting pore growth. When the pores become too large, radius of the curvature decreases and the field assisted dissolution decreases, so that the radius will subsequently decrease back to equilibrium value. Thus, in essence, film formation occurs at a constant rate, being determined by the average field. It is balanced by the field-assisted dissolution, at a rate determined by the local field, related to the radius of curvature of the pore base.

The synthesis and formation mechanisms of the titanium oxide nanotubes on titanium metal by anodization [5-7] are governed essentially by the same self-ordering principle and growth mechanisms that are in play when highly ordered aluminum oxide templates are grown anodically on aluminum surfaces. Fig. 2.5 shows a schematic diagram of evolution of TiO_2 nanotubes via anodization of titanium foil. For titanium, in

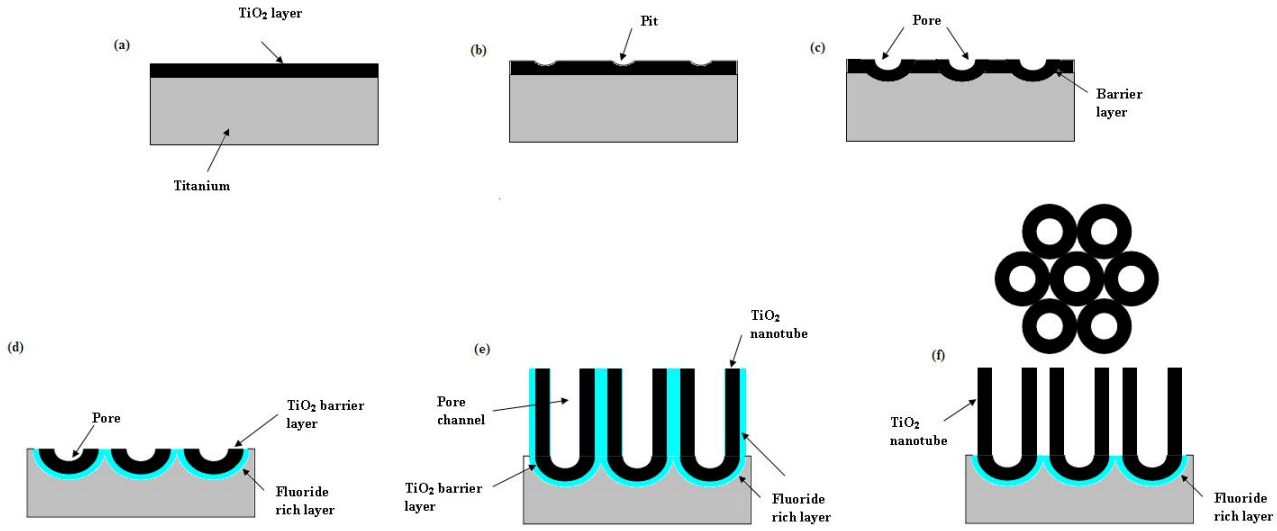

Fig. 2.5 Schematic diagram of evolution of titanium oxide nanotubes at a constant voltage: (a) oxide layer formation, (b) pit formation on the oxide layer, (c) growth of the pit into scallop shaped pore, (d) lateral expansion of scallop shaped pore until they merge and (e) fully developed titanium oxide nanotubes at steady state film growth, (f) corrosion of the fluoride rich layer by the electrolyte and formation of separated nanotube array with a corresponding top view.

contrast to aluminum, a low pH is not sufficient to create porous oxide. The presence of F^- ion is necessary for the mild but permanent chemical dissolution of TiO_2 so that TiO_2 nanotubes instead of compact layers are formed during the anodization. As mentioned earlier in this section, the oxide growth is controlled by the field-assisted ions transport (O^{2-} and Ti^{4+}) through the growing oxide layer. Due to the enhanced electric field across the barrier layer of each nanotube, O^{2-} ions formed from the splitting of H_2O will migrate from electrolyte/oxide interface to titanium/oxide interface to form TiO_2 while the Ti^{4+} ions will migrate from metal/oxide interface to oxide/electrolyte interface and are solvatized by the F^- ions to form water soluble TiF_6^{2-} complexes. At the same time, the tube base at the oxide/electrolyte interface will undergo field assisted dissolution which is presented by the reaction: $TiO_2 + 6F^- + 4H^+ \rightarrow TiF_6^{2-} + H_2O$.

In contrast to the porous structure in the aluminum oxide template obtained via anodization of aluminum, titanium oxide nanotube array with separated individual nanotubes which are shown in Fig. 2.5(f) is formed via anodization of titanium [8]. Due to the electric field across the barrier layer, F^- ions will migrate across the oxide layer from the electrolyte to the metal/oxide interface to form fluoride rich layer coating around the outermost wall of each TiO_2 nanotube. This fluoride rich layer is prone to chemical dissolution [8]. Depending on the solubility of this fluoride rich layer, the morphology can change from nanoporous to nanotubular. As a consequence, this can account for the hexagonal ordered nanoporous appearance at the bottom of TiO_2 nanotubes and the hexagonal structure continuously converts to a tubular shape towards the top of the TiO_2 nanotubes.

The length of aluminum oxide template increases with the duration of anodization until the aluminum is completely depleted, but this is not the case for titanium oxide nanotubes. The length of the nanotube will increase with duration of anodization for certain period of time after which it will remain more or less constant [9]. In addition to the oxide growth at the tube base, chemical dissolution occurs over the entire length of the nanotube. When the oxide growth rate at the tube base is equaled to the chemical etching at the top of the TiO_2 nanotube, length of the TiO_2 nanotube will stop increasing and remain constant. To achieve longer nanotube, low electrolyte acidity and low fluoride concentration should be used to reduce the dissolution rate. If the titanium is anodized for an extended period of time, wall of the tube will be thinned out and eventually the top of the tube will be covered with ‘’grassy” layer due to the collapsed tubes.

2.2.2 Nanowires by AC electrodeposition

The electrodeposition by direct current is very unstable and uniform filling of the pores cannot be achieved with the barrier layer remained intact at the base of the pore of aluminum oxide template. This is due to the partial removal of the barrier layer with the increment of pH occurring at the cathodic side [10]. Once a pore loses its barrier layer the resistance decreases significantly and the cathodic current passes from this pore preferably and the deposition occurs locally in this pore.

Special electrical properties of barrier layer allow alternating current (AC) to be used in the electrodeposition of nanowire in aluminum oxide templates. There is Al^{3+} deficit in its lattice at the interface of barrier layer and electrolyte and O^{2-} deficit at the interface of barrier layer and aluminum. Thus, it can function as a couple of N and P junctions, which rectifies the current like a diode. Deposition of nanowires in the pores of the aluminum oxide templates occurs normally at the cathodic half cycle. In the next anodic half cycle, the current drops to zero and polarization decreases and damaged points of the barrier layer can be repaired [11].

2.2.3 RF sputtering of thin film on substrate

The process of ejecting atoms from surface of a material (target) by bombardment of positive ions, which are usually inert, is known as sputtering. The plasma contains positive ions and electrons of the inert gas which is ionized due to the voltage applied across the electrodes. The ejected atoms from the target will coat onto the substrate to form thin film. The sputtering discharge cannot be sustained if the target used is an insulator since it will store positive ions and eventually will repel the bombarding positive ions. This problem can be overcome by applying rf power across the electrodes.

In the positive half cycle, the insulating target will collect large current of electrons which tend to charge the insulator negatively. In the negative half cycle, the insulating target will collect the positive bombarding ions but this ion current is smaller than the electron current. This is due to smaller mass of the electron as compared to that of the positive ions. Thus, a dc bias is produced on the target which is still negatively charged and will attract bombarding positive ions. If a metal is used as target in the rf sputtering, a capacitor of matching network circuit is required.

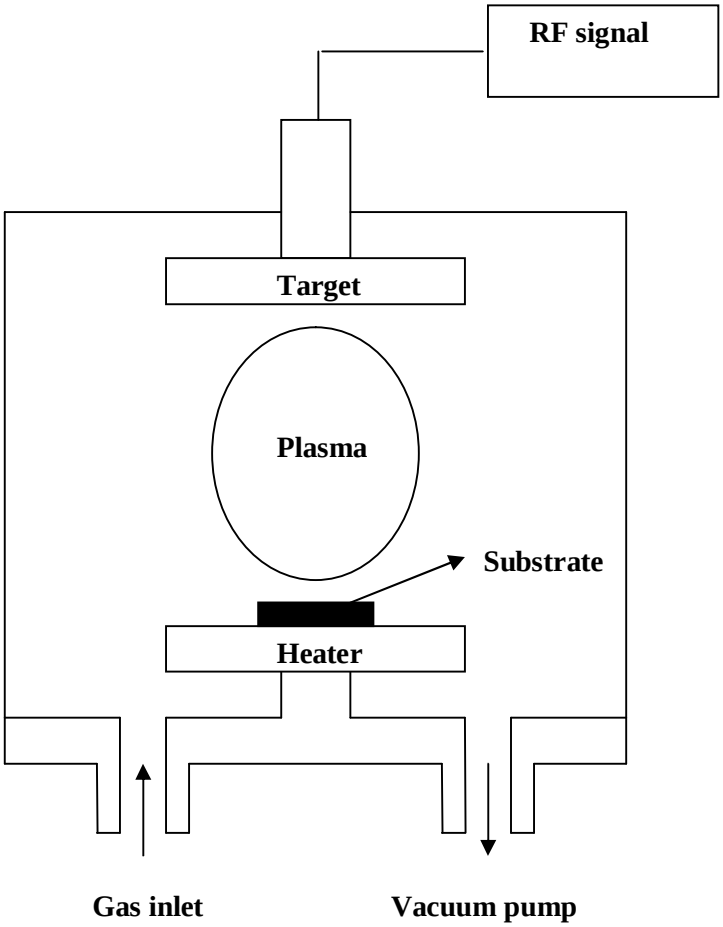

Fig. 2.6 Schematic drawing of the RF sputtering system.

2.3 Measurement techniques

2.3.1 Structural characterization

2.3.1.1 Transmission electron microscopy

Transmission electron microscopy (TEM) is a technique used for imaging a sample with thickness of at most 100 nm. Electrons which are emitted from fine tungsten by thermionic emission will be collected by application of high voltages. A beam of high energy electron from 1 keV to 1 MeV is first focused by a series of magnetic lenses in a vacuum chamber before it is transmitted through the sample. The transmitted elastically scattered (diffracted) electron will be collected by a fluorescent screen to form images of the samples with resolution down to atomic scale.

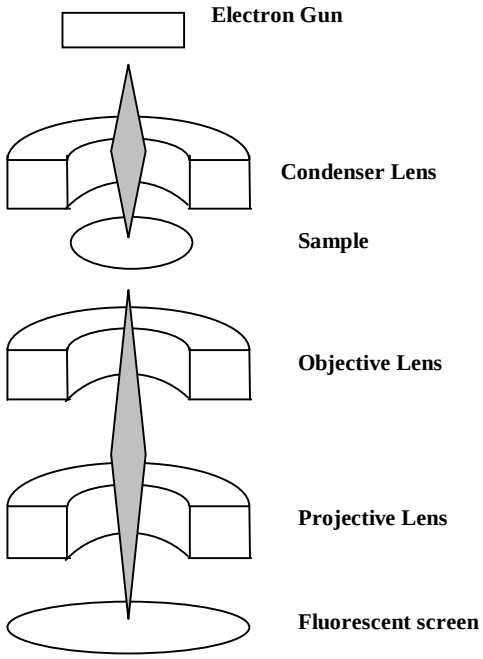

Fig. 2.7 Schematic drawing of a transmission electron microscope.

2.3.1.2 Field emission scanning electron microscopy

Field emission scanning electron microscopy (FESEM) can be used to investigate surface morphology and cross-section morphology of a sample. In SEM characterization method, electrons which are emitted from fine tungsten by thermionic emission will be accelerated by application of high voltages. These high energy electrons are focused through a series of magnetic lenses in a vacuum chamber before it bombards onto the samples. Low energy secondary electrons (<50eV) resulted from inelastic scattering of electrons with sample atoms are collected and analyzed by scintillator. Due to their low energy, these secondary electrons typically originate from surface of the sample and the images formed normally reflect surface morphology of the sample.

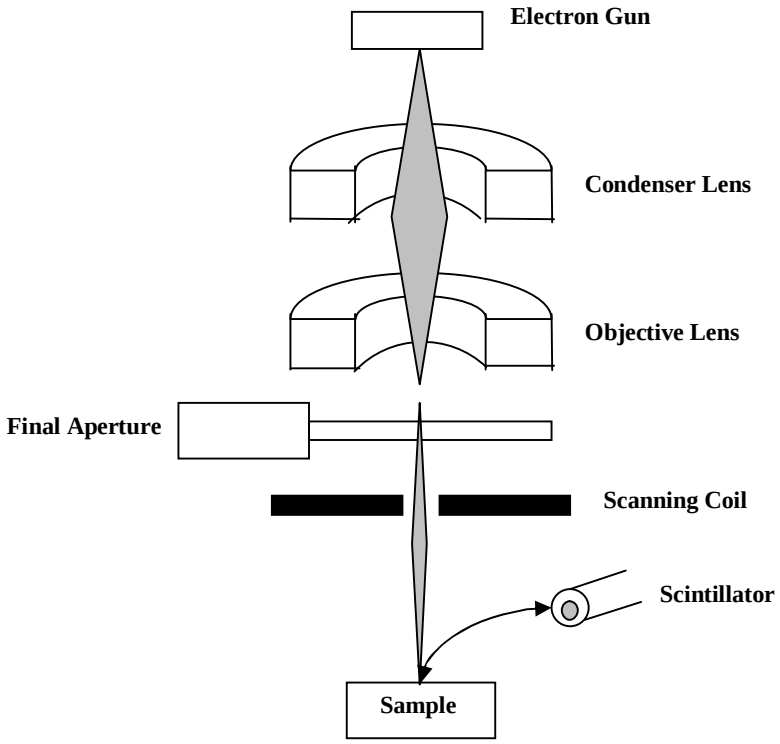

Fig. 2.8 Schematic drawing of a scanning electron microscope.

2.3.1.3 X-ray diffraction

X-ray diffraction (XRD) can be used to determine crystal structure of a material. Gonio (θ-2θ) scan is used to identify the out of plane crystal orientation of thin films. The X-ray is produced by impinging a copper target with high energy electron beam. The X-ray is then incidented onto the sample with an angle to the normal of the film surface. Crystal lattice of the sample will diffract X-rays and intensity of the diffracted X-ray is measured. The result is compared with standard powder diffraction files to identify phase composition, crystal orientation and lattice parameters of the films.

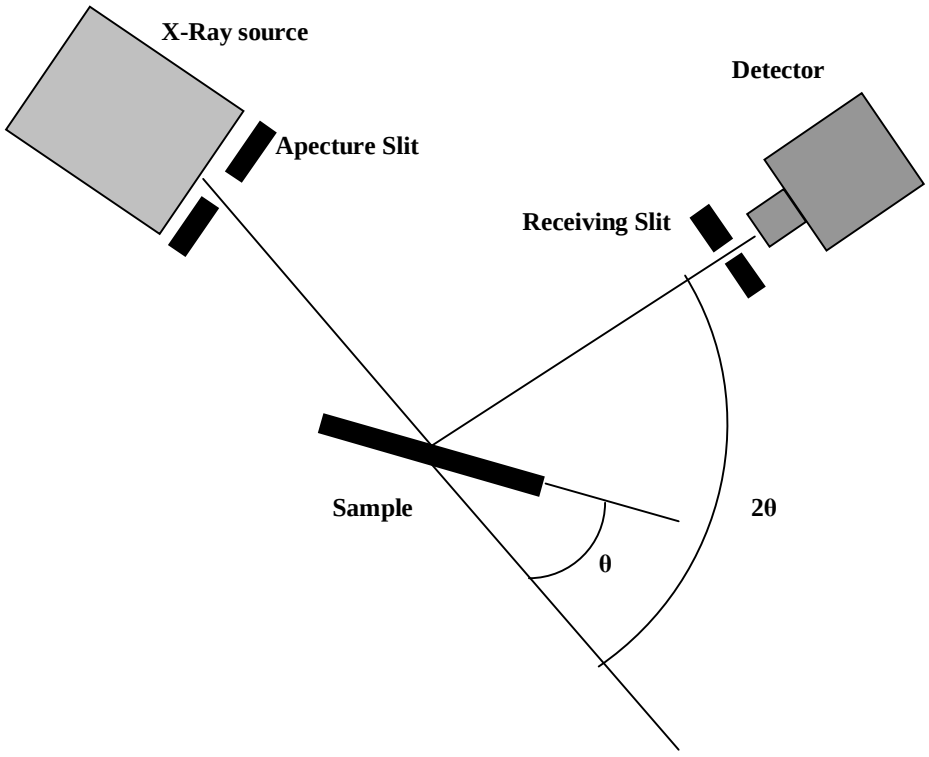

Fig. 2.9 X-ray diffraction θ-2θ scan.

2.3.2 Magnetization measurement

Vibrating sample magnetometer (VSM) and M-H loop tracer measure magnetic induction and magnetization based on Faraday Law's law:

$$V = -N\frac{d\Phi}{dt} = -NA\frac{dB}{dt}$$

$$B = -\frac{1}{NA}\int V dt$$

where V is the voltage induced in the circuit, Φ is the magnetic flux passing through a coil of N turns, $d\Phi/dt$ is the rate of the change of the flux, A is the cross-section area of the coil, and B is the magnetic induction. Faraday's law describes that the voltage induced in an electrical loop circuit is proportional to the rate of change of magnetic flux linking the circuit.

2.3.2.1 M-H loop tracer

M-H loop tracer is an instrument which measures magnetization of a sample according to the applied magnetic field. The M-H loop tracer used here is highly sensitive and is used extensively for the measurement of magnetic properties of soft magnetic materials, but is not suitable for measurement of hard magnetic materials since the maximum applied field is only 200 Oe. An external magnetic field is applied to magnetize the sample while it is placed within pick up coil. This pick up coil is located within a large driving coil which will provide a sinusoidal varying magnetic field.

A neutralizing coil which is identical with the pick-up coil is required to cancel out the voltage induced by the alternating driving field. The signal from the pick-up coil and the neutralizing coil is integrated by the appropriate network to find the magnetization of the

sample magnetized by the applied field.

2.3.2.2 Vibrating-sample magnetometer

Vibrating-sample magnetometer (VSM) can be used to measure magnetization of a sample as a function of applied magnetic field. VSM is suitable for measurement of magnetization hysteresis loop of magnetic hard materials whose coercivity is larger than 50 Oe. The sample is placed in a magnetic field and is subjected to a sinusoidal vibration motion during the measurement. Therefore, the voltage, which is induced in the pick-up coils, is proportional to the magnetic moment of the sample. Since VSM measures the difference in magnetic induction in a region of space between with and without the specimen, it can directly measure magnetization of the sample and is well suited for the determination of the saturation magnetization.

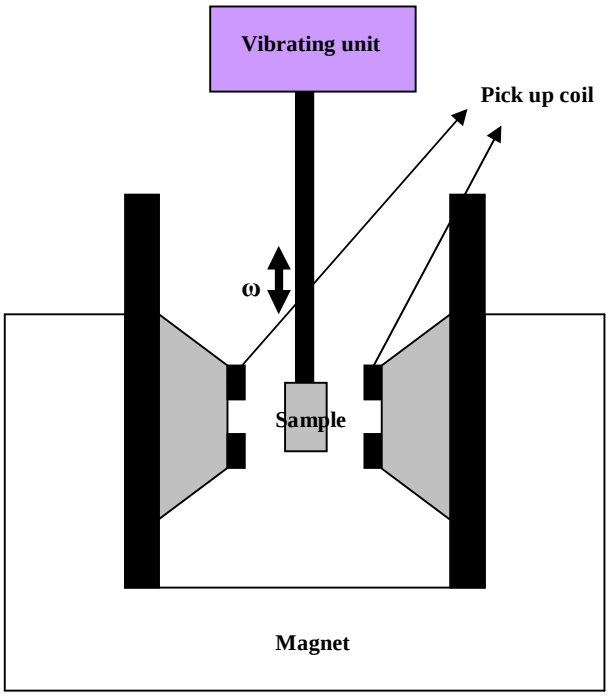

Fig. 2.10 Schematic drawing of vibrating sample magnetometer.

2.3.3 Permeability measurement by shorted microstrip transmission-line perturbation

Permeability of magnetic films was measured by using shorted microstrip transmission-line perturbation method. In this case, the magnetic thin films coated on dielectric substrate under measurement are inserted into a segment of a transmission line. In the reflection approach shown in Fig. 2.11, the transmission line is short circuited, and the magnetic thin film on the substrate is placed at a position close to the shorted end of the transmission line where the magnetic field dominates. The discontinuities of the characteristic parameters along the transmission line affect the reflection coefficient (S_{11}) of this one-port network. In the calculation of complex permeability of the magnetic thin film, we compared the transmission line loaded with a dielectric substrate without magnetic thin film and the transmission line loaded with a magnetic thin film coated on dielectric substrate. We assumed that the two substrates in these two cases have the same dimensions and the same dielectric properties, are nonmagnetic and they are placed at the same position in the transmission line.

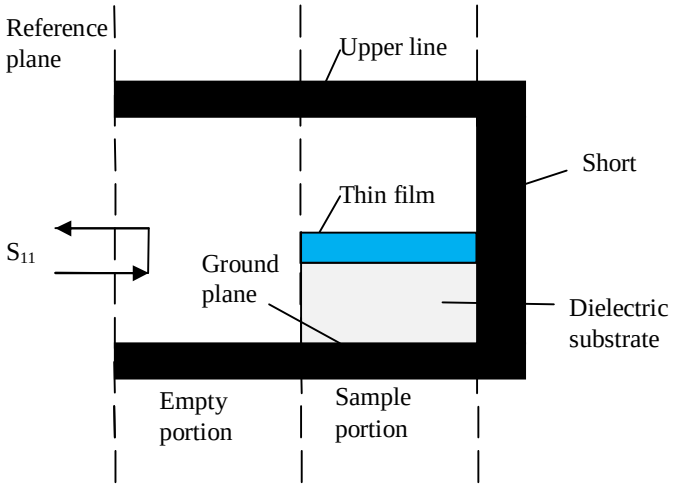

Fig. 2.11 Microstrip circuits for characterization of magnetic thin films using reflection approach.

The following algorithms are used to calculate permeability of the magnetic thin film in a short-circuited planar transmission line [12]:

1. Effective permittivity of the empty transmission line without any substrate can be be obtained from the reflection coefficient measured at starting point of the transmission line:

$$\varepsilon_{eff}^{empty}(f)=\left(\frac{jc_0 In\left[-S_{11}^{empty}(f)\right]}{4\pi f\left(l_{empty}+l_{sample}\right)}\right)^2$$

where $S_{11}^{empty}(f)$ is the reflection coefficient of an empty transmission line, l_{sample} is length of the sample portion, l_{empty} is length of the empty portion, f is measurement frequency and c_0 is the speed of light in free space.

2. Effective permittivity of the transmission line loaded with substrate without coating of thin film can be obtained from the reflection coefficient measured at the starting point of transmission line:

$$\varepsilon_{eff}^{sub}(f)=\left(\frac{jc_0 In\left(-S_{11}^{sub}(f)\right)}{4\pi fl_{sample}}-\frac{l_{empty}\sqrt{\varepsilon_{eff}^{empty}(f)}}{l_{sample}}\right)^2$$

where $S_{11}^{sub}(f)$ is reflection coefficient of the transmission line loaded with substrate without coating of thin film.

3. Effective permeability of the transmission line loaded with magnetic thin film coated on substrate can be obtained from the reflection coefficient measured at the starting point of the transmission line:

$$\mu_{eff}(f)=\left(\frac{jc_0 In\left(-S_{11}^{film}(f)\right)}{4\pi fl_{sample}\sqrt{\varepsilon_{eff}^{sub}(f)}}-\frac{l_{empty}\sqrt{\varepsilon_{eff}^{empty}(f)}}{l_{sample}\sqrt{\varepsilon_{eff}^{sub}(f)}}\right)^2$$

where $S_{11}^{film}(f)$ is reflection coefficient of the transmission line loaded with magnetic thin film coated on substrate.

4. Permeability of the magnetic thin film can be obtained from the effective permeability of the transmission line loaded with the magnetic thin film coated on substrate:

$$\mu_{film}(f) = \frac{K}{t}\left[\mu_{eff}(f) - 1\right]$$

where t is thickness of the thin film under test, and K is scaling coefficient of the shorted transmission line, which is determined by structure of the short transmission line and is independent of the thin film under test. The scaling coefficient K can be obtained by calibrating the shorted transmission line with a standard sample whose permeability is known, or by adjusting the real part of the complex permeability at low frequency to fit the value of initial permeability determined by

$$\mu_{inital}^{'}(f) = \frac{M_s}{H_a} + 1,$$

where M_s is saturation magnetization and H_a is anisotropic field of the magnetic thin film under test.

2.3.4 Electrical resistivity measurement

In order to eliminate the measurement error due to contact resistance, four-point measurement was used to measure the resistance of the magnetic thin films. Fig. 2.12 illustrates a circuit diagram of the four point measurement setup. In this setup, a high-input-resistance voltmeter, which draws negligible current, is used to measure the voltage

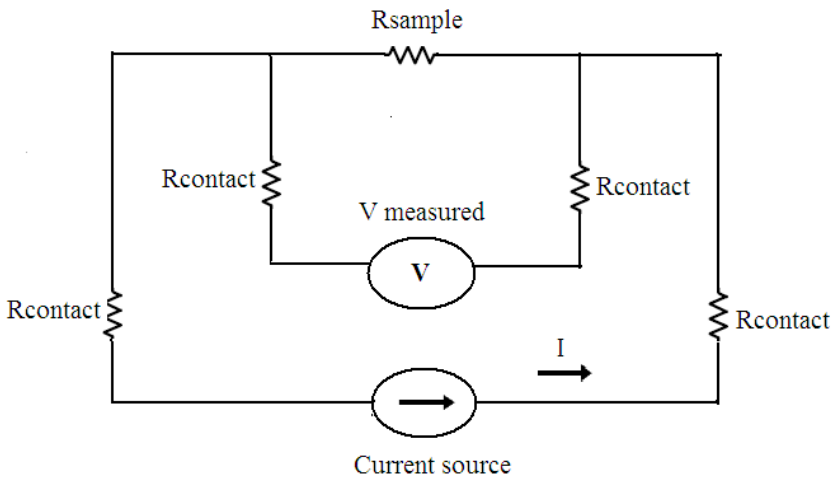

Fig. 2.12 A circuit diagram illustrating the four-point measurement setup.

across the sample. Due to the high resistance of the voltmeter as compared to the resistance of the sample, the voltage measured by the voltmeter is almost the same as the voltage across the sample.

2.3.5 Optical absorption and transmission measurement

A beam of light from a visible and/or UV light source is separated into its component wavelengths by a prism or diffraction grating. Each monochromatic (single wavelength) beam in turn is split into two equal intensity beams by a half-mirrored device. One beam, the sample beam passes through the sample holder on which the film sample is stuck onto. The other beam, the reference beam, passes through the reference holder which is left empty. The intensities of these light beams are then measured by electronic detectors and compared. The intensity of the reference beam is defined as I_0. The intensity of the sample beam is defined as I. Over a short period of time, the spectrometer automatically scans all the component wavelengths. Usually, transmittance (I/I_0) or absorbance $\log (I_0/I)$ is plotted against the wavelength.

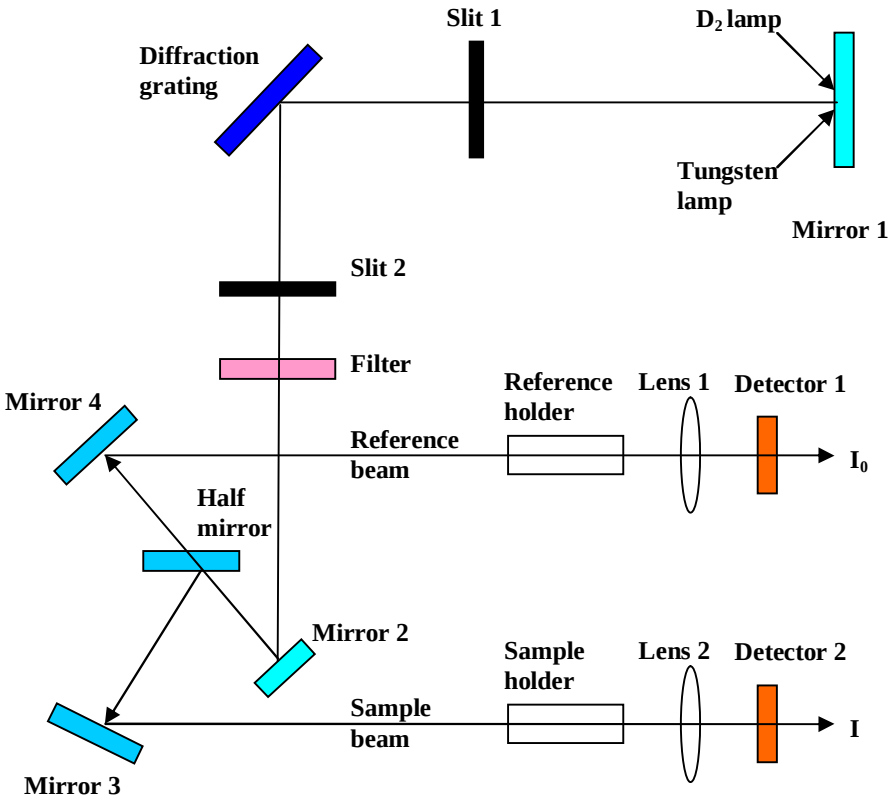

Fig. 2.13 Schematic drawing of UV-vis absorption spectrometer.

2.4 References

[1] J. P. O'Sullivan and G. C. Wood, *Proc. R. Soc.* **A317**, 511 (1970).

[2] G. E. Thompson, R. C. Furneaux, G. C. Wood, J.A. Richardson and J. S. Goode, *Nature* **272**, 433 (1978).

[3] V. P. Parkhutik and V. I. Shershulsky, *J. Phys. D: Appl. Phys.* **25**, 1258 (1992).

[4] G. E. Thompson, *Thin Solid Films* **297**, 192 (1997).

[5] G. K. Mor, O. K. Varghese, M. Paulose, K. Shankar and C. A. Grimes, *Sol. Energy Mater. Sol. Cells* **90**, 2011 (2006).

[6] J. M. Macak, H. Tsuchiya, A. Ghicov, K. Yasuda, R. Hahn, S. Bauer and P. Schmuki, *Curr. Op. Sol. State. Mater. Sci.* **11**, 3 (2007).

[7] A. Ghicov and P. Schmuki, *Chem. Commun.*, 2791 (2009).

[8] S. P. Albu, A. Ghicov, S. Aldabergenova, P. Drechsel, D. LeClere, G. E. Thompson, J. M. Macak and P. Schmuki, *Adv. Mater.* **20**, 4135 (2008).

[9] A. Ghicov, H. Tsuchiya, J. M. Macak and P. Schmuki, *Electrochem. Commun.* **7**, 505 (2005).

[10] N. Kallithrakas-Kontos, R. Moshohoritou, V. Ninni, I. Tsangaraki- Kaplanoglou, *Thin Solid Films* **326**, 166 (1998).

[11] P. M. Paulus, F. Luis, M. Kroll, G. Schmid and L. J. de Jongh, *J. Magn. Magn. Mater.* **224**, 180 (2001).

[12] Y. Liu, L.F. Chen, C. Y. Tan, H. J. Liu, and C. K. Ong, *Rev. Sci. Instrum.* **76**, 063911 (2005).

Chapter 3 Magnetic anisotropy

3.1 Introduction

The dependence of internal energy of a magnetic material on the direction of its spontaneous magnetization results in magnetic anisotropy. This phenomenon can be divided into various subcategories like, magnetocrystalline anisotropy, shape anisotropy, magnetoelastic anisotropy, uniaxial anisotropy, interface and volume anisotropy, exchange anisotropy and exchanged biased anisotropy. All these types of magnetic anisotropies will be discussed in the following subsections.

3.2 Magnetic anisotropy

3.2.1 Magnetocrystalline anisotropy (single ion anisotropy)

Magnetocrystalline anisotropy can be interpreted in terms of one ion model which assumes no ion interaction. It is discovered that spin-orbit interaction is responsible for the coupling of the spins to the crystal lattice via electronic clouds. In the absence of magnetic field, the energy of a single ion is minimized when the electron cloud takes particular orientation with respect to the crystalline field it is situated. The localized spins will also have preferred orientation with respect to the crystallographic axes that define the easy axis of magnetization since the spin is coupled to orbital state through the spin-orbit interaction. If magnetic field is applied, the spin will rotate from an easy axis and the electron charge cloud will be distorted as well through the spin-orbit interaction but still remains coupled to the lattice. The magnetocrystalline anisotropy is dependent on the orientation of magnetization relative to the crystal axes.

Phenomenologically, anisotropy energy density can be expressed as a function of

direction cosines of the magnetization vector with respect to crystal axes. For ferromagnetic crystal with cubic symmetry, the energy density is given as [1]

$$E = K_0 + K_1(\alpha_1^2\alpha_2^2 + \alpha_2^2\alpha_3^2 + \alpha_3^2\alpha_1^2) + K_2(\alpha_1^2\alpha_2^2\alpha_3^2) + K_3(\alpha_1^2\alpha_2^2 + \alpha_2^2\alpha_3^2 + \alpha_1^2\alpha_3^2)^2 + ... \quad ,$$

which α_i are referred to as direction cosines of magnetization along the cube edges and K_1, K_2 and K_3 are the anisotropy constant having a dimension of J/m^3.

For a crystal with hexagonal symmetry, the energy density can be expressed as [1]

$$E = K_0 + K_1 \sin^2\theta + K_2 \sin^4\theta + K_3 \sin^6\theta + K_4 \sin^6\theta \cos 6\phi + ... \quad ,$$

where θ is the angle between the hexagonal axis and the magnetization vector and ϕ is the angle between the magnetization component in the basal plane and one of the a axes. Döring derived and tabulated the expansion of magnetocrystalline anisotropy for all 32 crystallographic point groups [2].

3.2.2 Shape anisotropy

Magnetic stray field is produced by the magnetic body itself and contributes to the magnetostatic energy. This magnetostatic energy is mediated by dipolar interaction and is a long range effect. Assuming that the ferromagnetic object of finite size is uniformly magnetized, magnetostatic energy density of this object is given by $\frac{\mu_0}{2} N_{ij} M_i M_j$. The N_{ij} coefficients are the demagnetized coefficient of the body determined by the shape, resulting in shape anisotropy. The demagnetized coefficients along the three axes of the general ellipsoid have been tabulated by J. A. Osborn [3]. In the case of long cylindrical wires, thin disks or film, spheres and prolate ellipsoids, all the off diagonal terms are zero while all the N_{xx}, N_{yy} and N_{zz} are positive and will add up to 1. For a sphere, all three

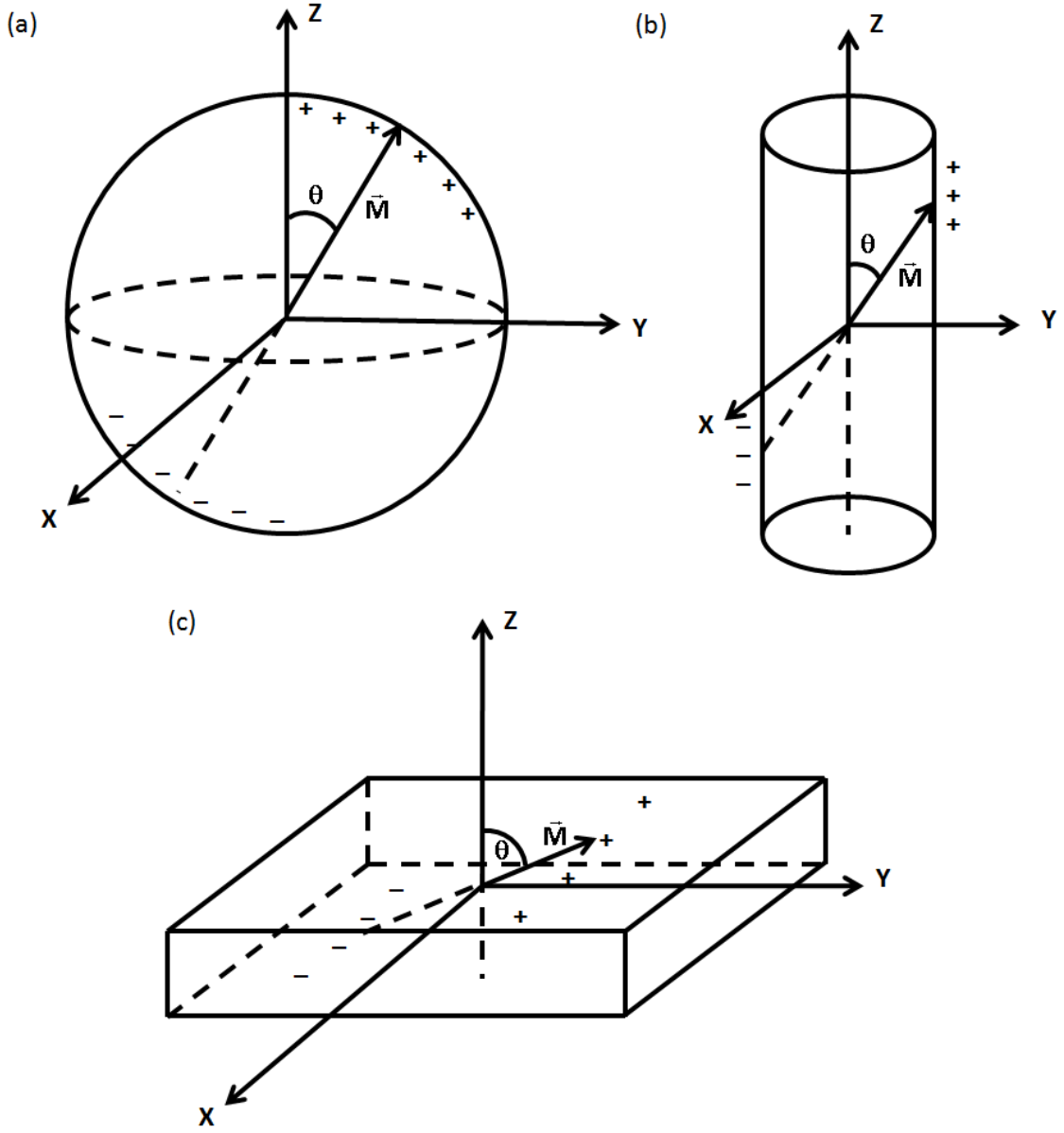

Fig. 3.1 Schematic diagram of uniform magnetization acting in: (a) sphere, (b) long cylindrical wire, and (c) thin film.

coefficients are equal to 1/3. For a thin disk or film, they are given by 0, 0, 1, where the z axis is perpendicular to the disk lying in the xy-plane. For a long cylindrical wire with its axis lying along z direction, the values are ½, ½, 0. For a prolate spheroid with its long axis lying along z direction, $N_{xx}= N_{yy}$ with $N_{zz} < N_{xx}$. The total magnetostatic energy

density of these shapes can be described as

$$E = \frac{\mu_0}{2}\left[N_{xx}M_x^2 + N_{yy}M_y^2 + N_{zz}M_Z^2\right] = \frac{\mu_0 M_s^2}{2}\left[N_{zz} + \left(N_{xx} - N_{zz}\right)\sin^2\theta\right]$$

where θ is the angle between z axis and the magnetization. For a thin disk or film, the energy will be at the minimum when the magnetization is lying in the plane (the preferred direction of magnetization). For a long cylindrical wire or prolate spheroid, the energy will be at the minimum when the magnetization is lying along the z axis (the preferred direction of magnetization).

3.2.3 Magnetoelastic anisotropy

Magnetoelastic anisotropy arises from deformation induced in lattice when stress is applied to the lattice. The spin moments are coupled to the lattice via the orbital motions of electrons. Consequently, the change in distance between the atoms will alter the lattice interaction energies between the atoms and hence cause anisotropy. Assuming that a stress of σ (N/m^2) is applied to a ferromagnetic body in the direction ($\gamma_1, \gamma_2, \gamma_3$), we can write the magnetoelastic energy density as [4]

$$E = -\frac{3}{2}\lambda\sigma\cos^2\theta$$

where λ is the magnetostriction constant and θ is the angle between magnetization and tensile stress direction.

3.2.4 Uniaxial anisotropy

For ferromagnetic material having uniaxial anisotropy, the energy density can be expressed as $E = K_1\sin^2\theta$, where θ is the angle of magnetization that makes with the

easy axis of magnetization and K_1 is of positive value. The hard axis of magnetization will be along $\theta = 90^o$, where the energy is of the maximum value.

3.2.5 Interface and volume anisotropy

Both bulk and interface contribute to the anisotropy of thin films. The effective anisotropy can be described as [5,6]

$$K_{eff} = K_v + \frac{2K_s}{t}$$

where K_s is anisotropy from the interface per unit area, K_v is the anisotropy due to the bulk per unit volume and t is the thickness of the ferromagnetic layer. The volume anisotropy K_v consists mainly of demagnetization energy or shape anisotropy, magnetocrystalline anisotropy and magnetoelastic energy. In the bulk system, the anisotropy is mainly dominated by volume term. However, in the case of thin film whose thickness approaches $\frac{2K_S}{K_v}$, the interface term can become more significant. In most cases of thin films, shape anisotropy is still dominant and in-plane magnetization is preferred.

3.2.6 Exchange interaction anisotropy

Exchange interaction is responsible for the alignment of spins in a ferromagnetic material. This exchange force between the spins is of quantum mechanical nature. The energy between the two spins S_i and S_j on site i and j is written as [7]:

$$E = -\sum_{i \neq j} J_{ij} \vec{S}_i . \vec{S}_j$$

where J is the exchange integral and it is positive for parallel alignment of $\vec{S}_i$ and $\vec{S}_j$.

3.2.7 Exchange anisotropy

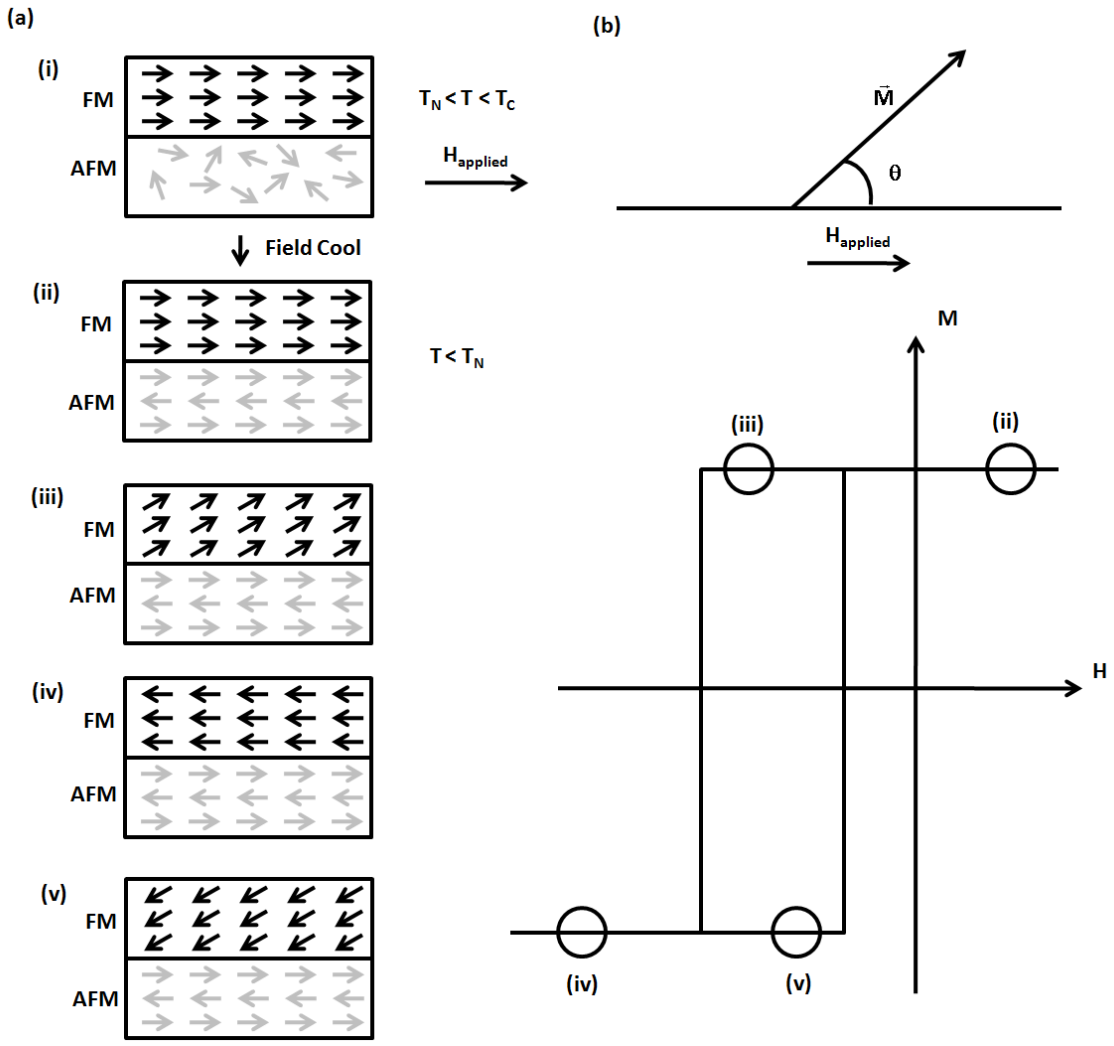

Fig. 3.2 Schematic diagram of (a) the spin configuration of an FM-AFM bilayer at different stages (i)-(v) of (b) an exchange biased hysteresis loop.

Exchange anisotropy can be qualitatively explained by assuming ferromagnetic exchange interaction between the ferromagnetic (FM) and antiferromagnetic (AFM) spins at an AFM-FM interface [8,9]. When the field is applied in the temperature range of, $T_N < T < T_C$, the FM spins will align in the same direction as the applied field direction while AFM spins remain random. Due to the ferromagnetic exchange interaction, the

AFM spins next to FM will align in the same direction as the FM spin when the T cools below T_N in the presence of field. Accordingly, the rest of the AFM spins will arrange in AFM order. When field is reversed, the FM spins start to rotate but the AFM spins remain unchanged due to the sufficiently huge AFM anisotropy. The AFM spins at the interface exert a microscopic torque on the FM spins to keep them in their original position. Thus, the FM spins have one stable configuration in the direction of field applied in temperature range of, $T_N < T < T_C$. As a consequence, the field needed to reverse completely an FM layer will be larger if it is in contact with an AFM because an extra field is needed to overcome the microscopic torque. The FM spins will start to rotate at smaller field once the field is rotated back to its original position due to its interaction with the AFM spins which exert now a torque in the same direction as the field. As a result, the hysteresis loop will shift to the left in the field axis.

Energy density due to the exchange anisotropy can be written as follows

$$E = -K_u \cos\theta$$

where K_u is unidirectional anisotropy energy density constant and θ is angle between the direction of applied field to align the FM spins in the temperature range of $T_N < T < T_C$ and the direction of magnetization [9].

3.2.8 Anisotropic magnetoresistance

The effect of resistivity dependent on the orientation of magnetization with respect to the direction of current is known as anisotropic magnetoresistance. In most 3d-transition metal alloys, the resistivity of a sample with magnetization parallel to the current direction (ρ_{ll}) is larger than resistivity of sample with magnetization perpendicular to the

current direction ($\rho_{\perp}$) [10]. The resistivity can be written as [10]

$$\rho(\theta) = \rho_{\perp} + (\rho_{ll} - \rho_{\perp})\cos^2(\theta)$$

where θ is the angle between the magnetization direction and the current direction.

3.2.9 Ferromagnetic resonance frequency

Under the application of static magnetic field, the magnetization of the specimen will precess about the direction of the static field. Ferromagnetic resonance occurs when transverse RF field in addition to the static field is applied, energy is absorbed strongly from the RF transverse field and the transverse susceptibility (both the real and imaginary components) are very large [11]. The driving frequency of RF transverse field which results in ferromagnetic resonance is known as ferromagnetic resonance frequency and it is equal to the precessional frequency of the magnetization in static field.

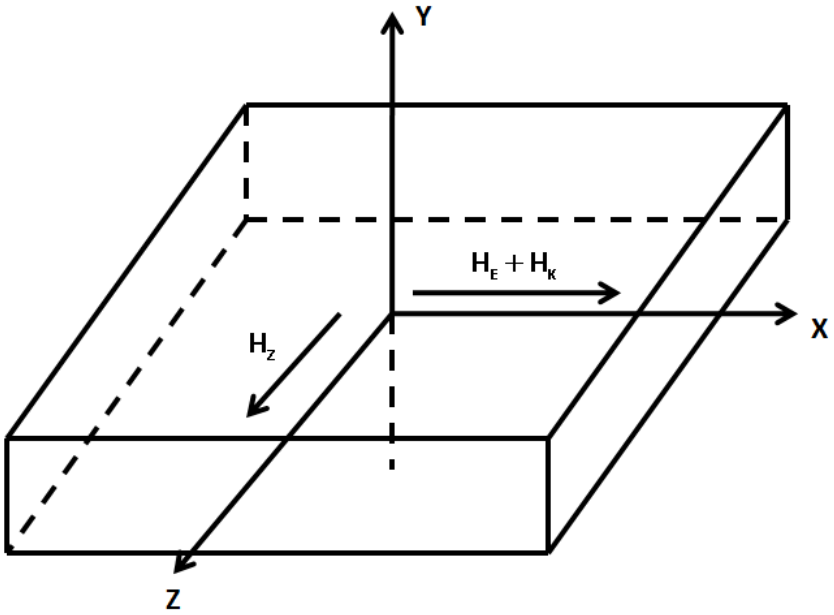

Fig. 3.3 Schematic diagram of the applied RF field (H_Z), unidirectional anisotropy (H_E) and uniaxial anisotropy (H_K) acting on the film.

Assuming the case of a magnetic thin film is of x-z plane, let both the unidirectional anisotropy, H_E, and uniaxial anisotropy, H_K, lie along x axis of the film while RF tranverse field of $H_z = H_{app} e^{i\omega t}$ is applied parallel to the z axis. Then the effective field can be written as $\vec{H} = \begin{bmatrix} H_x - N_x M_x \\ -N_y M_y \\ H_z - N_z M_z \end{bmatrix}$, where $N_x = N_z = 0$, $N_y = 4\pi$ and $H_x = H_k + H_E$ (in CGS unit). The Landau-Lifchitz-Gilbert (LLG) equation, which describes the precession of magnetization in the effective field without the damping factor can be written as

$$\frac{d\vec{M}}{dt} = \gamma \vec{M} \times \vec{H}$$

where γ is the gyromagnetic ratio. The equation of motion for all components of $\vec{M}$ can be expressed as follows

$$\frac{dM_x}{dt} = \gamma [H_z + 4\pi M_z] M_y \approx 0$$

$$\frac{dM_y}{dt} = \gamma [M_z H_x - M_x H_z]$$

$$\frac{dM_z}{dt} = \gamma [-4\pi M_x - H_x] M_y$$

On solving these equations with the time dependence $e^{i\omega t}$, the susceptibility $\chi_Z = \frac{M_Z}{H_z}$ is found to be

$$\chi_z = \frac{\chi_0}{1 - \frac{\omega^2}{\omega_0^2}}$$

where

$$\chi_0 = \frac{M_x}{H_x}$$

and the resonance frequency of this magnetic thin film is given by:

$$\omega_0 = \gamma\left[4\pi M_x + H_k + H_E\right]^{1/2}\left[H_k + H_E\right]^{1/2} \qquad \text{(C.G.S)'}$$

$$\omega_0 = \gamma\mu_0\left[M_x + H_k + H_E\right]^{1/2}\left[H_k + H_E\right]^{1/2} \qquad \text{(S.I)}$$

3.3 References

[1] M. I. Darby AND E. D. Isaac, IEEE Trans. Mag. **MAG-10**, 259 (1974).

[2] W. Döring, *Ann. Physik* **1**, 102 (1958).

[3] J. A. Osborn, *Phys. Rev.* **67**, 351 (1945).

[4] Soshin Chikazumi, *Physics of Magnetism*, (John Wiley & Sons, Inc., New York) pp.182-184 (1964).

[5] H. J. G. Draaisma, W. J. M. de Jonge and F. J. A. den Broeder, *J. Magn. Magn. Mater.* **66**, 351 (1987).

[6] B. N. Engel, C. D. England, R. A. Van Leeuwen, M. H. Wiedmann, and C. M. Falco, *Phys. Rev. Lett.* **67**, 1910 (1991).

[7] A. Aharoni, *Introduction to the Theory of Ferromagnetism* (Oxford Science Publications, Oxford University Press, Oxford) pp. 16-17 (1996).

[8] W.H. Meiklejohn and C.P. Bean, *Phys. Rev.* **102**, 1413 (1956).

[9] W.H. Meiklejohn, and C.P. Bean, *Phys. Rev.* **105**, 904 (1957).

[10] T. R. McGuire and R. I. Potter, IEEE Trans. Mag. **MAG-11**, 1018 (1975).

[11] Charles Kittel, *Introduction to Solid State Physics, Seventh edition* (John Wiley & Sons, Inc., New York) pp. 503-506 (1996).

Chapter 4 Length dependence of coercivity of $CoFe_2$ nanowire arrays with high aspect ratios

4.1 Introduction

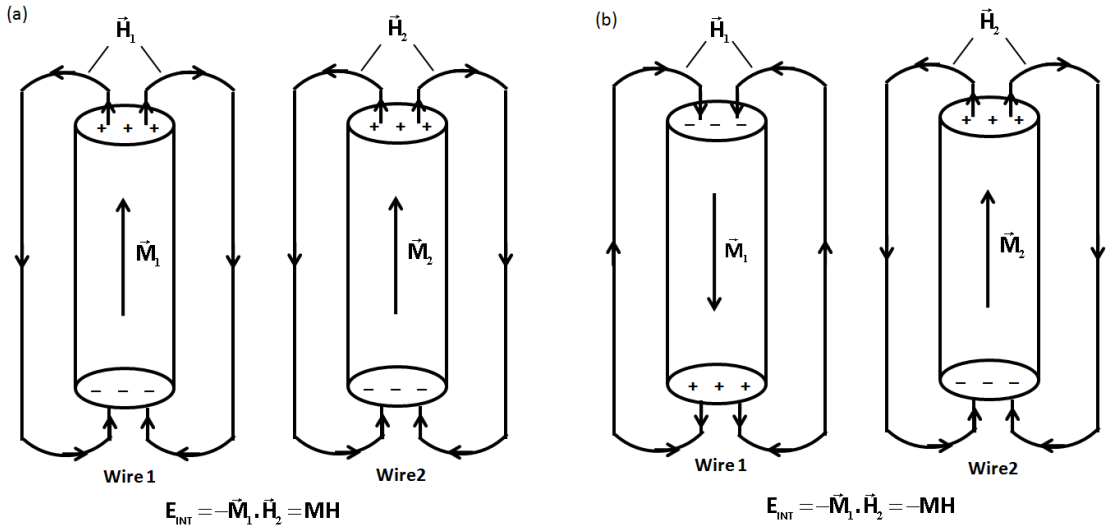

Fig. 4.1 Schematic diagram of magnetostatic interaction energy of the wire 1 resulted from the coupling of magnetization in wire 1 (M_1) with stray field (H_2) from wire 2 (a) before the reversal of magnetization in wire 1 and (b) after the reversal of magnetization in wire 1.

Studies on general magnetic behaviors have been reported on nanowire arrays of Fe, Ni, Co and their alloys [1-3]. Magnetic properties of nanowires are governed by two factors, the magnetic nature of the individual nanowire and the magnetostatic interactions between the nanowires. Magnetic nature of an individual nanowire is influenced by longitudinal uniaxial shape, magnetocrystalline and magnetoelastic anisotropies. Magnetostatic interaction originates from unbalanced magnetic poles at both ends of individual wires generating stray fields that couple with the magnetization of neighboring nanowires as illustrated in Fig. 4.1. Magnetostatic interactions can reduce the switching field of the nanowires as compared to the non-interacting array of nanowires. With

magnetostatic interactions considered, previous works have well interpreted the decreases in coercivity and remanence of nickel nanowire arrays with the increase in diameter of the nanowires while their interpore distance is kept constant [4,5].

In this Chapter, we investigated length dependence of coercivity of $CoFe_2$ nanowire arrays which have high aspect ratios ranging from 200 to 1000. Few experimental works have been carried on this issue in detail and in such a large range of aspect ratio [6.7]. The coercivity of the nanowires in this work cannot be explained based on the assumption of non-interacting nanowires. The magnetostatic interaction between the nanowires should be included to account for the length dependence of magnetic properties of the nanowire arrays. A simple model based on the influence of effective magnetostatic energy was used to calculate the coercivity of the nanowires. The calculation results with this model showed a good agreement with experimental data.

4.2 Experiment

4.2.1 Fabrication of AAO templates

The anodic aluminum oxide (AAO) templates were prepared from aluminum foil by a one-step anodization technique. The aluminum foils were cleaned by ultrasonic in acetone and distilled water before they were annealed in furnace for 6 h at 500 $^{\circ}$C. Then, the annealed aluminum foils were electropolished at 20 V for 2 min in a solution consisting of ethanol and perchloric acid at a ratio of 5:1. The electropolishing was carried out at 5 $^{\circ}$C. After this treatment, the aluminum foils were anodized at 25 V in 0.4 M H_2SO_4 at 10 $^{\circ}$C to form AAO templates. Lengths of the AAO templates were varied from 7 μm to 35 μm by using different anodizing times. The pore diameter and the distance between two nearest pores of the AAO templates were kept constant.

4.2.2 AC electrodeposition of nanowires

The AAO templates were immersed in 0.3 M H_3PO_4 for 15 min at 40 °C to widen the pore and to thin down the barrier layer so that they were suitable for AC electrodeposition. $CoFe_2$ nanowires were deposited into the AAO templates by using an AC electrodeposition. The electrolyte used in the AC electrodeposition consisted of 0.073 M $CoSO_4$, 0.0147 M $FeSO_4$, 0.6 M boric acid and 1 g/L of ascorbic acid. Deposition was carried out at room temperature at an AC voltage of 16 V and 100 Hz, using a graphite rod as counter electrode. Current of the deposition was monitored during the deposition. Initially, the current fell sharply and then remained stable. The deposition was stopped when there was an increase in the current, indicating that some of the nanowires were growing out of the AAO templates.

4.2.3 Characterization

Microstructures of the AAO templates and the nanowires were observed by using a scanning electron microscopy (SEM) and transmission electron microscopy (TEM), respectively. In order to measure the length of the $CoFe_2$ nanowires deposited in the AAO templates, the AAO templates were first etched in a solution of 6 wt% H_3PO_4 and 1.8 wt% CrO_3 at 40 °C until tips of the nanowires were exposed. Then the AAO templates filled with the $CoFe_2$ nanowires were cut with a pair of scissor for SEM side view. To liberate the nanowires from the templates for TEM studies, the AAO templates were dissolved in 1 M NaOH. After this, the solutions were washed carefully with distilled water for several times, and then a drop of suspension was dropped on a copper grid coated with carbon film for TEM observation. Phase composition of the nanowires was investigated by using X-ray diffraction (XRD) with Cu Kα radiation and selected area

electron diffraction (SAED). Prior to XRD measurement, aluminum was removed from the AAO templates embedded with $CoFe_2$ nanowires using $CuCl_2$ solution. Magnetic properties of the nanowires were measured by using a vibrating sample magnetometer (VSM) with the applied field parallel to the long axis of wires.

4.3 Results and discussion

Fig. 4.2 displays a typical XRD pattern of the electrodeposited $CoFe_2$ nanowires embedded in the AAO template. $CoFe_2$ nanowires exhibit body-centered cubic structure with a preferred texture orientation of [1 1 0] along the long axis of nanowires.

SEM image of the AAO template is shown in Fig. 4.3(a). The template has an average pore diameter pore of 32 nm and interpore distance (D) of 65 nm. SEM top view of a 21 μm long AAO template deposited with $CoFe_2$ nanowires which has been etched in a solution of 6 wt% H_3PO_4 and 1.8 wt% CrO_3 at 40 ˚C is presented in Fig. 4.3(b). Clearly, tips of the nanowires are exposed after the etching of the AAO template.

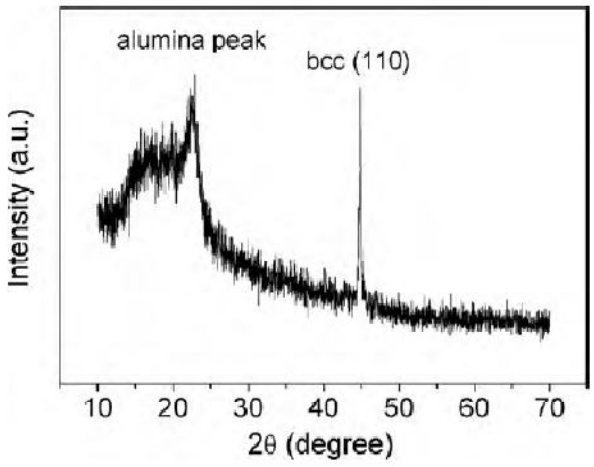

Fig. 4.2 XRD pattern of the $CoFe_2$ nanowires embedded in the AAO template with aluminum being removed.

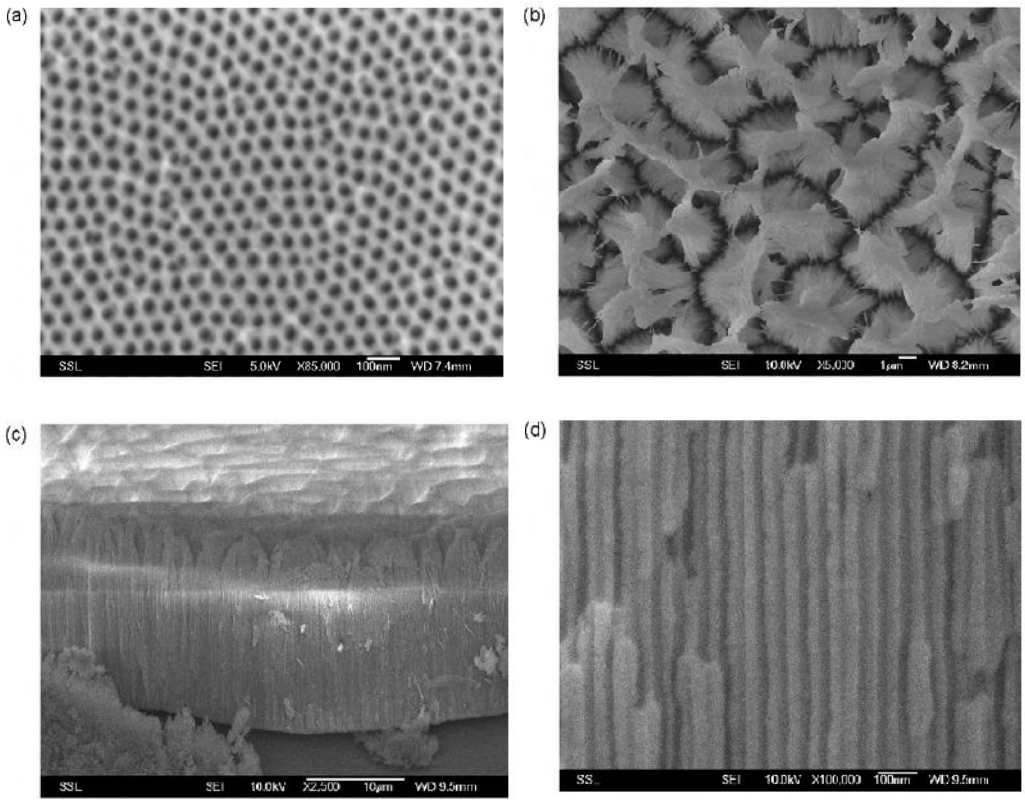

Fig. 4.3 (a) SEM image of top view of the AAO template fabricated. (b) SEM top view of 21 μm long AAO template deposited with $CoFe_2$ nanowires which has been etched in a solution of 6 wt% H_3PO_4 and 1.8 wt% CrO_3 at 40 ˚C. (c) The corresponding SEM side view of the same AAO template filled with $CoFe_2$ nanowires. (d) Enlarged SEM view of (c).

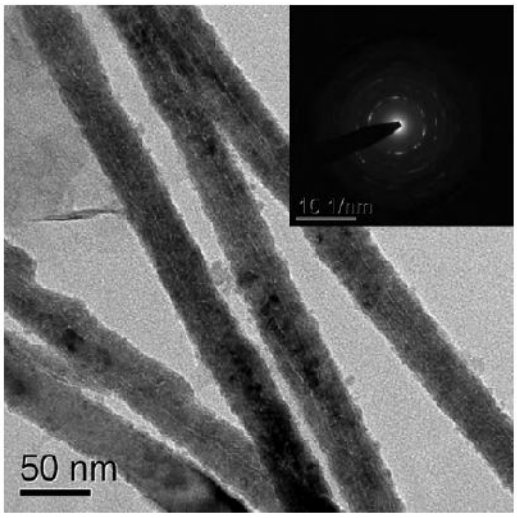

Fig. 4.4 TEM image of the $CoFe_2$ nanowires freed from the AAO template with the inset showing SAED of the $CoFe_2$ nanowires.

Corresponding SEM side view of the same AAO template filled with $CoFe_2$ nanowires is shown in Fig. 4.3(c). Length of the nanowires is about 20.5 μm which is close to the length of the AAO template. Fig. 4.3(d) shows an enlarged view of Fig. 4.3(c). Fig. 4.4 shows TEM image of the $CoFe_2$ nanowires freed from the AAO template. Diameter of the $CoFe_2$ nanowires (2R) is also 32 nm which is consistent with the average pore diameter of the AAO template. Polycrystalline structure of the $CoFe_2$ nanowires is confirmed by the multiple diffraction rings in the SAED pattern.

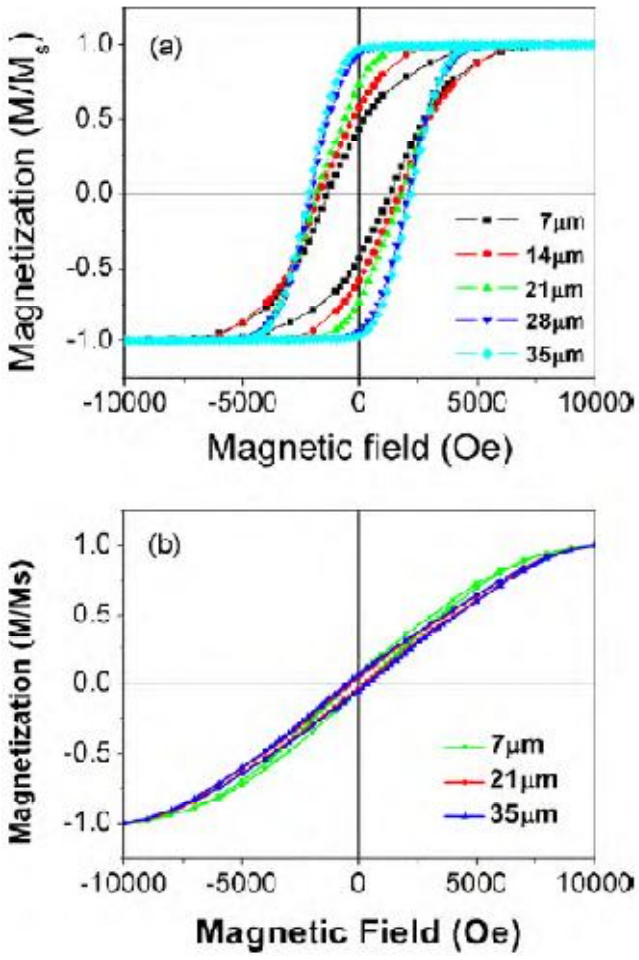

Fig. 4.5 (a) Hysteresis loops of the $CoFe_2$ nanowires with length L varying from 7μm to 35μm. The external field is applied parallel to the long axis of the nanowires. (b) Hysteresis loops of the $CoFe_2$ nanowires with the external field applied perpendicular to the long axis of the nanowires.

Fig. 4.5(a) presents magnetic hysteresis loops of the nanowire arrays with average nanowire lengths (L) varying from 7 μm to 35 μm with the field applied parallel to the long axis of nanowires. Fig. 4.5(b) shows magnetic hysteresis loops of the nanowire arrays with the field applied perpendicular to the long axis of nanowires. Clearly, the coercivity increased with length of the nanowires. The magnetic properties of an isolated nanowire have been also studied with the micromagnetism simulation based on the Landau–Lifshitz–Gilbert equation. LLG Micromagnetics SimulatorTM was used to simulate the hysteresis loop of an isolated $CoFe_2$ nanowire with applied field parallel to the long axis of nanowire. The cell size was chosen to be 8nm×8nm×8 nm and the

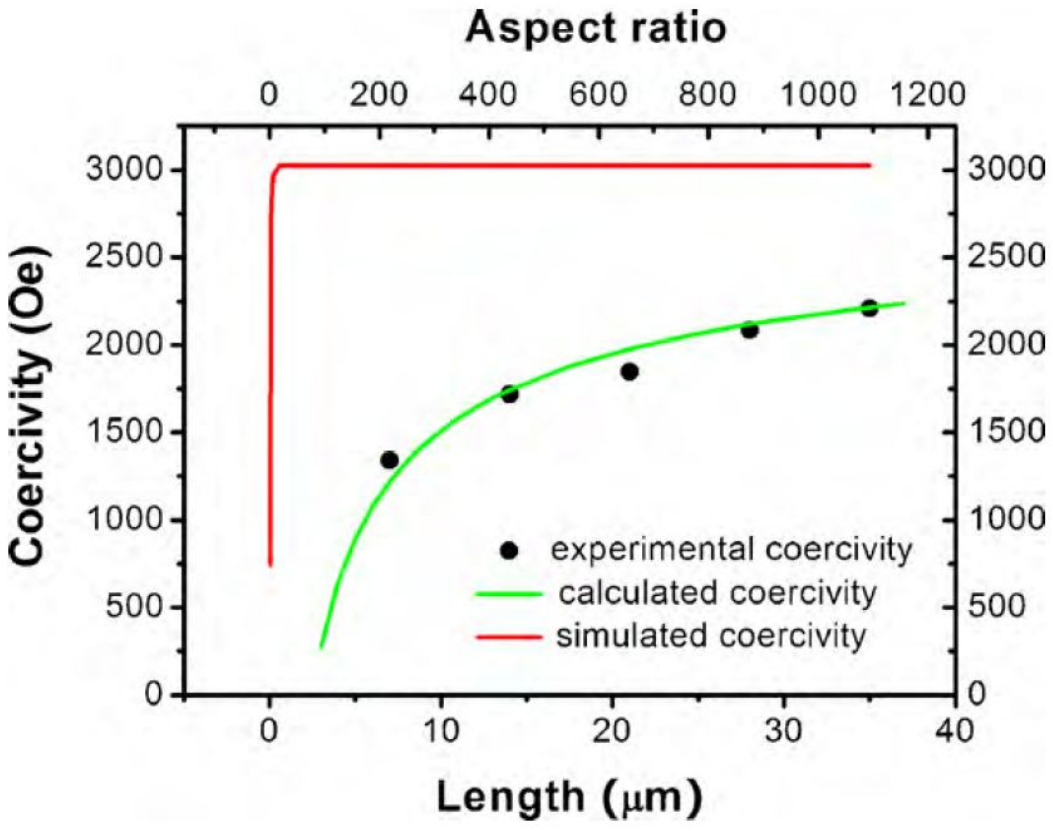

Fig. 4.6 Coercivity of the nanowires as a function of length. The red line represents the LLG simulation result of coercivity of an isolated nanowire. The green line represents the coercivity in an array of $CoFe_2$ nanowires calculated using Eq. (4.1). The black dots are experimental results of coercivity measured by VSM.

damping factor was 0.3. The saturation magnetization of the $CoFe_2$ nanowires (Ms) is 1930 emu/cm^3 and the exchange constant is 2.5×10^{-11} J/m. Since the $CoFe_2$ nanowire has a polycrystalline structure, the crystalline anisotropy energy was chosen to be zero. The coercivity of a long wire with large radius can also be predicted from curling mode [8], $H_0 = cA/\mu_0 M_s R^2$ and is calculated to be 3430 Oe. However, the coercivity of a long wire from the simulation is 3025 Oe which is much lower than that predicted by the curling mode. Fig. 4.6 presents the experimental and simulation results of length dependence of coercivity. Clearly, the shape anisotropy of an isolated nanowire cannot account for the trend of increasing coercivity with the length at such high aspect ratios ranging from 200 to 1000.

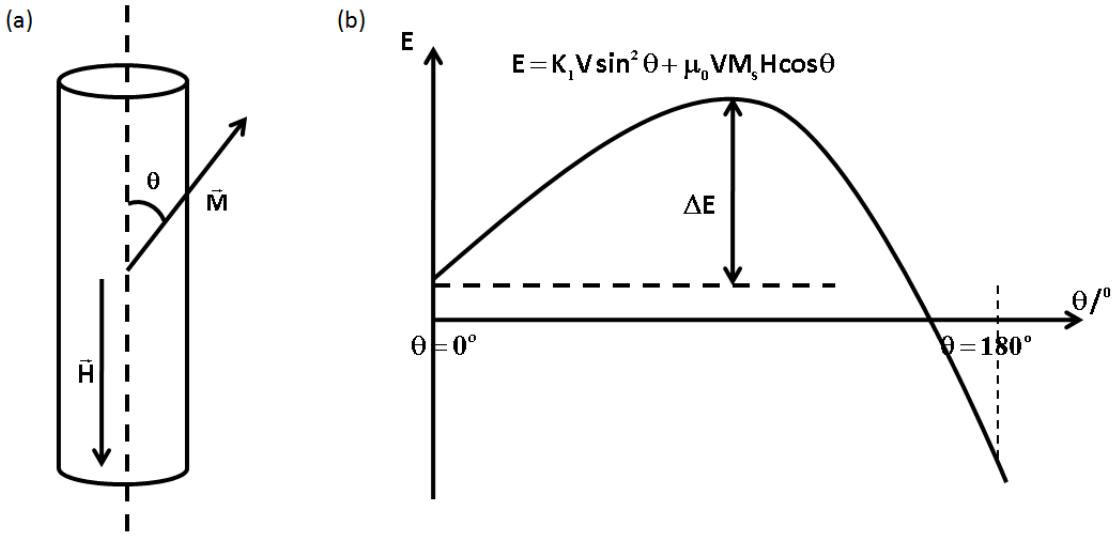

Fig. 4.7 Schematic diagram of: (a) magnetization and applied external field acting in the wire, and (b) energy of the wire as a function of θ, assuming uniaxial anisotropy of wire.

In order to interpret this observation, magnetostatic interaction between the nanowires must be taken into consideration when the distance between two nearest nanowires is

comparable to the diameter of a nanowire. Stray field generated from each nanowire in the array will couple with the magnetizations of other nanowires. This magnetostatic interaction favors an anti-parallel distribution of magnetization in neighboring nanowires [4, 9]. In an array with all the nanowires initially magnetized in the same direction, the magnetostatic interaction between neighboring nanowires favors the reversal of some of them. Assuming the reversal of an individual nanowire produces a decrease of magnetostatic interaction $\varepsilon E_{int}(D)$ that equals to the magnetic anisotropy barrier ΔE of a nanowire, the macroscopic coercivity will be:

$$H_c = H_0\left(1-\sqrt{\frac{\varepsilon E_{\text{int}}(D)}{K_1 V}}\right) \qquad (4.1)$$

where V represents the volume of a single nanowire and H_0 is the coercivity of an isolated nanowire, $E_{int}(D)$ represents the magnetostatic interaction between two nanowires separated by distance D. Such interaction has been derived by assuming the homogenous magnetization in the direction along long axis of the wire and has an expression, $E_{\text{int}} = \left(\frac{\mu_0 M_s^2 R^2}{2DL}\right)\left[1-1/\sqrt{1+L^2/D^2}\right]V$, if R/L<<1 [10]. Assuming that each magnetic nanowire is single domain and has the uniaxial shape anisotropy, magnetic anisotropy barrier will be given as $\Delta E = K_1 V(1-H/H_0)^2$, with the uniaxial shape anisotropy $K_1 = \mu_0 M_s H_0/2$ [11]. Finally, the macroscopic coercivity as a function of L can be expressed as $H_c = H_0\left[1-\sqrt{\left(\frac{\varepsilon M_s R^2}{H_0 DL}\right)\left(1-\left(1+L^2/D^2\right)^{-1/2}\right)}\right]$. Moreover, ε is a fitting parameter that depends on the distribution of the magnetic wires in space and on the long distance correlation among the wires. In Eq. (4.1), both H_0 = 3025 Oe which is

obtained from the LLG simulation and ε = 80 are used. Since the magnetostatic energy $E_{int}(D)$ decreases with length of the nanowires, the coercivity in the array of the $CoFe_2$ nanowires increases with the length of the nanowires. The calculated coercivity is presented in Fig. 4.6. It can well predict the trend observed from the experimental data and shows relatively good agreement with experimental data. At lower shape ratio range, Vázquez et al. observed that there was almost a linear relationship between the coercivity and length [6]. On the contrary, in dot arrays where 2R > L, a different behavior was observed in which coercivity decreased with increasing length [12].

Not only the coercivity of the nanowires increases with the length of the nanowires, remanence (Mr/Ms) also increases with the length of the nanowires, as shown in Fig. 4.5. This can be explained by the length dependence of magnetostatic interaction between the nanowires. As the length of the nanowires interaction increases, the magnetostatic interaction decreases. Thus, the anti-parallel configuration between the magnetization states of the nanowires becomes less favorable and fewer nanowires have their magnetization flipped in the opposite direction in zero applied field.

4.4 Conclusions

In conclusion, we have fabricated $CoFe_2$ nanowires with high aspect ratios to investigate the effect of length on coercivity and remanence. Both coercivity and remanence increased with length of the nanowires. In order to account for such a phenomenon, the effect of magnetostatic interaction between the nanowires due to the coupling of stray field with magnetization of the nanowires must be included. This magnetostatic interaction reduced the coercivity and remanence in the array of nanowires. For longer nanowires, the strength of magnetostatic interaction became weaker and thus

coercivity and remanence increased. A simple expression as a function of magnetostatic interaction was used to obtain the coercivity in an array of the $CoFe_2$ nanowires and showed relatively good agreement with the experimental results.

4.5 References

[1] D.J. Sellmyer, M. Zheng and R. Skomski, *J. Phys.: Condens. Matter* **13**, R433 (2001).

[2] P.M. Paulus, F. Luis, M. Kröll, G. Schmid and L.J. de Jongh, *J. Magn. Magn. Mater.* **224**, 180 (2001).

[3] K. Nielsch, R.B. Wehrspohn, J. Barthel, J. Kirschner, S.F. Fischer, H. Kronmüller, T. Schweinböck, D. Weiss andU. Gösele, *J. Magn. Magn. Mater.* **249**, 234 (2002).

[4] M. Vázquez, K. Pirota, M. Hernández-Vélez, V.M. Prida, D. Navas, R. Sanz, F. Batallán and J. Velázquez, *J. Appl. Phys.* **95**, 6642 (2004).

[5] K. Nielsch, R.B. Wehrspohn, J. Barthel, J. Kirschner, U. Gösele, S.F. Fischer and H. Kronmüller, *Appl. Phys. Lett.* **79**, 1360 (2001).

[6] M. Vázquez, K. Pirota, J. Torrejón, D. Navas and M. Hernández-Vélez, *J. Magn. Magn. Mater.* **294**, 174 (2005).

[7] J. Escrig, R. Lavín, J.L. Palma, J.C. Denardin, D. Altbir, A. Cortés and H. Gómez, *Nanotechnology* **19**, 075713 (2008).

[8] R. Skomski, J.P. Liu and D.J. Sellmyer, *Phys. Rev. B* **60**, 7359 (1999).

[9] M. Bahiana, F.S. Amaral, S. Allende and D. Altbir, *Phys. Rev. B* **74**, 74412 (2006).

[10] D. Laroze, J. Escrig, P. Landeros, D. Altbir, M. Vázquez and P. Vargas, *Nanotechnology* **18**, 415708 (2007).

[11] M.P. Sharrock, *J. Appl. Phys.* **76**, 6413 (1994).

[12] M. Grimsditch, Y. Jaccard and I.K. Schuller, *Phys. Rev. B* **58**, 11539 (1998).

Chapter 5 Magnetic and transport properties in pore-modified CoAlO antidot arrays

5.1 Introduction

Self-ordered porous anodic aluminum oxide (AAO) membranes [1, 2-6] have been utilized to make large-scale antidot arrays, which can reduce the lattice dimensions to tens of nanometres. Magnetic properties and magnetoresistance scaling with film thickness were discussed in these antidot arrays. But, to date, no comprehensive work on this issue has been reported, particularly with respect to physical properties of antidot arrays with modified geometries.

In this work, large-scale magnetic antidot arrays were fabricated on porous AAO membranes. Porosity features of the AAO membranes were modified to give magnetic antidot arrays with variable constrained geometries. Evolution of magnetic and transport properties of the antidot arrays was investigated as a result of their structural variations. A vanishing of magnetic anisotropy and a sign change in the magnetoresistance with reduction in the antidot sizes were observed. The growth process of the antidot arrays with varied magnetic properties was discussed.

5.2 Experiment

5.2.1 Fabrication of AAO membrane

AAO membranes were fabricated by a standard two-step anodic anodizing process using a high purity (>99.99%) aluminum sheet [7]. Nanochannels in the as-made AAO membranes were only open at one end while the other end was closed by thin hemispherical alumina barrier layers, as schematically shown in Fig. 5.1(*a*). These barrier

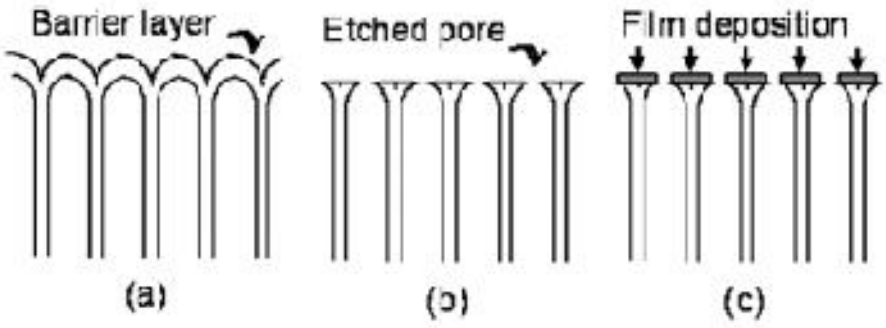

Fig. 5.1 Schematic illustrations of the CoAlO antidot preparation route: (*a*) the as-made AAO membranes with closed barrier layers; (*b*) chemically etched AAO membranes with partially opened barrier layers; (*c*) film deposition on AAO membranes made after the etching process.

layers could be gradually dissolved in acid solutions (e.g. phosphoric acid) at room temperature. AAO membranes with different porosity features were obtained by manipulating the etching process, as schematically shown in Fig. 5.1(*b*).

5.2.2 RF sputtering of CoAlO antidot arrays

CoAlO antidot arrays were deposited on the substrates by RF magnetron sputtering from a composite target (cobalt plate+Al_2O_3 chips) at an Ar pressure of 3.0 mTorr, as illustrated in Fig. 5.1(*c*). An external magnetic field of about 200 Oe was applied *in situ* on the film plane to induce an effective anisotropy.

5.2.3 Characterization

Cobalt content in the arrays was about (85 ± 5) vol.% estimated by calculating the saturation magnetizations (M_s) of the films by assuming that the crystallized cobalt grains had an equal M_s with its bulk value (1400 emu cm^{-3}). The composite microstructures comprising of crystallized cobalt grains and amorphous boundaries were revealed by the

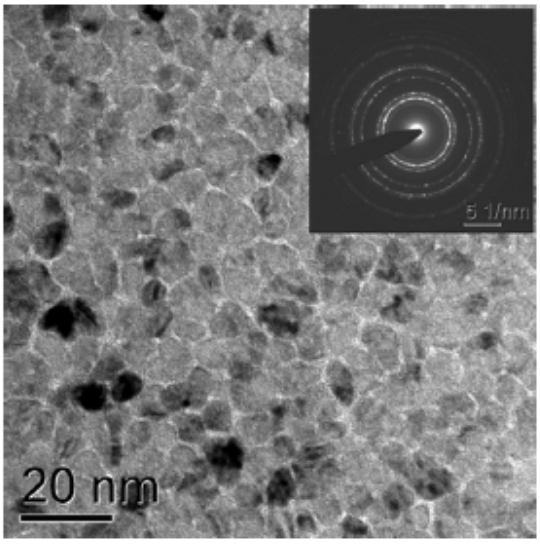

Fig. 5.2 Typical high resolution TEM image of a 40 nm thick CoAlO composite film deposited on the continuous barrier layers (shown in Fig. 5.1(*a*)). The averaged grain size was around 8 nm. The inset shows typical electron diffraction patterns for a polycrystalline fcc cobalt.

transmission electronic microscope (TEM) measurement, applied on a continuous CoAlO film deposited on the AAO barrier layers, as shown in Fig. 5.2. The cobalt grains with fcc phase were confirmed by the selected area electron diffraction (SAED) given in the inset of Fig. 5.2. Magnetic properties of the samples were measured by a vibration sample magnetometer with a maximum field of 10^4 Oe and magnetoresistance was measured in the film plane by a normal four-point probing technique.

5.3 Results and discussion

5.3.1 Influence of pore sizes in the 40 nm thick CoAlO antidot arrays

We aimed to study the dependence of magnetic properties of the CoAlO films on pore sizes. Fig. 5.3 shows SEM images of the 40 nm thick CoAlO antidot arrays with different pore sizes, denoted by an average diameter, $\langle D_p \rangle$. Without chemical etching,

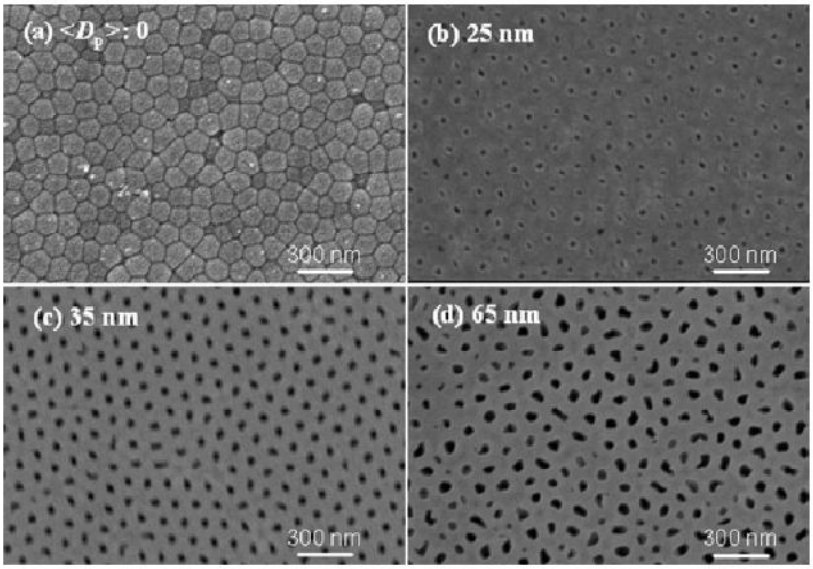

Fig. 5.3 SEM images of the 40 nm thick CoAlO antidot arrays with average pore diameter, $\langle D_p \rangle$ = *(a)* 0 nm, (*b*) 25 nm, (*c*) 35 nm and (*d*) 65 nm.

hexagonally aligned block arrays were formed in the films deposited directly on the AAO barrier layers, as shown in Fig. 5.3(*a*). Three antidot arrays with gradually increasing pore sizes are shown in Fig. 5.3(*b*)–(*d*), which had a constant pore density of ~10^{10} cm^{-2}. These antidot arrays showed micrometre-scale ordering till the average pore size was increased up to 35 nm. Above this value, the dispersions of pore sizes and shapes increased greatly. Surface roughness of the antidot arrays (in the non-pore areas), measured by using an atomic force microscope, was in the range of a few nanometres and much smaller than the film thickness (40 nm). Thus, in this case roughness factor could be excluded when considering magnetic properties of the pore-modified CoAlO antidot arrays.

Fig. 5.4 shows the minor magnetic hysteresis loops of the 40 nm thick CoAlO antidot arrays of different average pore diameters, $\langle D_p \rangle$. The solid and dashed curves, respectively, represent the loops measured with the fields parallel and transverse to

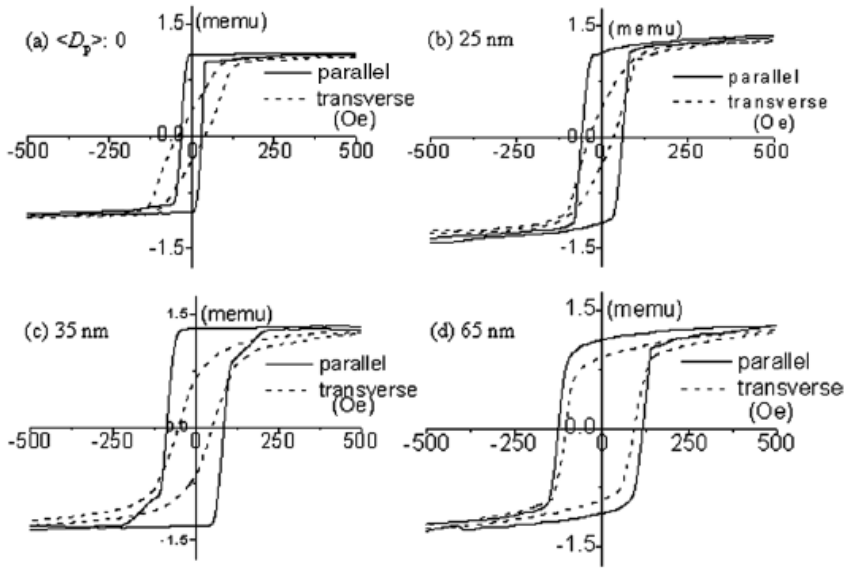

Fig. 5.4 Minor magnetic hysteresis loops of the 40 nm thick CoAlO antidot arrays with average pore diameter, $\langle D_p \rangle$ = *(a)* 0 nm, (*b*) 25 nm, (*c*) 35 nm and (*d*) 65 nm. The solid and dash line, respectively, represent the measurement directions parallel or transverse to the external field direction applied during film growth.

the induced easy axis which was along the external field applied during film deposition. By comparing the shapes of the two loops in Fig. 5.4(*a*), it is clear that the structurally continuous films are of prominent magnetic anisotropy. This feature was basically reserved for the antidot arrays of $\langle D_p \rangle$ = 25 nm (Fig. 5.4(*b*) and 35 nm (Fig. 5.4(*c*)). It means that 200 Oe was effective to induce an effective uniaxial anisotropy to align the magnetic domains along a preferential direction. Angular dispersion of the easy axis was indeed increased after introducing nanopores into the continuous structures, as evidenced by the broadening of the transverse hysteresis loops. This tendency was accelerated when $\langle D_p \rangle$ > 35 nm. The antidot array became nearly magnetic isotropic when $\langle D_p \rangle$ = 65 nm, where the hysteresis loops in both directions showed similar broadness, as shown in Fig.

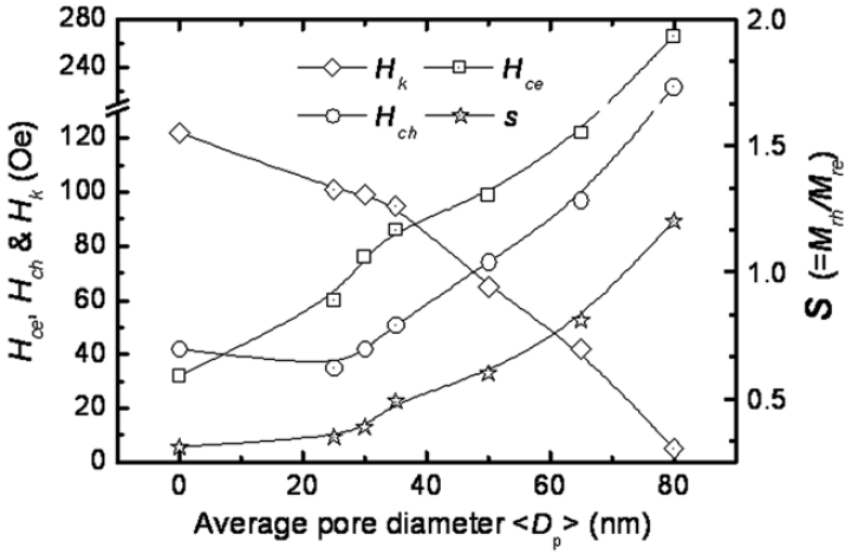

Fig. 5.5 Variations of magnetic parameters of the 40 nm thick CoAlO antidot arrays as a function of average pore diameter, $\langle D_p \rangle$. The maximum $\langle D_p \rangle$ value obtained was about 80 nm, beyond which coalition between neighboring pores occurred in large amount.

5.4(*d*). Fig. 5.5 gives the values of selected magnetic parameters of the antidot arrays as a function of $\langle D_p \rangle$, where H_{ce} and H_{ch} are the easy- and hard-axis coercivities, H_k is the effective anisotropy field and *s* is the ratio of the remanent magnetizations of hard and easy axes. To estimate H_k, middle slope straight lines (across origin) of low-field hysteresis loops were drawn to intersect the inverse extensions of the magnetization saturation lines, and the field difference at the intersecting points from the hard and easy axis loops were taken as the value of H_k. When $\langle D_p \rangle \leq$ 35nm, magnetic properties of the antidots showed moderate variations due to the introduction of the pore arrays. Domains in these samples still had preferential orientations. But when $\langle D_p \rangle$ > 35 nm, coercivities showed a quicker increase accompanying a rapider reduction in H_k, suggesting the hardening of magnetism in these arrays with further increasing $\langle D_p \rangle$. Thus, in this case,

35 nm seemed to be a critical pore size, beyond which the antidots quickly lost their magnetic anisotropy.

It is known that fcc cobalt-based composite films are soft magnetic in nature. Therefore, 200 Oe was strong enough to induce an obvious uniaxial anisotropy. With the introduction of pore arrays, the induced anisotropy was still the main force in determining the domain orientations and their reversals in the films with $\langle D_p \rangle \leq$ 35 nm. This suggested that the stray fields emanating from the pore edges with high-densities of ~10^{10} cm^{-2} had no serious effects on the neighbouring domain orientations. This was possible for the present nanogranular thin films (shown in Figure 5.2), where the strong intergranular exchange coupling could prevent the free reversal of domains by the disturbance of the stray fields. Under this circumstance, pore arrays of diameters below 35 nm, much smaller than the domain wall width of fcc cobalt phase (~90 nm at room temperature [8]), might be regarded as structural defects. The coercivities were increased due to their domain wall pinning effect. When pore diameters were further increased ($\langle D_p \rangle >$ 35 nm), obstruction of the wall motion by the pores would be greatly strengthened. As a result, the ever increasing stray fields resulting from the increased pore areas would gradually oblige the local domains to orient along the perimeters of the pores required by reduction in magnetostatic energy. In this case, shape anisotropy would be induced from the pore-modulated network topology and becomes dominant when the domain dimensions were closer to the wall width or even smaller, where nucleation or propagation of the walls would be eliminated. Consequently, the coercivities would be further greatly increased, as found in the antidots with $\langle D_p \rangle >$ 65 nm. In addition,

because of the angular dispersion in the trajectories of the arriving atoms associated with the sputtering process, the ferromagnetic materials would be extended into the channels of large pores and possibly formed portions of nanotube-like structures. In these structures, the magnetizations directed by either curling along the pore perimeters or parallel to the channel axes [9] would generally need high fields (larger than several kOe) to saturate their orientations in the film-plane geometry [10]. Their presence might have negligible contributions to the low-field hysteresis loops, as shown in Fig. 5.4 and Fig. 5.8, but could really influence the domain distributions in the neighbouring surface films through the long-range magnetostatic interactions [3, 6]. Therefore, the increased coercivities and weakened anisotropy in the larger pore modulated arrays should be attributed to the topology induced shape anisotropy superimposed by the stray fields from the pore channels.

Fig. 5.6 shows magnetoresistance ratio (MR) of the antidot arrays with $\langle D_p \rangle$ of (a) 25 nm and (b) 80 nm. The scanning magnetic fields were applied in-plane either parallel or transverse to the sensing current direction which was oriented along the induced hard axis, respectively, giving the longitudinal MR (LMR) and the transverse one (TMR), respectively. For the 25 nm diameter antidots, LMR was typically positive and TMR was negative. These features could be accounted for by the conventional anisotropic magnetoresistance (AMR), where a maximum (minimum) resistance could be induced due to the anisotropic spin–orbit coupling when the magnetic moments were parallel (perpendicular) to the current direction [11]. In the LMR measurement, the uniaxial anisotropy of the array would oblige the domains to gradually rotate from being parallel to the current direction at high fields to being perpendicular to it at low fields,

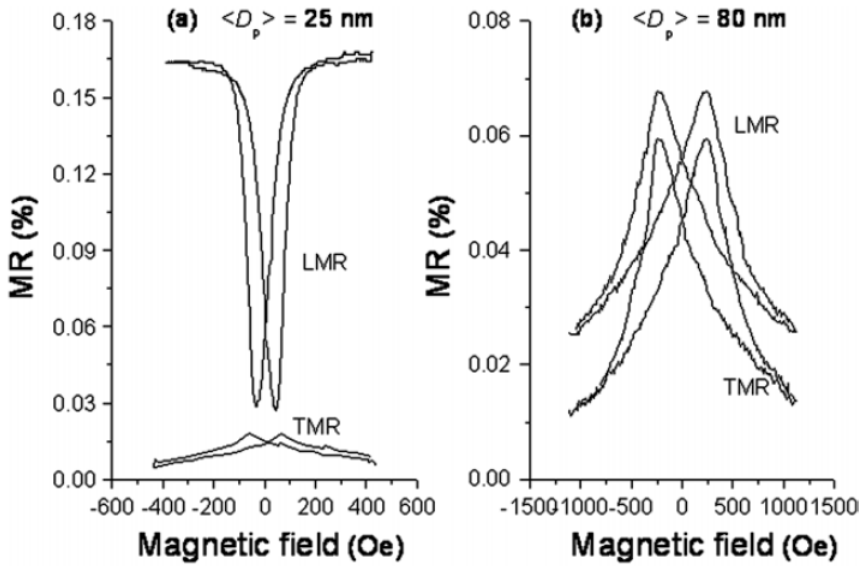

Fig. 5.6 MR curves of the antidot arrays with $\langle D_p \rangle$ of (a) 25 nm and (b) 80 nm. The sensing current was applied along the induced hard-axis direction. LMR and TMR were measured with the fields, respectively, longitudinal and transverse to the current direction. Here MR = (R(H)/R_T (5 kOe) -1) x 100%.

accompanying a monotonous decrease in MR on reducing the fields. A minimum LMR value was reached at fields of ~40 Oe close to the hard-axis coercivity (35 Oe) of the antidots. In the TMR measurement, the magnetization reversal along its easy axis would generally proceed by the motions of the 180^o domain walls, where the domains would be kept parallel to the applied fields. Thus, small negative MR values at lower fields would be expected. Here it should be noted that the maximum LMR value of ~0.17% obtained in this case was only one-third of that obtained in pure 20 nm fcc cobalt films ever reported [12]. The decreased magnetoelectric response of our CoAlO films should be reasonably attributed to their increased structural disorders (grain boundaries, dislocations and holes), represented by a 3–4 times increase in resistivity compared with that (~20 $\mu\Omega$ cm) of pure cobalt films [12]. These disorders would greatly increase the

field-independent electron scatterings and make the MR effect less manifest in the total measured resistance. Similarly, it might also be the major reason responsible for the negligible MR hysteresis loop observed in the magnetic isotropic continuous films (remanent magnetization ratio > 0.9 and coercivities of tens of Oe), although they indeed showed a resistance difference in the LMR and TMR measurements.

As shown in Fig. 5.6 (*b*), the isotropic 80 nm diameter antidot array exhibited similar butterfly-like LMR and TMR loops. Compared with the negligible MR loops in the isotropic continuous films, these increased magnetoresistive features should have close relations to their severely constrained geometries [1]. In this case, the current trajectories would be confined by the network dimensions. As discussed above, the topology-induced shape anisotropy as well as the stray fields from the channels would force the local domains to align along the networks at low fields with the magnetic moments parallel or antiparallel to the current trajectories. Thus, a high-resistance state would be expected in this situation. When the magnetic field was increased, the local domains would rotate gradually towards the field direction, with an accompanying increment in their average angles with the current trajectories. Thus, a reduction in magnetoresistance at high fields would be expected. Because of the isotropic magnetic properties and long-range disordering of the arrays, no apparent difference in the average angles between the magnetization and the current trajectories would be seen in the longitudinal and transverse MR measurements on increasing fields. It resulted in similar MR loops in both cases, seemingly portraying nearly isotropic magnetoresistive behaviour. In addition, it should be noted that the local sensing current densities in the antidots would be modulated by the empty pores. As numerically simulated [13], the local films defined by

two neighbouring pores would tend to carry less dense current when their networks were directed orthogonally to the macroscopically averaged current direction. It suggested that these parts should have fewer contributions to the total resistance. Correspondingly, the number of high-resistance components in the TMR measurement or low-resistance components in the LMR measurement would be reduced at high fields where magnetization approached saturation. It might additionally result in lower TMR values as compared to LMR, besides the traditional contribution from the intrinsic AMR effect. The observed maximum values for LMR and TMR were changed in the range of 0.05–0.07% at ~240 Oe, close to the coercivities (~220 Oe). The small amplitude was possibly caused by the increased field-independent scattering arising from the pore edges besides the grain boundaries and other crystal defects [14].

5.3.2 Influence of film thickness in the antidot arrays deposited on AAO membranes of $\langle D_p \rangle$ = 80 *nm*

In this part, films growth on the AAO membranes with an average pore diameter $\langle D_p \rangle$ = 80 nm were investigated. Fig. 5.7 shows SEM images of the CoAlO antidot arrays with different film thicknesses, *t*. The porosity features of the antidots showed no obvious changes at $t \leq 40$ nm. Above this thickness, a reduction in pore sizes is clearly observed. When *t* reached 80 nm, only tiny nanopores of less than ~15 nm are observed. The pores almost disappeared when *t* increased to 120 nm. Interestingly, the thick film showed analogous block assembly morphologies as those in the sample shown in Fig. 5.3(a). In the latter case, the block assemblies were from the humped AAO barrier layers and the CoAlO films deposited on them were magnetically continuous. But for the films shown in Fig. 5.7(*c*) and (*d*), cluster assemblies were from the CoAlO composite

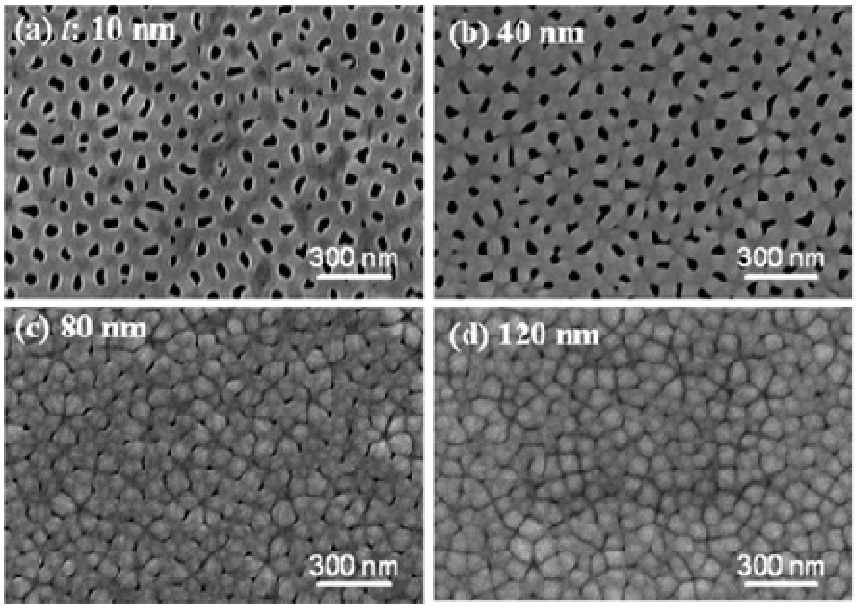

Fig. 5.7 SEM images of the CoAlO composite antidot arrays with different film thickness, *t*. Porosity features of the antidots showed obvious differences as the thickness is increased from 40nm to 80nm.

and formed due to the incomplete vanishing of grain boundaries as the film thickness was increased.

Fig. 5.8 shows minor magnetic hysteresis loops of the CoAlO antidot arrays with different thicknesses, *t*. The arrays with thicknesses of 10 and 40 nm showed hard-like magnetics with large switching field distributions while those of $t \geq 80$ nm were greatly softened with small switching field distributions. No obvious magnetic anisotropy was observed in these antidots. Their coercivities and saturation field H_s are shown in Fig. 5.9. For comparison, the magnetic properties of structurally continuous CoAlO films deposited on AAO barrier layers were also included. For the continuous films, coercivity showed a slight increase when the film thickness was larger than 60 nm. But their anisotropic properties were not influenced by the thicknesses. In the CoAlO antidot arrays with small thickness ($t \leq 40$ nm), large saturation fields, of more than

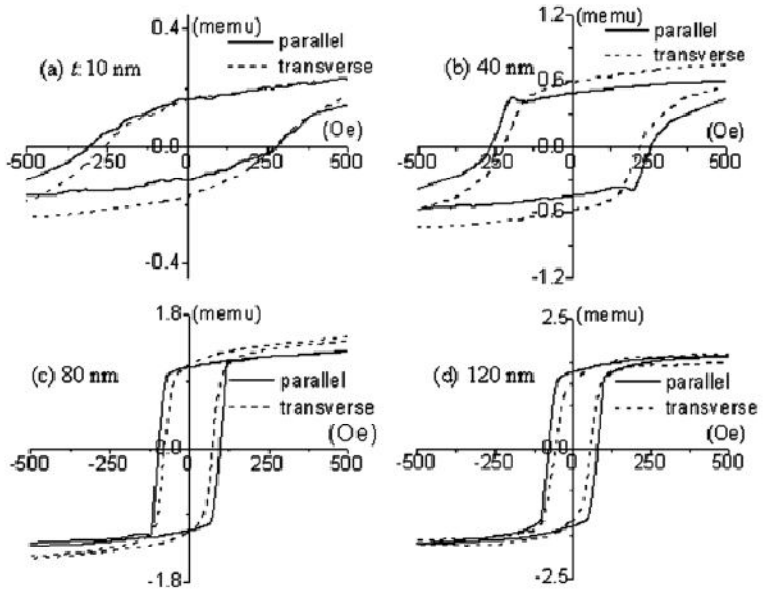

Fig. 5.8 Minor magnetic hysteresis loops of the CoAlO antidot arrays with different film thickness, *t*. The solid and dash lines, respectively, represent the measurement directions parallel or transverse to the external field direction applied during film growth.

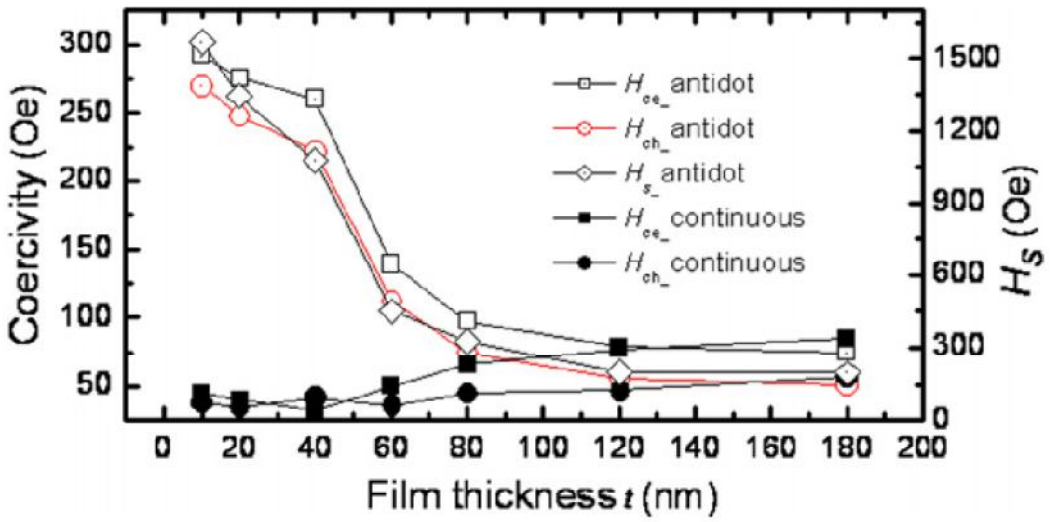

Fig. 5.9 Coercivities (easy axis: $H_{ce\_}$ antidot and hard axis: $H_{ch\_}$ antidot) and saturation field $H_{s\_}$ of the CoAlO antidot arrays as a function of thickness, *t*. As comparison, coercivities (easy axis: $H_{ce\_}$ continuous and hard axis: $H_{ch\_}$ continuous) of the continuous CoAlO films are also included, which were deposited on the AAO barrier layers (as shown in Fig. 5.1(*a*)).

1 kOe, were needed to overcome the local shape anisotropy and the disturbing stray fields from the pore channels. The coercivities and saturation fields showed a quick reduction when t > 40 nm. This happening may be attributed to a possible change in the domain reversal process from domain rotation in the thin antidots to wall motion in the samples of higher structural continuity. In addition, the pinning effect of the material deposited within the pores would become relatively less important as the effective pore size decreased and the network approached a continuous film [3]. This also seemed to be responsible for a reduction in coercivities. The shrunk pores in thick antidot arrays would behave as domain wall pinning sites as discussed above. But it should be noted here that the antidot had an open bottom and the size of the antidot was largest at the bottom, gradually decreasing towards the top surface [1]. Hence, domains in the bottom layer would still be controlled by the topology-induced shape anisotropy and the stray fields from the channels, just as the case in the thin films, where complex domain states would be formed. The orientations of moments in the upper layer would be disturbed by the lower irregularly oriented moments through spin couplings. It was possibly responsible for the isotropic magnetic properties found in the thick films although with high structural continuity. In addition, high dense cluster boundaries formed in these arrays could weaken the coupling interactions across the magnetic clusters, which also tended to result in randomly oriented domains.

Magnetotransport in these antidot arrays with different thicknesses was also measured. When t = 10nm and 40nm, the antidot array showed similar MR loops as shown in Figure 6(b). These could be attributed to the geometrically constrained domain orientations with confined current trajectories, as discussed above. When t = 80nm and 120nm, the antidot

array showed no obvious LMR or TMR loops. The LMR had a constant value while the TMR was almost at zero. As argued previously, the weak AMR effect should result from the large resistance ratio of spin-independent scatterings.

5.4 Conclusions

The AAO membrane technique has been utilized to pattern CoAlO films with controlled porosity features. An anisotropic to isotropic magnetic transition was observed as the pore dimensions were increased, with a critical diameter of about 35 nm. Magnetotransport showed a corresponding variation, as evidenced by a MR change from typical anisotropic to nearly isotropic behaviour on increasing the pore sizes. Magnetism of the antidot arrays, deposited on the large-pored AAO membranes, was softened by increasing the film thickness and showed isotropic magnetic properties.

5.5 References

[1] Z. L. Xiao et al, *Appl. Phys. Lett.* **81**, 2869 (2002).

[2] F. J. Castano, K. Nielsch , C. A. Ross, J. W. A. Robinson and R. Krishnan, *Appl. Phys. Lett.* **85,** 2872 (2004).

[3] J. A. Barnard, A. Butera, H. Fujiwara, V. R. Inturi, J.D. Jarratt, T. J. Klemmer, T. W. Scharr and J. L. Weston, *J. Appl. Phys.* **81**, 5467 (1997).

[4] K. Liu, S. M. Baker, M. Tuominen, T. P. Russell and I. K. Schuller, *Phys. Rev.* B **63**, 060403 (2001).

[5] S. A. M. Tofail, I.Z. Rahmana and M. A. Rahman, *J. Appl. Phys.* **91**, 7998 (2002).

[6] K. Liu and C. L. Chien, *IEEE Trans Mag.* **34**, 1021 (1998).

[7] (a) H. Masuda and K. Fukuda, *Science* **268**, 1466 (1995); (b) H. Chik and J. M. Xu, *Mater. Sci. Eng.* R **43**, 103 (2004).

[8] S. A. Koch, G. Palasantzas, T. Vystavel, J. Th. M. De Hosson, C. Binns C and S. Louch, *Phys. Rev.* B **71**, 085410 (2005).

[9] J. Escriga, P. Landerosa, D. Altbira, E. E. Vogelb and P. Vargas, *J Magn. Magn. Mater.* **308**, 233 (2007).

[10] K. Nielsch, F. J. Castano, S. Matthias, W. Lee and C. A. Ross, *Adv. Eng. Mater.* **7**, 217 (2005).

[11] T. R. McGuire and R. I. Potter, *IEEE Trans. Magn.* **11**, 1018 (1975).

[12] G. S. M. Rijks, R. Coehoorn, M. J. M. de Jong and W. J. M . de Jonge, *Phys. Rev.* B **51**, 283 (1995).

[13] C. C. Wang, A. O. Adeyeye and N. N. Singh, *Nanotechnology* **17**, 1629 (2006).

[14] G. Woosik, G. Detlef, H. Michael and K. Jürgen, *Phys. Rev.* B **72**, 13440 (2005).

Chapter 6 Exchange bias in pore modified FeNi/FeMn multilayer antidot arrays

6.1 Introduction

Although there have been a few works which studied the exchange bias of antidot arrays [1,2], to our best knowledge, there has been no work investigating the microwave properties of exchange-biased multilayered antidot arrays. It is well known that exchange bias effect can be used to extend the ferromagnetic resonance (FMR) frequency and there have been several reports [3-7] to employ exchange bias for microwave applications. However, these studies only focused on the microwave properties of exchange-biased multilayer thin films [3-7]. Therefore in this Chapter, microwave properties of Permalloy-FeMn multilayer antidot arrays in conjunction with their magnetic and structural properties as a function of Permalloy thickness and pore size were systemically investigated.

6.2 Experiment

6.2.1 Fabrication of AAO membrane

Fabrication procedure of the antidot arrays, including the preparation of anodic aluminum oxide (AAO) membranes, is sketched in Fig. 6.1. AAO membranes were fabricated as follows. First, a pure aluminum foil (99.5%) annealed at 500 °C for 5 h was first electropolished in a solution of perchloric acid and ethanol (1:4 vol %). It was then anodized at a constant voltage of 40 V in a 0.3 M oxalic acid solution at 0 °C for 15 h. By this way, we can fabricate AAO membranes with pore sizes ranging from 30 to 80 nm and an interpore distance fixed at about 120 nm, as shown in Fig. 6.2. Scanning electron

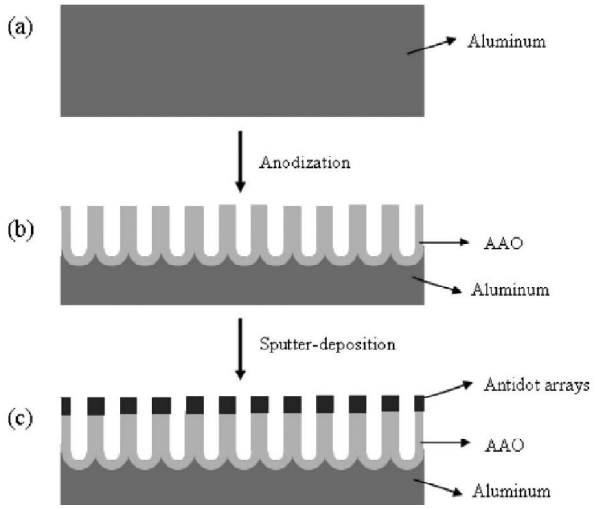

Fig. 6.1 Schematic diagram of the fabrication process of the multilayered antidot arrays.

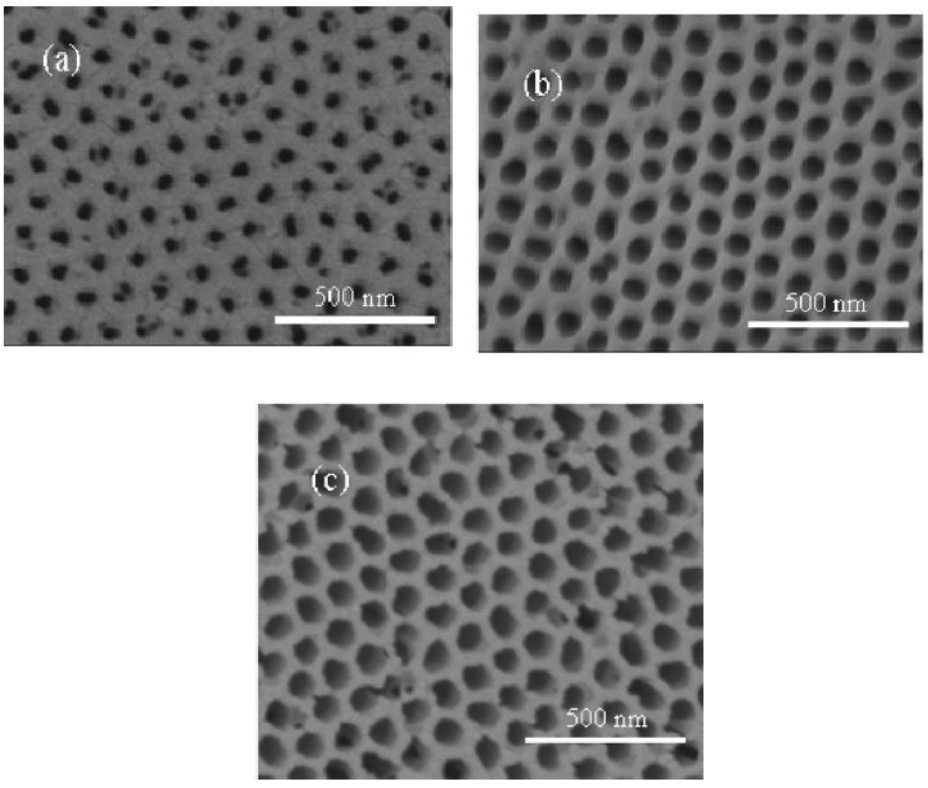

Fig. 6.2 SEM images of the AAO templates with the average pore sizes of (a) 30 nm, (b) 60 nm, and (c) 80 nm.

microscope (SEM) images revealed that the templates had a high hexagonal ordering. They also showed high uniformity in the pore size except for the sample with pore size of 30 nm.

6.2.2 Fabrication of FeNi/FeMn multilayered antidot arrays

The antidot arrays were fabricated by deposition of $[Fe_{20}Ni_{80}/Fe_{50}Mn_{50}$ (15 nm)$]_{10}$ multilayers with various thicknesses of $Fe_{20}Ni_{80}$ (Permalloy) onto the AAO substrates at ambient temperature using a reactive rf magnetron sputter-deposition system with a base pressure better than $7x10^{-7}$ Torr. A magnetic field of about 200 Oe was applied in the plane of the films to induce a unidirectional anisotropy. The argon pressure was kept at 10^{-3} Torr during the deposition process.

6.2.3 Characterization

Phase compositions of the samples were characterized by using an X-ray diffractometer with Cu *K*α radiation. Their magnetic properties were measured by an *M*-*H* loop tracer at room temperature. Permeability spectra over 0.05 - 5 GHz were obtained by a shorted microstrip transmission-line perturbation method using a fixture developed in our laboratory. Further details of this method can be found in our previous publication [8].

6.3 Results and discussion

Presented in Fig. 6.3 are hysteresis loops of the antidot arrays of [FeNi(40 nm) /FeMn(15 nm)]$_{10}$ multilayers on the substrates with various pore sizes (denoted as *d* in Fig. 6.3) in both hard and easy axes. For continuous thin films, the pore size is equal to zero. The easy axis direction is defined as the direction of the field applied during

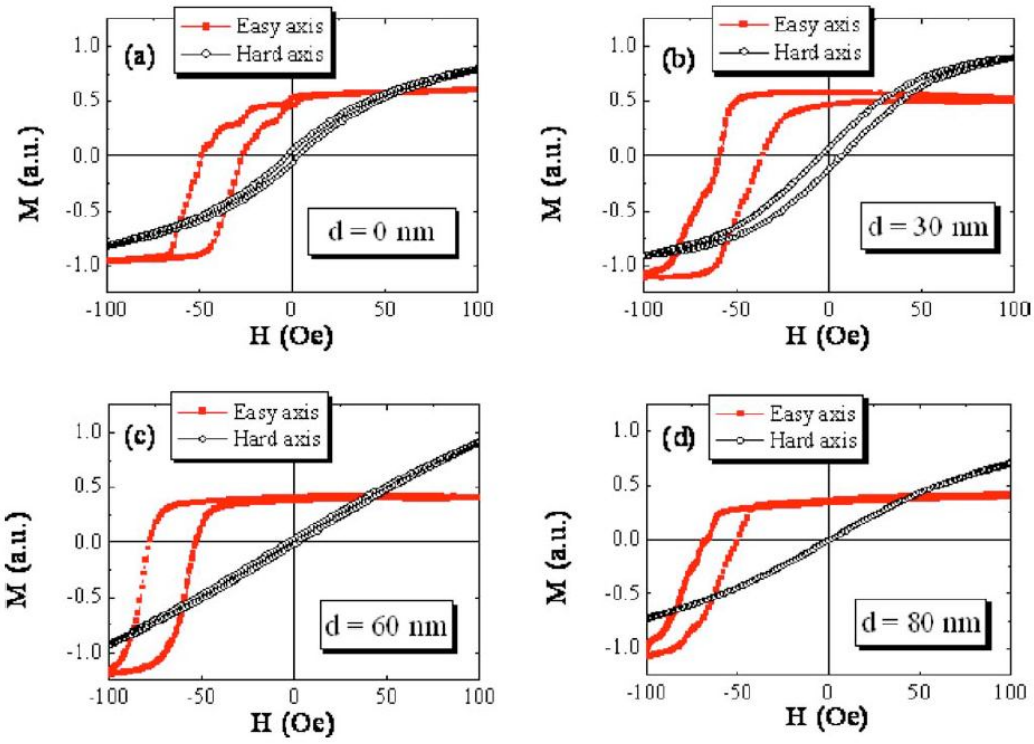

Fig. 6.3 Hysteresis loops of the [FeNi(40 nm)/FeMn(15 nm)]$_{10}$ multilayered antidot arrays on the substrate with various pore sizes measured at room temperature: (a) d = 0 nm, (b) d = 30 nm, (c) d = 60 nm, and (d) d = 80 nm. (d is diameter of pore of the AAO template and d = 0 is for the continuous thin film.)

deposition while the hard axis is in the direction perpendicular to the easy axis but still in the plane of the sample. The reason for using the in-plane hard axis instead of the out-of-plane hard axis as typical definition is that in this case we only concern with the anisotropy induced by applying the field during the deposition. If using out-of-plane axis as the hard axis, the situation will be more complicated as we have to look into the shape anisotropy contribution. As seen in Fig. 6.3, the easy axis hysteresis loops have obvious loop shift as a result of exchange bias coupling between the FeNi and FeMn layers. It is noted that there are multiple-stage magnetization reversals in the M-H loops, which are possibly ascribed to the different interfacial exchange energies at different interfaces resulting in different exchange bias fields (H_E) acting on each FeNi layer. Due to the

overlap of several hysteresis loops with different exchange bias fields, the hysteresis loop manifests itself as a multiple-stage reversal. Previously, several groups [9,10] observed similar behavior for exchange-biased systems using FeMn as an antiferromagnetic (AF) layer, where they claimed that the bottom interface normally had a better unidirectional anisotropy constant.

It is seen that the steps in the *M-H* loops gradually disappear as the pore size is increased, indicating that, in these antidot arrays, the unidirectional anisotropy constant at the top interface is not much different from that of the bottom. This may possibly be attributed to the defects in the antidot structures, causing some uncompensated spins at edges of the antidots so that the exchange bias at top interface is almost the same as that of the bottom. However, further study is needed to clarify this point. Another interesting point that should be mentioned is the vertical shift of the hysteresis loops, which was similarly observed by other researchers [11,12]. The physical origin of this vertical shift is still in controversy. Kagerer *et al*. [11] ascribed this behavior to piezomagnetism induced by residual shear stress, while Arenholz *et al.* [12] related this shift to pinned AF spins. The shift in the present work is quite large (up to 50%), as compared to the results reported in Ref. 12 (less than 1%). As a result, the vertical shift is not likely due to the pinned AF spins as claimed by Arenholz *et al.* [12] and the interpretation of this effect in terms of piezomagnetism by Kagerer *et al.* [11] seems to be more suitable.

By comparing the *M-H* loops in Fig. 6.3, one can clearly see that as the pore size is increased, the easy axis hysteresis loop is shifted more to the negative direction, indicating an enhancement of exchange bias field with increasing pore size. The Permalloy thickness dependences of the exchange bias field (H_E), the uniaxial anisotropy

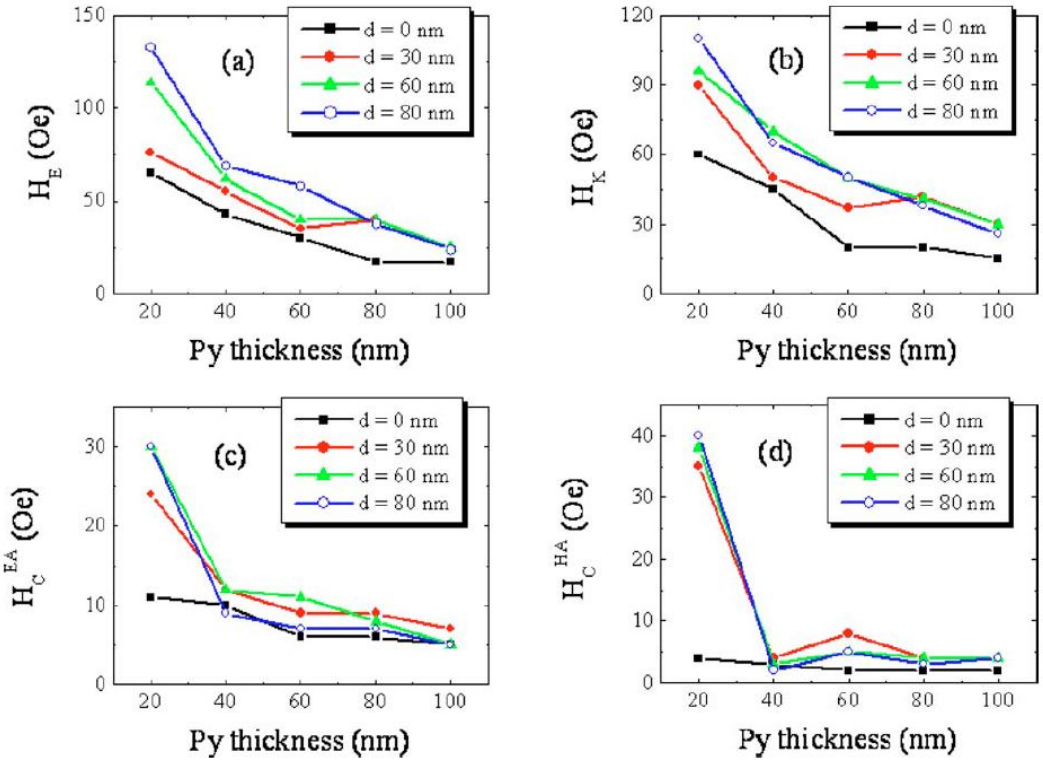

Fig. 6.4 (a) Exchange bias field (H_E), (b) uniaxial anisotropy field (H_K), and coercivity [in (c) easy axis and (d) hard axis] as a function of Permalloy thickness for the [FeNi(x nm) /FeMn(15 nm)]$_{10}$ multilayered antidot arrays on the substrates with various pore sizes.

field (H_K), and the coercivities in easy and hard axes (H_C^{EA} and H_C^{HA}), as a function of pore size, are summarized in Fig. 6.4. As clearly seen in Figs. 6.4(a) and 6.4(b), the antidot arrays exhibit larger exchange bias field and uniaxial anisotropy field, as compared to the continuous films. Liu *et al.*[1] reported similar observations in FeF_2/Fe antidot arrays. This behavior can be qualitatively explained by employing the random field model proposed by Li and Zhang [13]. According to this model, the FM domain size is determined by the competition between FM-FM exchange interaction and the random field due to the interfacial FM-AF interaction. When multilayers are geometrically confined in a lateral dimension as those in this work, the FM-FM interaction will be reduced, resulting in smaller FM domains and larger net random fields.

It thus explains why the exchange bias field is increased with increasing pore size. Besides, it is interesting to see in Fig. 6.4(a) that, when thickness of the Permalloy layer is large, the enhancement of exchange bias field is less. This behavior can also be explained by using the random field model. When the FM layer is thick enough, even though the lateral dimension is confined, the FM-FM interaction is still strong, because the vertical dimension now has a more significant role. Therefore, in the samples with thick FM layers, when the pore size is increased, the FM domain size is not decreased as much as that in the samples with thinner FM layers, and consequently the exchange bias does not change much. The present result thus provides a firm support to the random field model. It is known that exchange coupling between ferromagnets and antiferromagnets can induce not only unidirectional anisotropy but also uniaxial anisotropy [14]. Hence, the behaviors of uniaxial anisotropy field (H_K) and coercivity (H_C) are expected to be similar to that of H_E, as one can see in Figs. 6.4(b) – 6.4(d).

Fig. 6.5 presents imaginary $\left(\mu''\right)$ permeability spectra of the multilayered antidot arrays with various pore sizes. The peak in the imaginary permeability spectrum corresponds to the microwave resonance frequency [3-7]. It is observed that the resonance frequency is decreased as the thickness of Permalloy is increased. For continuous film (d=0 nm), the resonance frequency is increased from 1. 4 to 3.1 GHz as the FeNi layer thickness is reduced from 100 to 20 nm, while for the antidot arrays with the largest pore size (d=80 nm), the resonance frequency is changed from 2 to 4.1 GHz. The dependence of the resonance frequency on the Permalloy thickness is summarized in Fig. 6.6. It is noted that there are multiple peaks corresponding to several resonance frequencies. The main purpose of this paper is to explore the possibility of using antidot

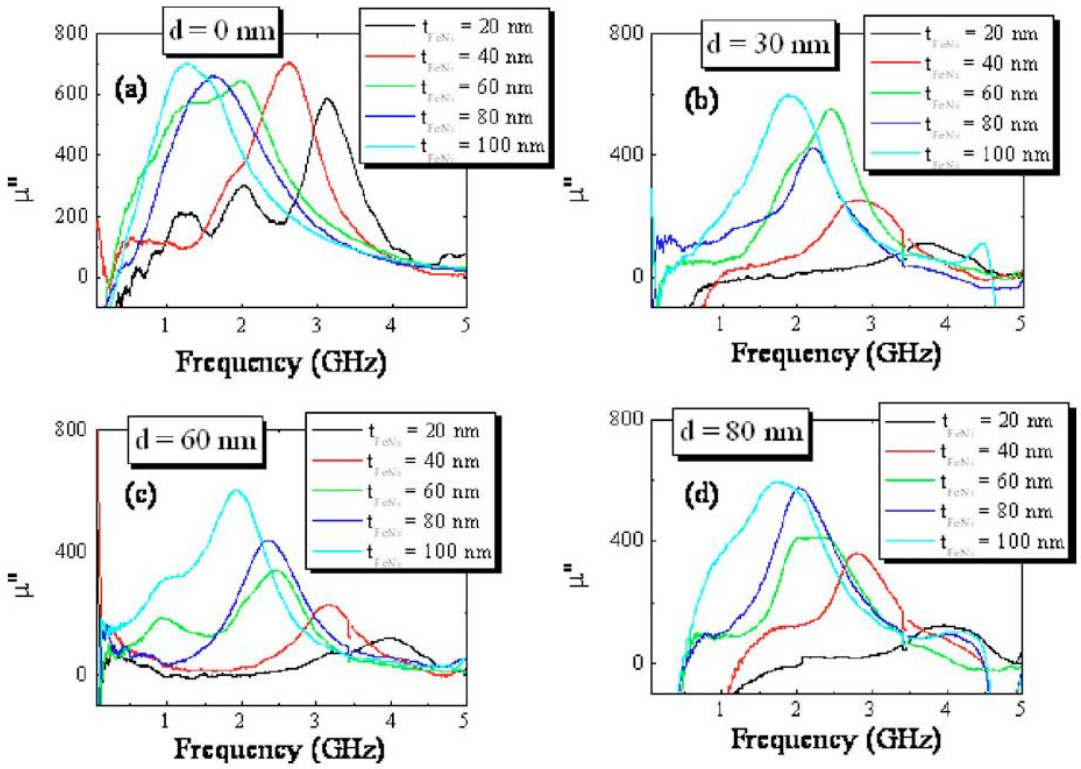

Fig. 6.5 Imaginary $(\mu^{"})$ permeability spectra of the [FeNi(x nm)/FeMn(15 nm)]$_{10}$ multilayered antidot arrays with various pore sizes measured at room temperature: (a) d = 0 nm, (b) d=30 nm, (c) d = 60 nm, and (d) d = 80 nm.

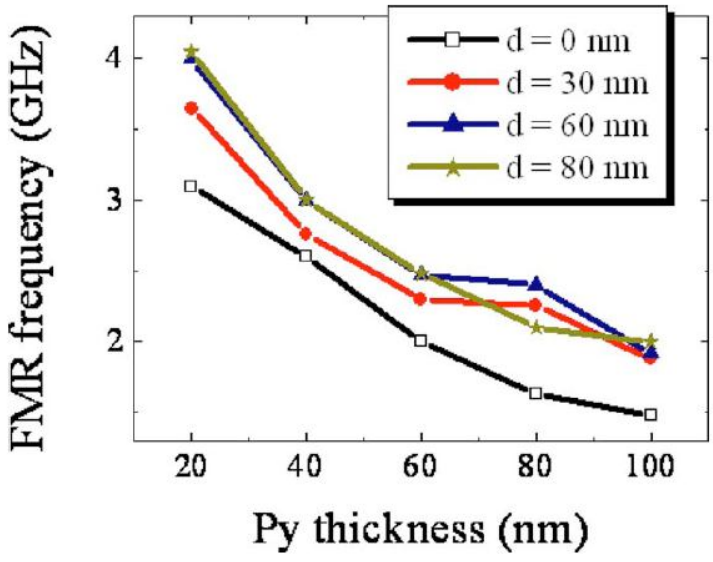

Fig. 6.6 Permalloy thickness dependence of the FMR frequency for [FeNi (x nm) /FeMn(15 nm)]$_{10}$ multilayered antidot arrays with various pore sizes.

arrays for microwave applications so that for comparison, one should compare the highest resonance frequency that each system can have. Hence, in this case we only choose the highest resonance frequency for analysis. Microwave resonance frequency can be written as follows [6]:

$$f_{FMR} = \frac{\gamma}{2\pi}\sqrt{(H_k + H_E)(H_k + H_E + 4\pi M_s)}$$

where, γ is gyromagnetic ratio (γ=1.76 x 10^7 Hz/Oe), M_S is saturation magnetization ($4\pi M_S$ = 10 kOe), H_K is anisotropy field, and H_E is exchange bias field. From this equation, it is expected that the resonance frequency is significantly affected by the pore in a similar way to the exchange bias field and the uniaxial anisotropy field. It is well known that, for microwave applications, resistance of a material should be as large as possible to avoid the eddy current effect. Antidot arrays are known to have larger resistance as compared to continuous thin films due to the presence of the pores. Antidot arrays are thus promising for microwave applications, since they meet both criteria: high resistance and high resonance frequency. For example, comparing with the resonance frequency of Permalloy/IrMn (about 2 GHz) [5], our Permalloy/FeMn antidot arrays have resonance frequencies of up to to 4.1 GHz.

6.4 Conclusions

In summary, we have studied magnetic and microwave properties of the magnetic multilayered antidot arrays with different pore sizes. It is found that exchange bias and microwave resonance frequency can be increased significantly by increasing the pore size of the antidot arrays. By using the antidot arrays in the optimized condition (FeNi thickness of 20 nm and pore size of 80 nm), one can increase the exchange bias

field from 65 to 135 Oe and the resonance frequency can be increased from 3.1 to 4.1 GHz accordingly. This result demonstrates that antidot arrays with exchange-biased FM/AF configurations can be promising candidates for microwave applications.

6.5 References

[1] K. Liu, S. M. Baker, M. Tuominen, T. P. Russell, and I. K. Schuller, *Phys. Rev. B* **63**, 060403 (2001).

[2] M. I. Montero, K. Liu, O. M. Stoll, A. Hoffmann, J. J. Akerman, J. I. Martin, J. L. Vicent, S. M. Baker, T. P. Russell, C. Leighton, J. Nogués, and I. K. Schuller, *J. Phys. D* **35**, 2398 (2002).

[3] O. Acher, S. Queste, K.-U. Barholz, and R. Mattheis, *J. Appl. Phys.* **93**, 6668 (2003).

[4] B. K. Kuanr, R. E. Camley, and Z. Celinski, *J. Appl. Phys.* **93**, 7723 (2003).

[5] S. Queste, S. Dubourg, O. Acher, K. U. Barholz, and R. Mattheis, *J. Appl. Phys.* **95**, 6873 (2004).

[6] M. Sonehara, T. Sugiyama, T. Sato, K. Yamasawa, and Y. Miura, *IEEE Trans. Magn.* **41**, 3511 (2005).

[7] D. Y. Kim, C. O. Kim, M. Tsunoda, M. Yamaguchi, S. Yabugami, and M. Takahashi, *J. Appl. Phys.* **101**, 09E511 (2007).

[8] Y. Liu, L. F. Chen, C. Y. Tan, H. J. Liu, and C. K. Ong, *Rev. Sci. Instrum.* **76**, 063911 (2005).

[9] A. M. Alsmadi, S. G. E. te Velthuis, G. P. Felcher, and C. G. Kim, *J. Appl. Phys.* **101**, 09E522 (2007).

[10] B. T. Bolon, M. A. Haugena, A. Abin-Fuentesa, J. Deneena, C. B. Cartera, and C. Leighton, *J. Magn. Magn. Mater.* **309**, 54 (2007).

[11] B. Kagerer, Ch. Binek, and W. Kleemann, *J. Magn. Magn. Mater.* **217**, 139 (2000).

[12] E. Arenholz, K. Liu, Z. Li, and I. K. Schuller, *Appl. Phys. Lett.* **88**, 072503 (2006).

[13] Z. Li and S. F. Zhang, *Phys. Rev. B* **61**, R14897 (2000).

[14] J. Nogués and I. K. Schuller, *J. Magn. Magn. Mater.* **192**, 203 (1999).

Chapter 7 Infiltrating P3HT polymer into ordered TiO_2 nanotube arrays

7.1 Introduction

Infiltration of polymers into nanostructured metal oxides is of particular importance for optimizing the performances of the hybrid photovoltaic devices. Wet processing deposition techniques, such as spin-coating, dip-coating, drop-casting, doctor-blading, inkjet-printing, and screen-printing, are attractive approach to cast polymer films into nanostructured metal oxides from solutions [1-6].There are detailed reports on the efficiency of infiltration of poly(3-hexyl thiophene) (P3HT) conjugated polymer into titania mesoporous films with different morphologies. Coakley et al. [7] infiltrated P3HT polymer into thin mesoporous (50–300 nm) TiO_2 film with uniform pore sizes (10 nm) by spin coating. Bartholomew and Heeger [8] infiltrated P3HT polymer into 2.2 μm thick random nanocrystalline TiO_2 networks (RNTNs) by spin coating. Recently, polymer was incorporated into TiO_2 porous films by chemical in situ polymerization of a soluble, low molecular weight monomer instead of inserting from solution of a high molecular weight polymer into the pores [9,10].

In this Chapter, TiO_2 nanotube arrays were formed by anodizing titanium foil in an electrolyte mixture that consisted of 0.25 wt% NH_4F and 2 vol% H_2O dissolved in ethylene glycol and P3HT polymer was infiltrated into the TiO_2 nanotube arrays by a dip-coating method. The TiO_2 nanotubes had a large diameter of about 60 nm. The morphology of TiO_2 nanotubes is radically different from that of mesoporous TiO_2 films. TiO_2 nanotube arrays offer straight nanopores while the mesoporous TiO_2 films which are made of an interconnected network can have inaccessible internal voids that might

hinder infiltration of polymers. By using time-of-flight secondary ion mass spectrometer (TOF-SIMs) depth profiling, transmission electron microscopy (TEM), UV–Vis absorption spectrometer measurement and scanning electron microscopy (SEM), we are able to show that P3HT polymer can be readily infiltrated into the TiO_2 nanotube arrays.

7.2 Experiment

7.2.1 Fabrication of TiO_2 nanotube arrays

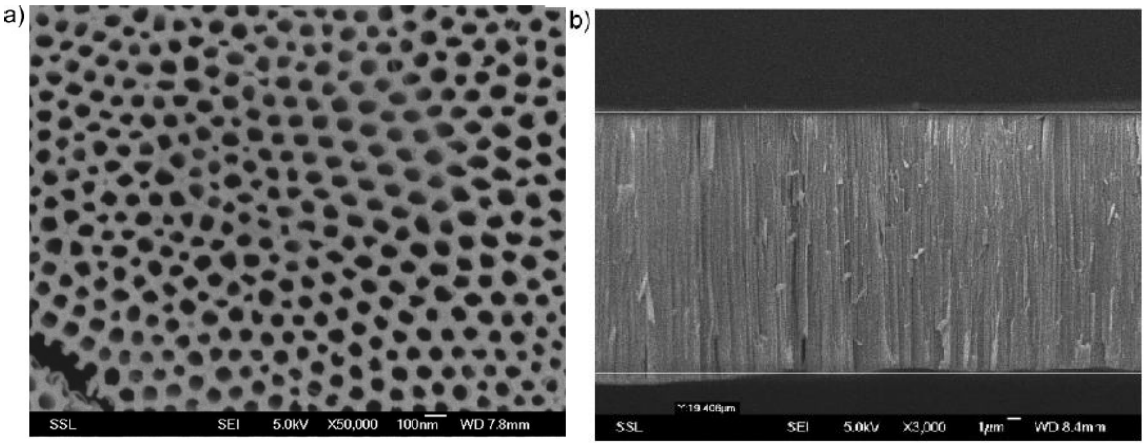

Fig. 7.1 (a) SEM image of top view of the TiO_2 nanotube arrays formed from 2-step anodization of titanium foil in ethylene glycol- based solution. (b)SEM image of side view of the TiO_2 nanotube arrays. The thickness of the TiO_2 nanotube arrays is around 19 μm.

Before anodization, the titanium foil was degreased ultrasonically in acetone for 5 min, then rinsed in distilled water and dried in hot air. The titanium foil was first anodized for 24 h in an electrolyte mixture containing 0.25 wt% NH_4F and 2% distilled water dissolved in ethylene glycol. The anodization was performed in a two-electrode configuration with titanium foil as working electrode and graphite rod as counter electrode, at a constant voltage of 40 V at 22 ^oC. The nanotubes formed from the first anodization were detached completely from the titanium substrate by placing

masking tape over the nanotubes and peeling off the masking tape. Then, the titanium foil was degreased and dried in hot air before second anodization. The second anodization was performed using the same conditions as in the first anodization except that the time was 7 h instead of 24 h. Finally, the nanotubes were rinsed thoroughly with distilled water. The nanotube arrays formed by the 2-step anodization were completely free from surface debris. The presence of surface debris could limit the infiltration efficiency of P3HT polymer. SEM images of the TiO_2 nanotube arrays are presented in Fig. 7.1. Diameter of the TiO_2 nanotubes is 60 nm and thickness of the template is about 19 μm.

7.2.2 Infiltration of polymer into the TiO_2 nanotube arrays

The nanotube arrays were immersed for 24 h in 10 mg/mL solution of regioregular poly(3-hexyl thiophene) (RR P3HT) in chlorobenzene at 65 ^oC. Average molecular weight (Mn) and polydispersity of the RR P3HT used in this work are 25 500 g/mol and 1.48, respectively. Its radius of chains is in the range of 8.5–10.6 nm [11]. For the characterization with UV–Vis absorption spectra, TOF-SIMs depth profiling and TEM, the TiO_2 nanotubes filled with polymer were first rinsed in chlorobenzene several times before drying in a vacuum oven at 65 ^oC for 1 h to remove the thick layer of polymer on surface of the TiO_2 nanotubes. For the characterization with SEM, the samples were left to dry in a vacuum oven at 65 ^oC for 1 h without rinsing in chlorobenzene.

7.2.3 Characterization

UV–Vis absorption spectra were recorded with a UV–Vis spectrometer. Prior to the spectrometer measurement, a transparent Scotch tape was pasted over the TiO_2 nanotube arrays infiltrated with polymer, which was peeled off to detach the TiO_2 film from the titanium substrate. The Scotch tape with the TiO_2 film was then pasted over the

transparent glass slide for spectrometer measurement.

To study the infiltration of the polymer near the top surface of the nanotubes, TOF-SIMs depth profiling was used to monitor the count of TiO^-, S^-, and C^- ions. The depth of the crater of the TiO_2 nanotube arrays created during surface ablation used in the TOF-SIMs depth profiling was measured with a step profiler. The depth etched during the profiling was 500 nm.

Transmission electron microscopy was used to characterize morphology of the P3HT/TiO_2 nanotube arrays. Energy dispersive X-ray (EDX) spectroscopy was employed to study chemical composition within the nanotube arrays. To prepare sample for TEM measurement, the P3HT/TiO_2 nanotube arrays were scraped off from the titanium substrate with a penknife and physically ground into powders to avoid chemical contamination. Powders of the sample were dropped onto on a copper grid coated with a carbon film for TEM observation. Before that, large particles on the TEM grid were blown away with a gas gun.

Scanning electron microscopy was used to study morphology of the P3HT nanotubes within the TiO_2 nanotubes by etching it in a solution consisting of 0.125 vol% HF. Direct etching from the top of the TiO_2 nanotubes with dilute HF solution was not possible due to a layer of polymer coating on the top surface of the nanotube arrays. Thus, the top polymer overlayer together with some of TiO_2 nanotube must be mechanically polished away before the TiO_2 nanotubes can be etched from the top. To etch the TiO_2 nanotubes from the bottom, Scotch tape was first placed over the surface of TiO_2 nanotubes filled with polymer and peeled off to detach the TiO_2 film from the titanium substrate. The Scotch tape with the TiO_2 film was stuck onto a titanium foil with the bottom of the

nanotubes facing upward. The bottom of the TiO_2 nanotubes was etched open to reveal the P3HT nanotubes by soaking it in a dilute HF solution.

7.3 Results and discussion

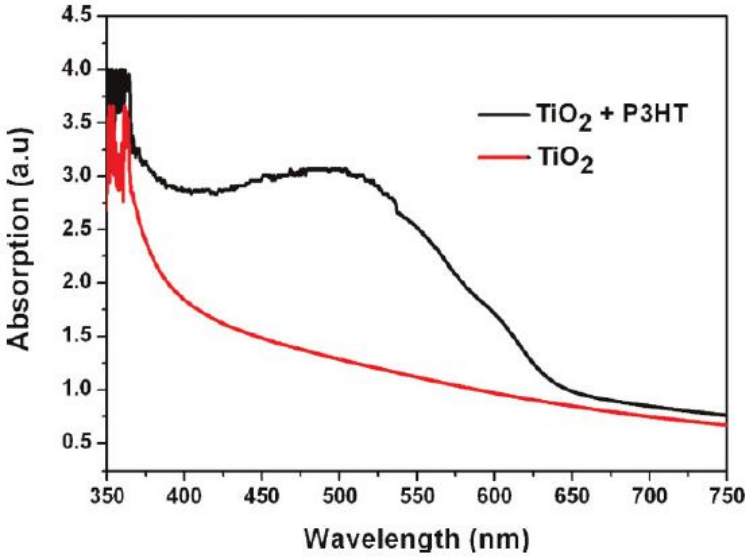

Fig. 7.2 UV–Vis absorption spectra of the empty TiO_2 nanotube arrays (red line) and TiO_2 nanotube arrays infiltrated with P3HT polymer (black line).

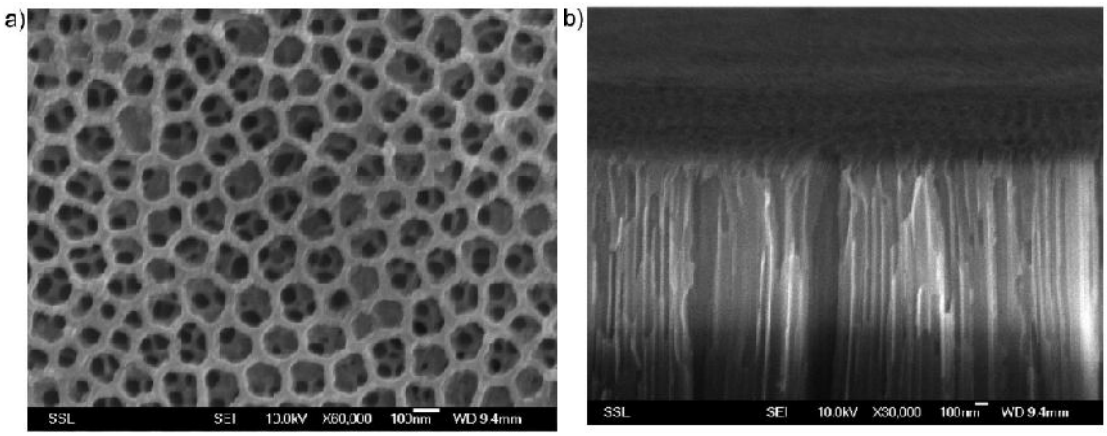

Fig. 7.3 (a) SEM image of top view of the TiO_2 nanotube arrays infiltrated with polymer and rinsed with chlorobenzene to remove excess layer. (b) SEM image of side view of the TiO_2 nanotube arrays infiltrated with polymer and rinsed with chlorobenzene to remove excess layer.

UV–Vis absorption spectra of the bare TiO_2 nanotube arrays and the P3HT/TiO_2 nanotube arrays are presented in Fig. 7.2. It is clear that the absorption peak at 500 nm for the P3HT/TiO_2 nanotube arrays is due to the polymer embedded within the TiO_2 nanotube arrays [7]. The thick layer of the polymer on top of the nanotubes was removed by rinsing in chlorobenzene as seen from Fig. 7.3 (a) and (b). Fig. 7.3(a) shows that, even though some of the pores of the TiO_2 nanotubes are filled up with polymer, the nanotube walls are clearly visible. From Fig. 7.3 (b), there is no distinctive layer of polymer on surface of the TiO_2 nanotube arrays. Thus, there is no overlayer of polymer on top of the nanotubes contributing to the absorption spectra.

TOF-SIMs depth profiling of the P3HT/TiO_2 nanotube arrays is presented in Fig. 7.4. The signal from S^- and C^- ions observed in Fig. 7.4 is entirely attributed to the embedded P3HT polymer and is homogeneous throughout the depth profile. The intensity of S^- and C^- ions signal is proportional to the polymer concentration at a given point, whereas the

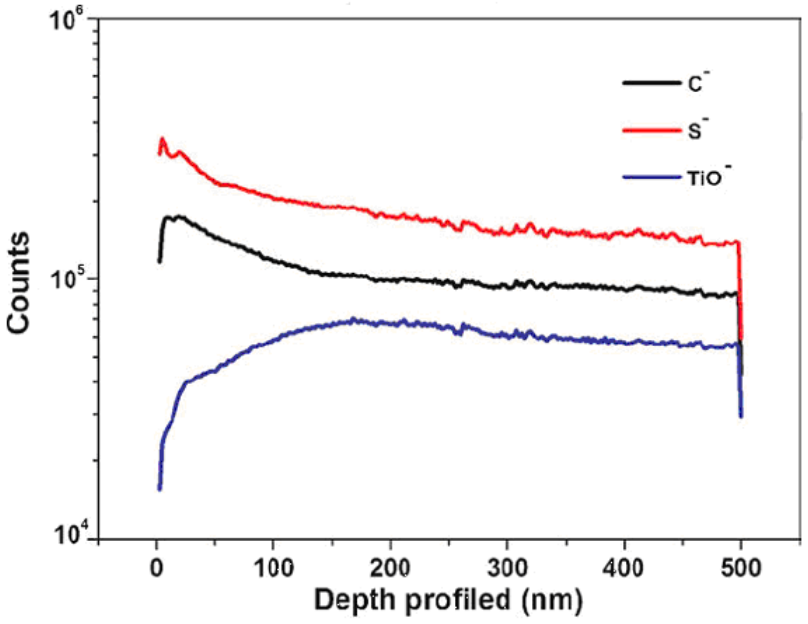

Fig. 7.4 TOF-SIMs depth-profiling trace.

intensity of TiO^- ion signal is affected by TiO_2 nanotube array porosity. As the depth profiled is increased from 0 to 150 nm, the counts of C^- and S^- ions decreased, while the counts of the TiO^- ion increased. From Fig. 7.3(a), there were areas in TiO_2 nanotube arrays where there was a thin overlayer of TiO_2 nanotube array, which was left behind from the imprint of the peeled TiO_2 nanotubes from the 1st anodization. The diameter of this thin overlayer of TiO_2 nanotubes was larger than the diameter of the TiO_2 nanotube underneath it. As a consequence, the count of TiO^- ions increased as the porosity of the tubes decreased with depth profiled from 0 to 150 nm. A thin P3HT polymer coated onto this overlayer of TiO_2 nanotube array account for the C^- and S^- ions counts at a depth of 150 nm dropping to 57% of C^- and S^- ions counts at a depth of 0 nm. This observation is in contrast to the result reported by Bartholomew and Heeger [8] who infiltrated P3HT polymer into thick RNTNs (thickness = 2.2 μm and diameter = 60–70 nm) by spin coating. The transition from the polymer overlayer to RNTNs is distinct at 200 s. At 200 s, the carbon signal dropped to 0.5% of the polymer overlayer signal when there is no heating applied to melt the polymer. Even heating of the polymer, only 3% of the polymer can be incorporated into the RNTNs. Therefore, it is clear that the inaccessible internal voids present in the thick RNTNs hindered infiltration of the polymer. Coakley et al. [7] infiltrated P3HT polymer into ordered network of thin TiO_2 film (the thickness is 50–300 nm and the pore diameter is 10 nm) by spin coating and examined the infiltration of the P3HT polymer into the TiO_2 film by using depth-profiling X-ray photoelectron spectrometer (XPS). In his case, with heating the polymer to 200 ^oC, the carbon signal is also homogeneous throughout the depth profile. This indicated that most of the spin-coated polymer can infiltrate into the thin mesoporous TiO_2 film. Using a thin TiO_2

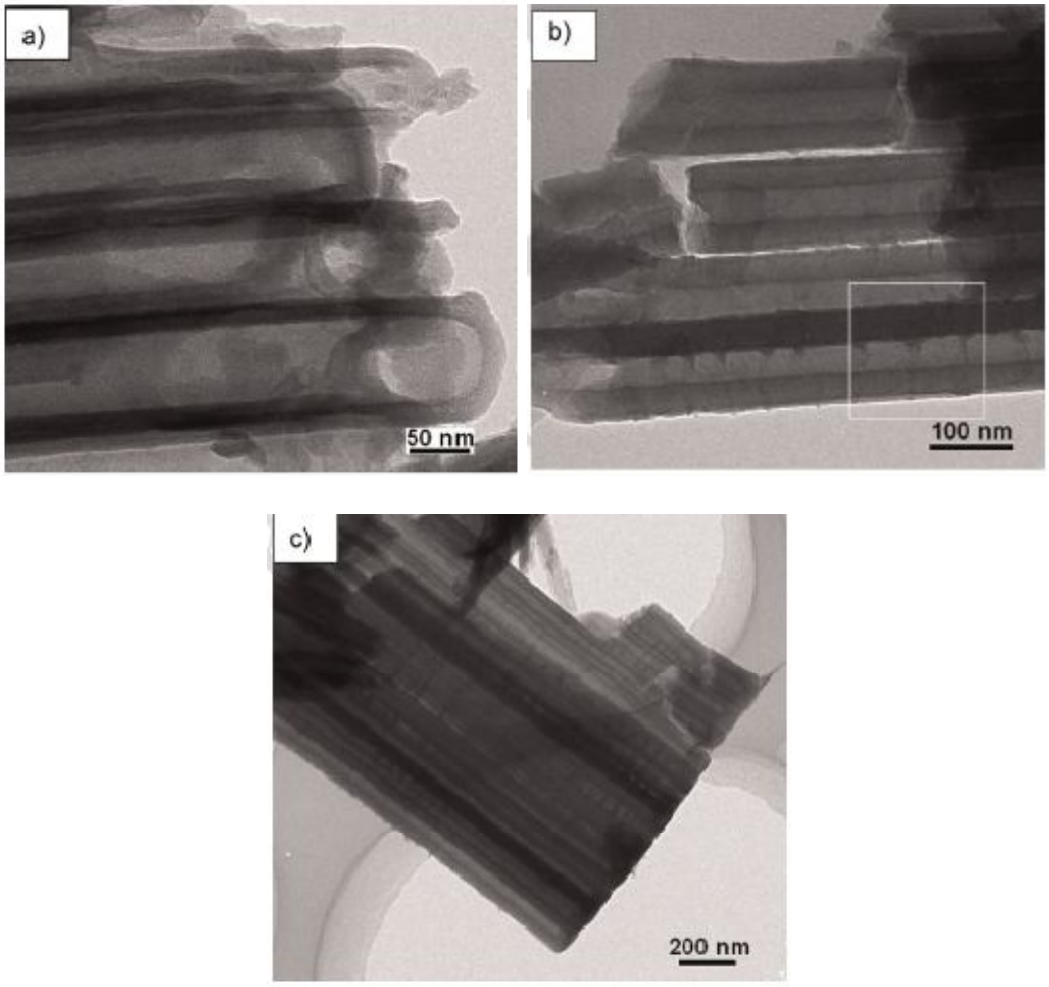

Fig. 7.5 TEM images of the TiO_2 nanotube arrays infiltrated with P3HT polymer. (a) Top end of the nanotube arrays. (b) Side view of the nanotube arrays. The white box indicates the area of the P3HT/TiO_2 nanotube arrays on which EDX measurement is done. (c) Bottom end of the nanotube arrays.

mesoporous film with uniform pore size can improve the infiltration efficiency of P3HT polymer.

Fig 7.5 (a) shows TEM image of top end of the P3HT/TiO_2 nanotube arrays, which is in sharp contrast to the morphology of bottom end of the arrays where all the tubes are well aligned, as shown in Fig. 7.5(c). TEM image of side view of the P3HT/TiO_2 nanotube arrays is displayed in Fig. 7.5(b). To analyze chemical composition of the area

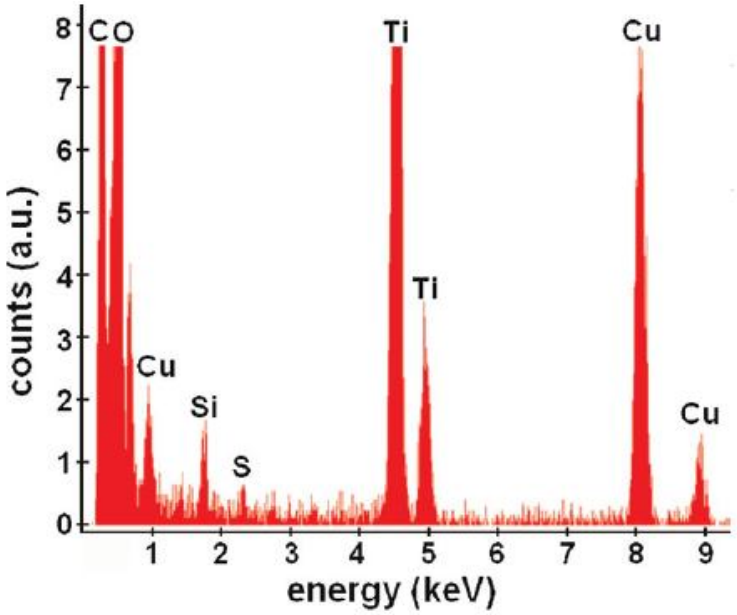

Fig. 7.6 EDX of the TiO_2 nanotube arrays infiltrated with P3HT polymer. The measurement is performed on the area indicated by the square box in Fig. 7.5(b).

within the box on Fig. 7.5(b), EDX spectrum analyses were performed, and a typical result is presented in Fig. 7.6. From Fig. 7.6, the major elements detected are C, O, Ti, S, and Cu. Cu signal is from the Cu grid, as commonly seen in EDX spectra using TEM. The presence of sulfur and carbon elements indicates that the polymer was infiltrated into the pores of the TiO_2 nanotube arrays. In particular, we can see that the pore of the TiO_2 nanotube arrays in Fig. 7.5(b) is filled up with P3HT polymer.

Fig. 7.7(a) shows SEM top view of the TiO_2 nanotubes arrays infiltrated with polymer after the top polymer overlayer and thin TiO_2 overlayer were mechanically polished away. From this figure, we can see that the pores of the TiO_2 pores are not completely filled up with polymer. Instead, the walls of the TiO_2 pores were coated with a thin layer of P3HT polymer which formed nanotubes. Fig. 7.7(b) shows SEM image of the P3HT nanotubes after the top polymer overlayer and the thin TiO_2 overlayer were

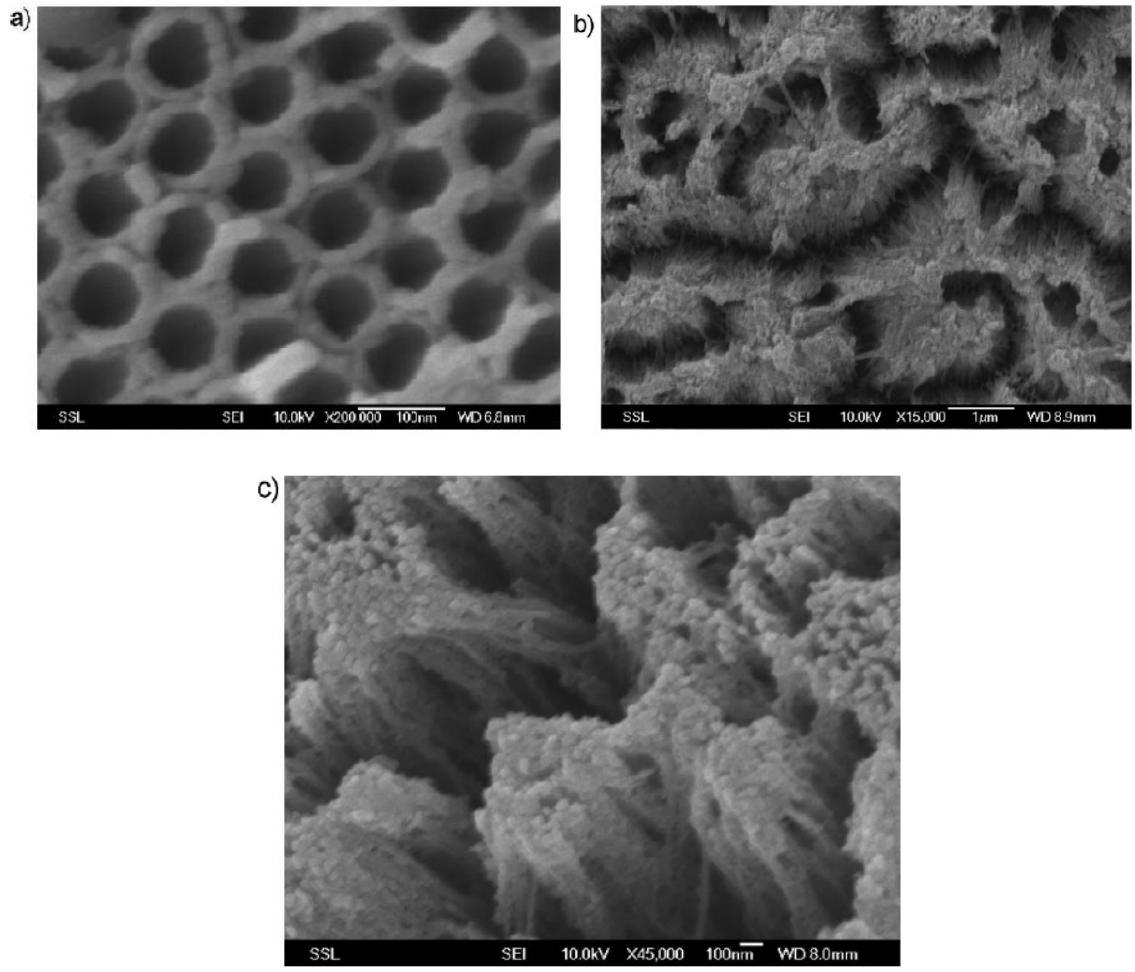

Fig. 7.7 (a) SEM image of the TiO_2 nanotubes arrays infiltrated with polymer after the top polymer overlayer and thinTiO_2 overlayer were mechanically polished away. (b) SEM image of the P3HT nanotubes obtained by etching the top of TiO_2 nanotubes infiltrated with polymer after the top polymer overlayer and thin TiO_2 overlayer were mechanically polished away. (c) SEM image of the P3HT nanotubes obtained by etching the bottom of TiO_2 nanotubes using 0.125 vol% HF solution.

mechanically polished away and the P3HT/TiO_2 nanotubes were then etched in diluted HF solution. Fig. 7.7(c) shows SEM image of the P3HT nanotubes obtained by etching the bottom of the TiO_2 nanotubes infiltrated with polymer with diluted HF solution. From Fig.7.7, we can conclude that the polymer solution was infiltrated into the TiO_2 nanotubes and the polymer coated onto the walls of the TiO_2 nanotubes, forming polymer nanotubes after the solvent evaporated.

7.4 Conclusions

In conclusion, we have fabricated ordered TiO_2 nanotube arrays that are completely free of surface debris by 2 steps of anodization of titanium foil. P3HT polymer was infiltrated into the TiO_2 nanotube arrays by a dip-coating method at an elevated temperature of 65 ^oC. UV–Vis absorption spectrometer measurement of the P3HT/TiO_2 nanotube arrays showed that there was an absorption peak at 500 nm that is due to the embedded P3HT polymer within the nanotube arrays. TOF-SIMs depth profiling up to 500 nm showed that the P3HT polymer was infiltrated into the TiO_2 nanotube arrays. EDX measurement also detected the presence of sulfur and carbon elements within the P3HT/TiO_2 nanotube arrays. Polymer nanotubes can be observed with SEM after the TiO_2 nanotubes were etched away by dilute HF solution. Due to the large pore radius of the TiO_2 nanotube arrays (larger than the gyration radius of the polymer coil), an absence of surface debris and straight nanopores to the bottom of TiO_2 nanotube arrays, infiltration of P3HT polymer into the nanotubes have been achieved in this work.

7.5 References

[1] K. M. Coakley, B. S. Srinivasan, J. M. Ziebarth, C. Goh, Y. X. Liu, and M. D. McGehee, *Adv. Funct. Mater.* **15**, 1927 (2005).

[2] G. M. Wang, T. Hirasa, D. Moses, and A. J. Heeger, *Synth. Met.* **146**, 127 (2004).

[3] J. Park, S. Lee, and H. H. Lee, *Org. Electron.* **7**, 256 (2006).

[4] P. Schilinsky, C. Waldauf, and C. J. Brabec, *Adv. Funct. Mater.* **16**, 1669 (2006).

[5] H. Sirringhaus, T. Kawase, R. H. Friend, T. Shimoda, M. Inbasekaran, W. Wu, and E. P. Woo, *Science* **290**, 2123 (2000).

[6] S. E. Shaheen, R. Radspinner, N. Peyghambarian, and G. E. Jabbour, *Appl. Phys. Lett.* **79**, 2996 (2001).

[7] K. M. Coakley, Y. Liu, M. D. McGehee, K. L. Frindell, and G. D. Stucky, *Adv. Funct. Mater.* **13**, 301 (2003).

[8] G. P. Bartholomew and A. J. Heeger, *Adv. Funct. Mater.* **15**, 677 (2005).

[9] P. Atienzar, T. Ishwara, M. Horie, J. R. Durrant, and J. Nelson, *J. Mater. Chem.* **19**, 5377 (2009).

[10] S. Tepavcevic, S. B. Darling, N. M. Dimitrijevic, T. Rajh, and S. J. Sibener, *Small* **5**, 1776 (2009).

[11] G. W. Heffner and D. S. Pearson, *Macromolecules* **24**, 6295 (1991).

Chapter 8 Transparent titania nanotubes of micrometer length prepared by anodization of titanium thin film deposited on indium tin oxide

8.1 Introduction

Many groups have reported on the formation of TiO_2 nanotubes directly on the glass [1] and silicon substrates [2,3]. Transparent conductive oxide films coated on glass substrates like indium tin oxide (ITO) and fluorine-doped tin oxide (FTO) are important in the fabrication of electro-optical and chromic devices due to their conductivity and transparency. However, few research works have been carried out to investigate anodization of titanium on ITO/glass [4,5] even though there are many reports on anodization of titanium on FTO/glass [6-9].

In this work, transparent titania nanotubes of micrometer length were prepared via anodization of titanium thin films RF sputtered onto ITO/glass substrates. Using this technique, we are able to fabricate TiO_2 nanotube arrays with residue metal underneath the nanotubes completely eliminated. This transparent metal oxide electrode has important application for solar cell constructions.

It was shown that the nanotube formation was strongly affected by the concentration of NH_4F dissolved in a mixture of ethylene glycol and water which was used as an electrolyte in the anodization, the voltage applied and the thickness of the sputtered titanium film. Furthermore, we demonstrated that an upper nanoporous layer was formed on top of the ordered TiO_2 nanotube arrays. Lastly, annealed TiO_2 nanotube had lower transmittance than non-annealed TiO_2 nanotubes in the visible wavelength region.

8.2 Experiments

8.2.1 RF sputtering of Ti film on ITO/glass substrates

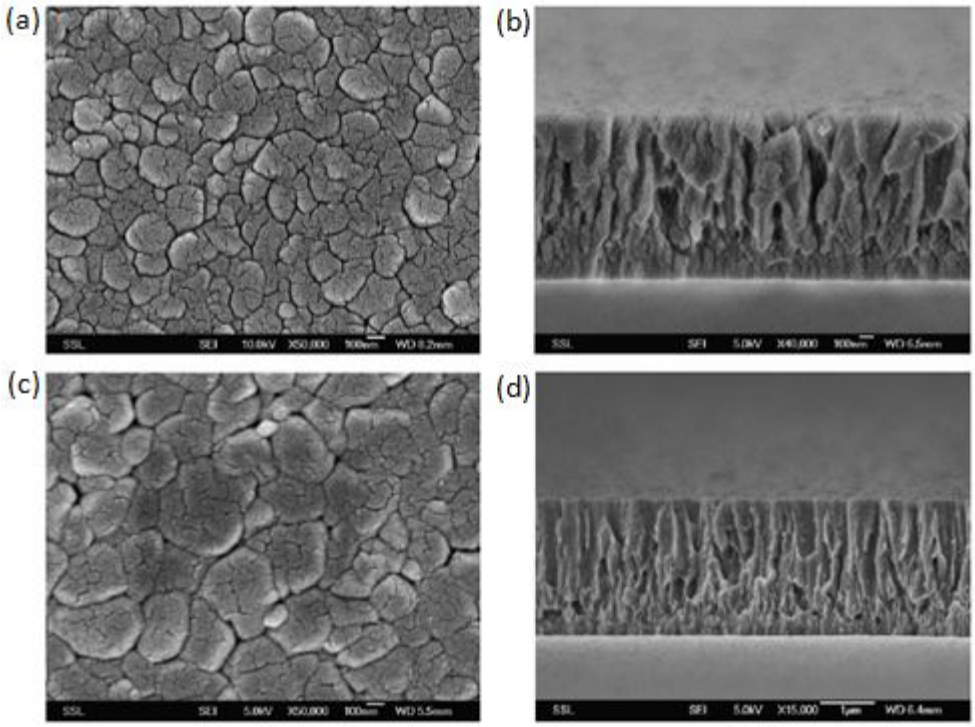

Fig. 8.1 SEM images of the RF sputtered titanium film on ITO/glass at 500 °C: (a) top view of the 3 h sputtered titanium film, (b) side view of the 3 h sputtered titanium film which is 1.2 μm thick. (c) Top view of the 6 h sputtered titanium film and (d) side view of the 6 h sputtered titanium film which is 2.4 μm thick.

Titanium films were first deposited onto ITO glass substrates by using RF sputtering technique with a 99.99% pure titanium target. The ITO glass substrates are bought from Sigma Aldrich. Before the deposition of titanium films, the ITO glass substrates were subjected to ultrasonic cleaning in acetone, isopropyl alcohol and ethanol for 30 min each sequentially. The sputtering chamber was pumped down to the pressure of 10^{-7} Torr before argon gas was introduced. During the deposition process, the argon gas pressure was 1.2×10^{-3} Torr. The total deposition times used were 3 h and 6 h. RF power of 180W was applied and substrate temperature was 500 °C. SEM images of the titanium films

sputtered onto the ITO glass substrate at 500 °C are given in Fig. 8.1. The titanium film formed round platelets when sputtered at elevated temperatures. It can be seen that the thickness of the film is proportional to the total deposition time. When the deposition time is 3 h, the total thickness of titanium film is 1.2 μm. When the deposition time is 6 h, the total thickness of titanium film is 2.4 μm. Furthermore, the size of platelet is observed to increase with deposition time.

8.2.2 Anodization of Ti film on ITO substrate

The first electrolyte used for anodization consisted of 0.25% (vol.) HF and acetic acid mixed with a volume ratio of 7:1. The second electrolyte used for anodization consisted of 0.25–1.00 % (wt.) NH_4F and 2% (vol.) H_2O dissolved in ethylene glycol solution. The anodization was performed at room temperature with graphite rod as cathode. The anodizing voltages were ranged from 20 V to 50 V. Prior to anodization, epoxy was used to cover the unanodized portion of the titanium film. The electrolyte was filled up to the portion of titanium covered by the epoxy so that bared titanium would be kept immersed in the electrolyte. The anodization was stopped when the current dropped to zero.

Table 8.1
Samples 1, 2 and 3 are anodized using electrolyte which consists of 0.75% (wt.) NH_4F and 2% (vol.) H_2O dissolved in ethylene glycol solution.

Sample	Thickness of sputtered Ti film (μm)	Anodization voltage (V)
Sample 1	2.4	40
Sample 2	1.2	40
Sample 3	2.4	20

Firstly, the effect of type and concentration of NH_4F presented in the electrolytes was investigated. In particular, 2.4 μm thick sputtered titanium film was anodized at 40 V

with electrolyte consisted of 0.25–1.00 % (wt.) NH_4F and 2% (vol.) H_2O dissolved in ethylene glycol solution. It is found that electrolyte consisting 0.75% (wt.) NH_4F and 2% (vol.) H_2O is optimal for the formation of TiO_2 nanotube arrays. Secondly, the effect of thickness of the sputtered film on the formation of nanotube was investigated by anodizing 1.2 μm thick of sputtered titanium film with the optimal electrolyte. Lastly, the voltage applied was varied from 20 V to 50 V during the anodization of 2.4 μm thick sputtered titanium film. Samples 1, 2 and 3 anodized using electrolyte which consists of 0.75% (wt.) NH_4F and 2% (vol.) H_2O in ethylene glycol are listed in Table 8.1.

8.2.3 Characterization

Surface morphology and crystalline phase of the TiO_2 nanotube arrays were studied by using field emission scanning electron microscopy (FESEM) and X-ray diffraction (XRD) spectroscopy, respectively. Transmittances of the TiO_2 nanotube arrays were measured by using a UV–visible spectrometer.

8.3 Results and discussion

8.3.1 Effect of type of electrolyte used on the 2.4μm thick sputtered titanium film

Type of electrolyte used for anodization can affect morphology of the TiO_2 nanotube array greatly. TiO_2 nanotube arrays were first formed by anodizing the 2.4 μm thick titanium film with an aqueous electrolyte that consisted of 0.25% (vol.) HF and acetic acid mixed with a volume ratio of 7:1 at 10V. Some areas of the ITO glass substrate are not covered by TiO_2 nanotube arrays. This could be due to the higher etching rate of TiO_2 nanotube arrays compared to the growth rate of TiO_2 nanotube arrays. Thus, electrolyte containing 0.25% (vol.) HF is not suitable for anodization of titanium.

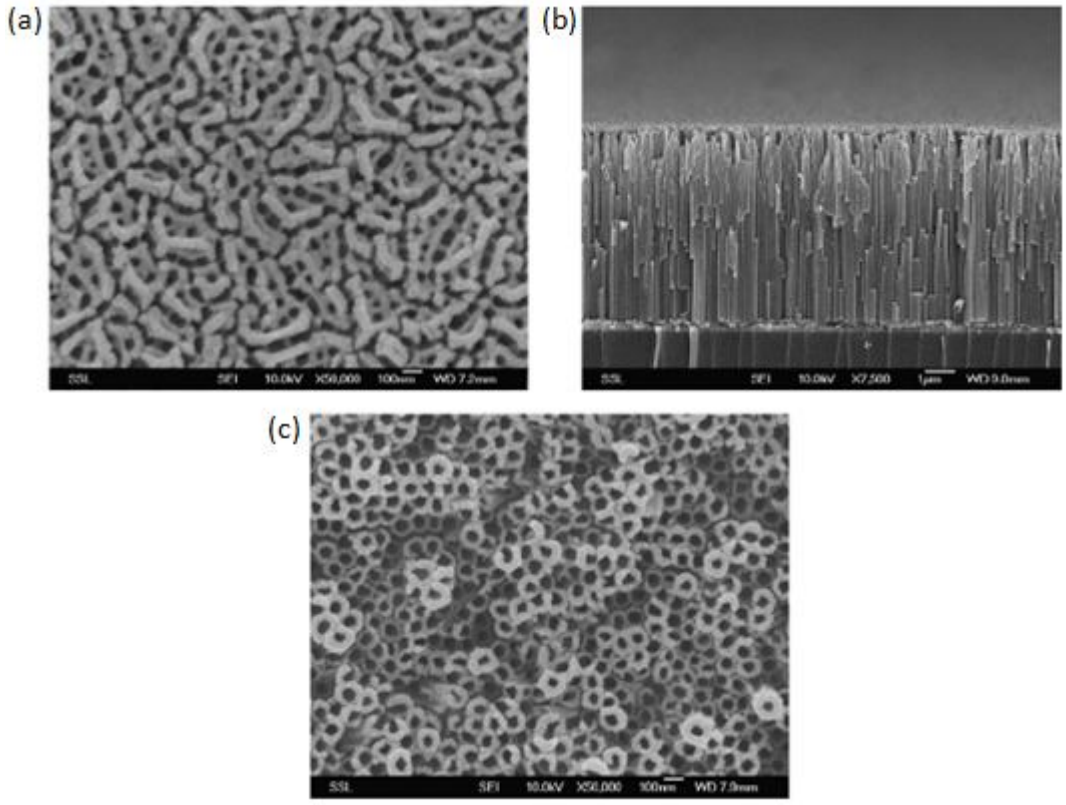

Fig. 8.2 SEM images of 2.4 μm thick titanium film anodized in an electrolyte consisting of 0.75% (wt.) NH_4F and 2% (vol.) H_2O dissolved in ethylene glycol at 40 V (sample 1). The duration of anodization is around 1h 20min: (a) top view of sample 1, (b) side view of sample 1 with thickness of 6.5 μm and (c) top view of sample 1after subjected to ultrasonic in a mixture of 50 nm Al_2O_3 powder dissolved in water for an hour.

The second electrolyte which contains 0.25–1.00 % (wt.) of NH_4F and 2% (vol.) H_20 in ethylene glycol was used for anodization of the 2.4 μm thick titanium film at 40 V. When 0.25% (wt.) NH_4F was used, tiny nanopores were developed along the boundary between grains of the sputtered titanium. Nanopores started to appear within the platelet when 0.50% (wt.) NH_4F was used. When 0.75% (wt.) NH_4F was used, pores with larger size were formed as shown in Fig. 8.2(a) which is the SEM top view of sample 1. Its corresponding side view is presented in Fig. 8.2(b), which shows that thickness of the TiO_2 nanotube is about 6.5 µm. The duration of the anodization is 1 h 20 min. When

sample 1 was subjected to ultrasonic in a mixture of 50 nm Al_2O_3 powder dispersed in distilled water, the Al_2O_3 nanoparticles in constant agitation bombard the upper TiO_2 nanoporous layer which are not mechanically strong to withstand the bombardment and as a consequence detached from the remaining TiO_2 nanotube array. More defined TiO_2 nanotube arrays with open and regular top morphology are revealed as observed in Fig. 8.2(c). Thus, we can conclude that ordered arrays of nanotubes were formed beneath this upper nanoporous layer and these nanopores lead to the openings of the nanotubes. It should be noted that some of the TiO_2 nanotube arrays formed are not robust enough to withstand the ultrasonic in the mixture of 50 nm Al_2O_3 powder and distilled water and thus detached completely from the ITO glass substrates. When 1.0% (wt.) NH_4F was used, TiO_2 nanotubes collapsed partially due to the higher etching rate caused by the higher concentration of F^- ions.

8.3.2 Effect of thickness of the sputtered titanium

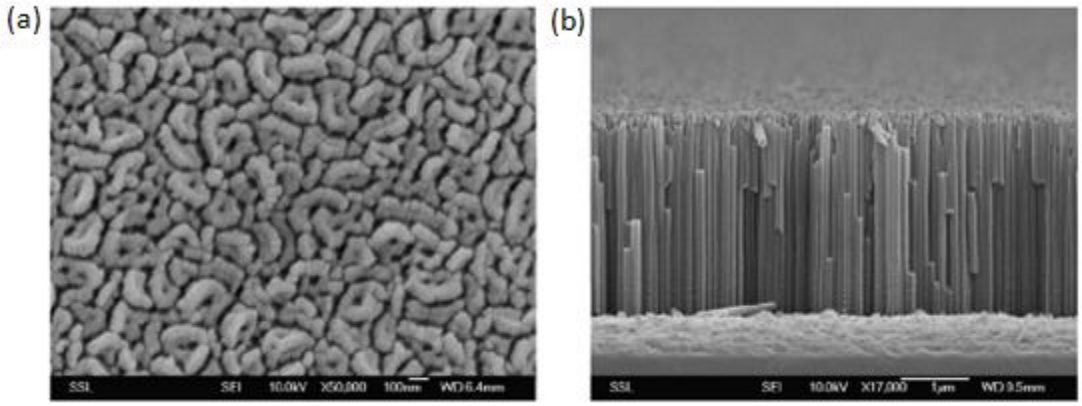

Fig. 8.3 SEM images of 1.2 μm thick titanium film anodized in an electrolyte consisting of 0.75% (wt.) NH_4F and 2% (vol.) H_2O dissolved in ethylene glycol at 40 V (sample 2). The duration of anodization is around 40 min: (a) top view of sample 2 and (b) side view of sample 2 with thickness of 3 μm.

The effect of thickness of the titanium on the formation of the TiO_2 nanotube array was investigated. The 1.2 μm thick sputtered titanium film was anodized at 40 V using an electrolyte consisting of 0.75% (wt.) NH_4F and 2% (vol.) H_20 in ethylene glycol (sample 2). The total time of anodization was 40 min. SEM top view and side views of sample 2 are presented in Fig. 8.3(a) and (b) respectively. From Fig. 8.3(a), we observe that smaller nanopores were formed in the upper layer. Fig. 8.3(b) shows that well ordered array of TiO_2 nanotubes with uniform size distribution was formed. Thickness of the film is about 3 μm. However, anodization of the 2.4 μm thick titanium film with the same condition led to the formation of larger nanopores in the upper layer (sample 1). This is because, with longer duration of anodization, more of the upper layer was etched away by F^- ions.

8.3.3 Effect of voltage on the 2.4 μm thick sputtered titanium film

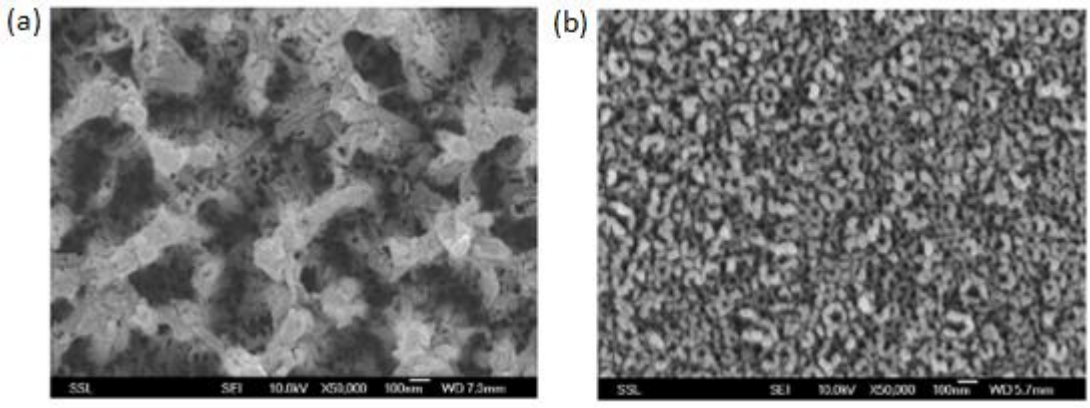

Fig. 8.4 SEM images of 2.4 μm thick titanium film anodized in an electrolyte consisting of 0.75% (wt.) NH_4F and 2% (vol.) H_2O dissolved in ethylene glycol at 20 V (sample 3). The duration of anodization is 6 h: (a) top view of sample 3 and (b) top view of sample 3 after subjected to ultrasonic in a mixture of 50 nm Al_2O_3 powder dissolved in the water for an hour.

The voltage applied during anodization was varied from 20 V to 50 V on the 2.4μm thick sputtered titanium film. The electrolyte used for anodization consisted of varying concentrations of NH_4F (according to the voltage applied) and 2% (vol.) H_2O in ethylene glycol. When the 2.4 μm titanium film was anodized at 20 V with an electrolyte consisting of 0.75% (wt.) NH_4F (sample 3), growth rate was extremely slow, thus requiring prolonged period of anodization. SEM top view of the titanium on ITO glass anodized at this condition for 6 h is shown in Fig. 8.4(a). It is found that the upper layer, which consisted of a compact layer at early stage of the anodization, was partially etched away at the end of the anodization. After the titanium oxide nanotube was subjected to the ultrasonication in the mixture of 50 nm Al_2O_3 powder and distilled water, more regular and ordered array of nanotubes underneath the partially etched upper layer are revealed, as shown in Fig. 8.4(b). Thus, 20 V is not suitable for anodization of the sputtered titanium film. When 50 V was applied during the anodization using 0.50–0.75% (wt.) NH_4F, the TiO_2 nanotubes were peeled off easily from the substrates since collapsed TiO_2 nanotubes which were formed at higher etching rate did not adhere to the substrates. On the other hand, using an applied voltage of 50 V but with reduced NH_4F concentration of 0.25% (wt.), the TiO_2 nanotubes adhered strongly to the substrate, but the nanotubes were covered by a layer with extremely small nanopores.

8.3.4 XRD and transmittance result

Typical XRD patterns of the sputtered titanium film, non-annealed and annealed sample 2 are presented in Fig. 8.5. Sadek et al. reported that the sputtered titanium film was actually TiO_2 due to the donation of oxygen from ITO to the sputtered titanium film during high temperature deposition process [4]. However, this is not observed in our

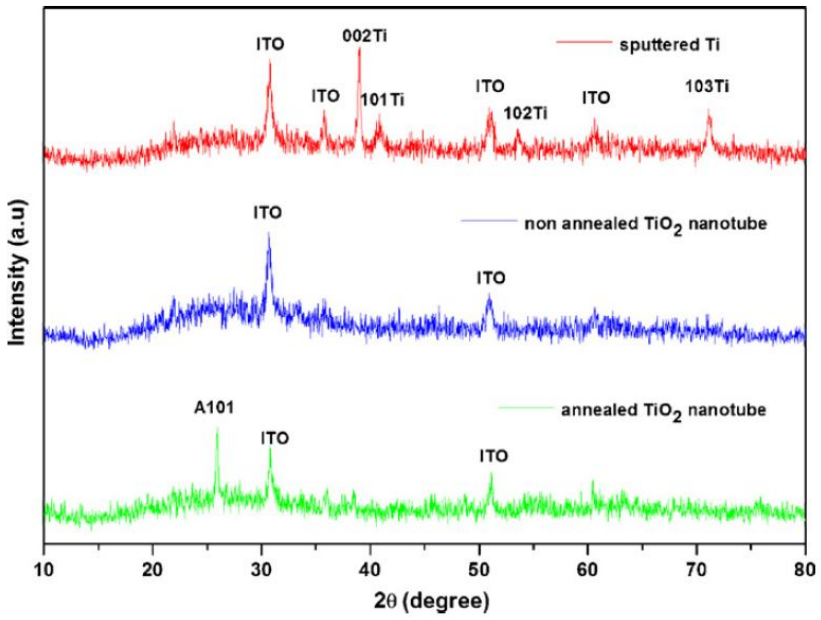

Fig. 8.5 XRD patterns of the 500 ˚C RF sputtered titanium film, annealed and non-annealed sample 2.

samples. We obtained pure titanium film on ITO glass with no oxidized forms of titanium in the 500 ˚C of RF sputtering process. This discrepancy is attributed to the lower back ground pressure of 10^{-7} torr used in this work as compared to background pressure of 10^{-5} torr used by Sadek et al. The decrease in the ITO conductivity and the formation of oxidized titanium reported by Sadek et al [4] is due to the presence of oxygen in the sputtering process.

The TiO_2 nanotube arrays are amorphous without annealing. When the TiO_2 nanotube arrays were annealed for 6 h at 450 ˚C (at heating and cooling rate of 1 ˚C /min), they crystallized to anatase phase. Digital images of Fig. 8.6 clearly show the change in the appearance of the titanium sputtered on ITO glass substrate before and after the thermal annealing. The as-anodized samples are fully transparent. Upon annealing, they become translucent. Transmittance spectra of samples 1 and 2 are shown in the Fig. 8.7. In the

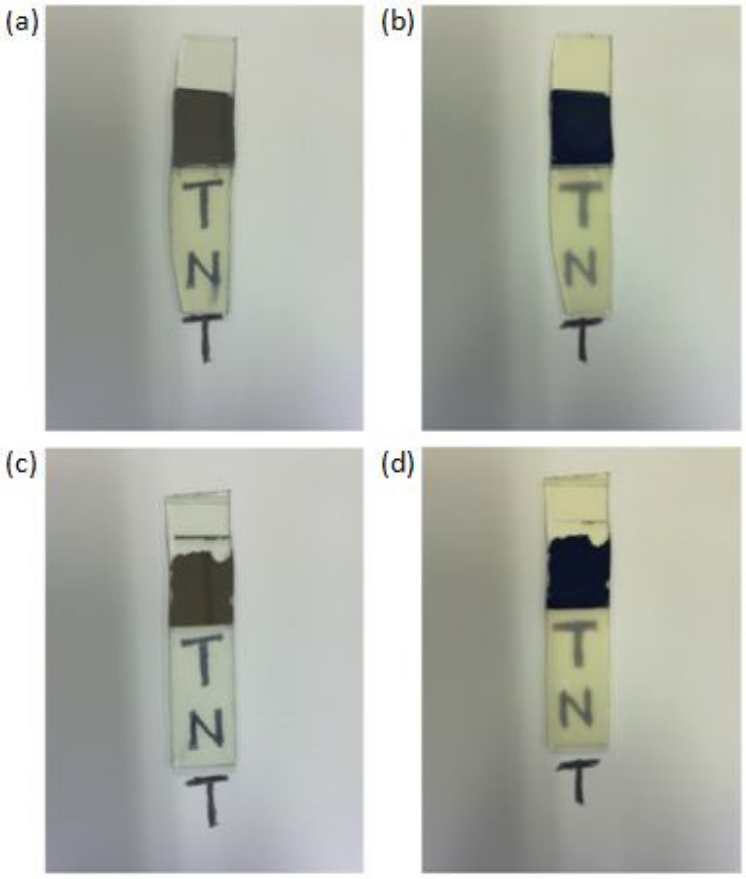

Fig. 8.6 Digital images of (a) non annealed sample 1, (b) annealed sample 1, (c) non annealed sample 2 and (d) annealed sample 2.

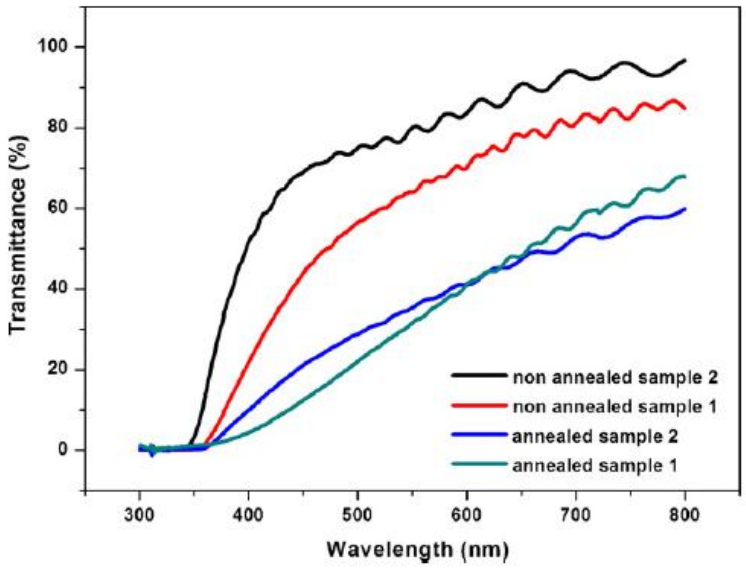

Fig. 8.7 Transmittance spectra of non-annealed and annealed samples 1 and 2.

UV region from 300 nm to 380 nm wavelength, the annealed and non-annealed nanotubes show exceedingly low transmission, which is due to mainly the semiconductor optical bandgap absorption of TiO_2. For the non-annealed TiO_2 nanotube arrays, the samples with longer TiO_2 nanotube have lower transmittance, because more scattering of the light occurs at theTiO_2/air interface within the taper-shaped TiO_2 nanotubes which have larger pore diameter at the top than at the bottom. In the visible region, the annealed samples demonstrate much lower transmittance than the non annealed samples. After the nanotubes were annealed at 450 $^{\circ}$C, oxygen vacancies were formed, which absorbed light [10]. Moreover, the TiO_2 nanotubes became more compact and denser and its reflective index became higher after annealing at 450 $^{\circ}$C [11].

8.4 Conclusions

Transparent TiO_2 nanotube arrays of micrometer length were prepared via anodization of titanium thin films RF sputtered on ITO/glass substrates. High etching rate led to the formation of damaged TiO_2 nanotube arrays and some of the nanotube arrays were completely detached from the substrate. TiO_2 nanotube arrays can be formed with non-aqueous electrolyte which consisted of NH_4F and water in ethylene glycol. It was found that the electrolyte consisting of 0.75% (wt.) NH_4F and 2% (vol.) H_2O and anodization voltage of 40 V were optimal for the formation of TiO_2 nanotube arrays. Annealed samples showed much lower transmittance in the visible region as compared to the non-annealed samples due to the larger light scattering and higher light absorption of oxygen vacancies introduced during the annealing.

8.5 References

[1] G. K. Mor, O. K. Varghese, M. Paulose and C. A. Grimes, *Adv. Funct. Mater.* **15**, 1291 (2005).

[2] J. M. Macak, H. Tsuchiya, S. Berger, S. Bauer, S. Fujimoto and P. Schmuki, *Chem. Phys. Lett.* **428**, 421 (2006).

[3] D. J. Yang, H. G. Kim, S. J. Cho and W. Y. Choi, *IEEE Trans. Nanotechnol.* **7**, 131 (2008).

[4] A. Z. Sadek, H. Zheng, K. Latham,W. Wlodarsk and K. K. Zadeh, *Langmuir* **25**, 509 (2009).

[5] J. Wang and Z. Lin, *J. Phys. Chem. C* **113**, 4026 (2009).

[6] P. Xiao, Y. H. Zhang, X. X. Zhang and G. Z. Cao, *J. Inorg. Mater.* **25**, 32 (2010).

[7] Y. X. Tang, J. Tao, Y. Y. Zhang, T. Wu, H. J. Tao and Z. G. Bao, *Acta Phys.-Chim. Sinica* **24**, 2191 (2008).

[8] Y. X. Tang, J. Tao, H. J. Tao, T. Wu, L. Wang, Y. Y. Zhang, Z. L. Li and X. L. Tian, *Acta Phys.-Chim. Sinica* **24**, 1120 (2008).

[9] H. D. Zheng, A. Z. Sadek, M. Breedon, D. Yao, K. Latham, J. du, K. Plessis and Kalantar- Zadeh, *Electrochem. Commun.* **11**, 1308 (2009).

[10] G. Tian, L. Dong, C. Wei, J. Huang, H. He and J. Shao, *Opt. Mater.* **28**, 1058 (2006).

[11] X. D. Xiao, G. P. Dong, H. J. Qi, Z. X. Fan, H. B. He and J. D. Shao, *Chin. Phys. Lett.* **25**, 2181 (2008).

Chapter 9 Conclusions

9.1 Conclusions

With the aid of aluminum oxide template, three magnetic nanostructures have been fabricated: (1) ferromagnetic $CoFe_2$ nanowires (2) ferromagnetic CoAlO antidot arrays and (3) multilayered ferromagnetic (FM) FeNi and antiferromagnetic (AFM) FeMn antidot arrays. Geometrical effects of the aluminum oxide templates on magnetic properties of these magnetic nanostructures have been investigated.

Coercivity and remanence of the $CoFe_2$ nanowires increased with the length of the nanowires, which can be explained by taking into account the effect of magnetostatic interaction between the nanowires due to the coupling of stray field with the magnetization of nanowires. The magnetostatic interaction favors an anti-parallel distribution of magnetization in neighboring nanowires, which reduced the coercivity and remanence of nanowire arrays.

Both pore size and thickness have strong influences on magnetic properties and magnetotransport properties of the CoAlO antidot arrays. As the pore diameter was increased, magnetic hysteresis loop of the 40 nm thick CoAlO antidot arrays changed from anisotropy to isotropic and the coercivity increased. This observation can be explained by the topology-induced shape anisotropy. It was also found that the CoAlO antidot arrays with pore diameter of 80 nm showed a quick reduction in coercivity as the thickness was increased, which can be attributed to the change in domain reversal process from domain rotation in thin antidot to wall motion in the samples with higher structural continuity. Furthermore, thicker sample showed negligible magentoresistive loops which could be due to the spin-independent electron scattering.

The exchange bias field (H_E) of the FeNi/FeMn antidot arrays with thinner FM layers was enhanced significantly as the pore diameter was increased, but it did not change much in the samples with thicker FM layers. This behaviour can be qualitatively explained by employing the random field model. According to this model, FM domain size is determined by the competition between FM-FM interaction and random field due to the interfacial FM-AFM interaction. When the pore size was increased in thin FM layer antidot array, the FM-FM interaction was weakened, resulting in smaller FM domain and larger net random fields and exchange bias field. In a thicker FM layer antidot array, the FM-FM interaction remained strong and the FM domains did not decrease drastically as in the thin FM layer when the pore diameter was increased. Consequently, the exchange bias field did not change much. Microwave resonance frequency would be significantly enhanced which has been confirmed experimentally.

P3HT/TiO_2 nanotube arrays were fabricated by infiltration of P3HT into the TiO_2 nanotubes in Ti foil via anodization. Due to the large pore radius of the TiO_2 nanotube arrays (larger than the gyration radius of the polymer coil), absence of surface debris and straight nanopores to the bottom of TiO_2 nanotube arrays, infiltration of P3HT polymer into the nanotubes could be achieved.

TiO_2 nanotubes were also fabricated directly on ITO/glass via anodization of sputtered titanium films on ITO/glass. TiO_2 nanotube arrays can be formed with non-aqueous electrolyte which consisted of NH_4F and water in ethylene glycol. It was found that electrolyte consisting of 0.75% (wt) NH_4F and 2% (vol) H_2O and anodization voltage of 40 V were optimal for the formation of the TiO_2 nanotube arrays. It was also demonstrated that a nanoporous layer was formed on top of the ordered TiO_2 nanotube

arrays. Annealed samples showed much lower transmittance in the visible region due to the larger light scattering and higher light absorption of the oxygen vacancies introduced during the annealing.

9.2 Future Work

The dipolar interaction between the $CoFe_2$ nanowires of varying length can be also be investigated using high frequency ferromagnetic resonance (FMR) techniques. This can be done so by using a microstrip transmission line to excite uniform mode of resonance in the array of $CoFe_2$ nanowires at microwave frequency. In this experimental setup, the microwave signal propagation along the microstip transmission line produces a RF field which is perpendicular to the nanowires and induces a precession of the magnetization around the static equilibrium position which is parallel to the nanowire. At ferromagnetic resonance power is absorbed from the incident microwave signal and the corresponding minimum in the transmitted power is recorded by a network analyzer.

FMR technique can also be used to characterize the dynamic properties of CoAlO antidot array with different pore diameter. Microstrip transmission line can be used to excite uniform mode of resonance in the array of CoAlO antidot array at microwave frequency. In this experimental setup, the static field is applied along the direction of the easy axis of induced magnetic anisotropy while the RF field is applied perpendicular to the static applied field along the plane of the film. At ferromagnetic resonance power is absorbed from the incident microwave signal and the corresponding minimum in the transmitted power is recorded by a network analyzer.

We can also investigate the exchange field in the FeNi/FeMn antidot array as a function of temperature. AFM layers in antidot array are more susceptible to thermal

activation effects as compared to a continuous film. This will result in the depinning of a large proportion of the AFM spin lattice and affect the magnitude of the exchange field.

Chapter 7 shows that infiltration of P3HT polymer into the TiO_2 nanotube can be achieved by dip coating method. Chapter 8 shows the successful fabrication of TiO_2 nanotubes on ITO substrate via anodization of Ti thin film sputtered on ITO. These two chapters indicate the possibility of constructing a hybrid TiO_2 nanotube/P3HT polymer photovoltaic. This photovoltaic can be fabricated by using dip coating method to introduce the P3HT polymer into the TiO_2 nanotube fabricated on ITO substrate. Finally gold electrode can be sputtered on top of P3HT layer atop TiO_2 nanotube. ITO allows the light to be illuminated onto P3HT polymer which will be able to absorb photon to create exciton. These exciton will dissociate into freed hole and electron at the interface of TiO_2/P3HT polymer and hence photocurrent is generated.

Bibliography

1. Y. G. Ma, S. L. Lim and C. K. Ong, Evolution of magnetic and transport properties in pore-modified CoAlO antidot arrays, *Journal of Physics D: Applied Physics* **40**, 935 (2007)
2. N. N. Phuoc, S. L. Lim, F. Xu, Y. G. Ma and C. K. Ong, Enhancement of exchange bias and ferromagnetic resonance frequency by using multilayer antidot arrays, *Journal of Applied Physics* **104**, 093708 (2008)
3. S. L. Lim, F. Xu, N. N. Phuoc and C. K. Ong, Length dependence of coercivity in $CoFe_2$ nanowire arrays with high aspect ratios, *Journal of Alloys and Compounds* **505**, 609 (2010)
4. S. L. Lim, Y. L. Liu, G. Liu, S. Y. Xu, H. Y. Pan, E. T. Kang and C. K. Ong, Infiltrating P3HT polymer into ordered TiO_2 nanotube arrays, *Physica Status Solidi A* **208**, 658 (2011)
5. S. L. Lim, Y. L. Liu, J. Li, E. T. Kang and C. K. Ong, Transparent titania nanotubes of micrometer length prepared by anodization of titanium thin film deposited on ITO, *Applied Surface Science* **257**, 6612 (2011)